Jinkeun Kim
Zhe Chen   *Editors*

Trends in Environmental Sustainability and Green Energy

Proceedings of 2022 5th International Conference on Green Energy and Environment Engineering

Springer

Springer Proceedings in Earth and Environmental Sciences

The series Springer Proceedings in Earth and Environmental Sciences publishes proceedings from scholarly meetings and workshops on all topics related to Environmental and Earth Sciences and related sciences. This series constitutes a comprehensive up-to-date source of reference on a field or subfield of relevance in Earth and Environmental Sciences. In addition to an overall evaluation of the interest, scientific quality, and timeliness of each proposal at the hands of the publisher, individual contributions are all refereed to the high quality standards of leading journals in the field. Thus, this series provides the research community with well-edited, authoritative reports on developments in the most exciting areas of environmental sciences, earth sciences and related fields.

Jinkeun Kim · Zhe Chen
Editors

Trends in Environmental Sustainability and Green Energy

Proceedings of 2022 5th International Conference on Green Energy and Environment Engineering

 Springer

Editors
Jinkeun Kim 🆔
Jeju National University
Jeju, Korea (Republic of)

Zhe Chen 🆔
Aalborg University
Aalborg, Denmark

Preface

2022 5th International Conference on Green Energy and Environment Engineering (CGEEE 2022) was successfully held as virtual conference during July 28–30, 2022. The conference is an annual event which has been conducted since 2018. CGEEE 2022 was held for three days. Three keynote speakers are invited this year, including Prof. Jae K. Park form the University of Wisconsin-Madison, USA; Prof. Marco Casini from Sapienza University of Rome, Rome, Italy; and Prof. Zhe Chen from Aalborg University, Denmark, as well as one invited speaker Prof. Sweety Vermas from Inje University, South Korea. Additionally, five technical sessions are arranged in the conference, including environmental biology and ecological protection; sewage treatment and marine pollution assessment; environmental management, environmental chemical engineering and sustainable development; green energy technology, thermal engineering and energy management; and clean energy technology, energy management and pollution control. Many researchers, engineers, academicians as well as industrial professionals from all over the world have presented their research results and development activities.

This volume of proceedings includes papers which were presented at CGEEE 2022. All of the papers were subjected to peer review by conference committee members and international reviewers. The final papers selected depended on their quality and relevancy to the conference. Topics covered by these papers include environmental pollution analysis, green energy and environment engineering pollution treatment, ecological environment protection and sustainable development, renewable energy and clean energy technology. The proceedings can serve as a reference and hopefully inspire new ideas for scientists, engineers, graduate students, equipment manufactures and operators, as well as technical managers who are working in the related fields.

We will continue to organize this conference in the future to provide a much effective platform for further exchange of new knowledge and perhaps potential collaboration in all aspects.

The organizer would like to thank all the conference participants for their support to CGEEE 2022. Especially, we would like to thank all the members of organizing committee, invited speakers, chairpersons and sponsors for their valuable suggestions in the organization and all the reviewers for their professional peer review of the submitted papers.

Jinkeun Kim
CGEEE 2022 Conference Chair

Conference Committees

Conference Advisory Chair

Jae K. Park   University of Wisconsin-Madison, USA

Conference Co-chairs

Jinkeun Kim   Jeju National University, Jeju, Korea
Zhe Chen (FIET, FIEEE)   Aalborg Universitet, Denmark

Conference Program Chairs

Suyin Gan   University of Nottingham Malaysia, Malaysia
Keh-Chin Chang   National Cheng Kung University, Taiwan
Yu Liu   Northwestern Polytechnical University, Shaanxi, China

International Steering Committee

Kristopher Ray S. Pamintuan   Mapua University, Philippine

Technical Committee Members

Karamanis Dimitrios   University of Patras, Greece
Yarusova Sofia Borisovna   Far-Eastern Branch of Russian Academy of Sciences, Russian
Engr. Kristopher Ray S. Pamintuan   Mapua University, Philippine
Saad A. EL-Sayed   Zagazig University- Al-Sharkia, Egypt
Svetla Draganova Tzvetkova   University of National and World Economy, Bulgaria
Zeeshan Haider Jaffari   Chaoyang University of Technology, Taiwan
Yu Liu   Northwestern Polytechnical University, Shaanxi, China

Suyin Gan	The University of Nottingham Malaysia, Malaysia
Keh-Chin Chang	National Cheng Kung University, Taiwan
Svenja Hanson	University of Nottingham, Ningbo, China
Supachok Tanpichai	King Mongkut's University of Technology, Thailand
Cheng Siong Chin	Newcastle University, Singapore
Radu Godina	Universidade Nove de Lisboa, Caparica, Portugal
Lorant Andras Szolga	Technical University of Cluj-Napoca, Romania
Elanur Adar	Artvin Coruh University, Turkey
Yanqiang Di	China Academy of Building Research & China Building Technique Group Co., Ltd.
Ahmad Zamani Ab Halim	Universiti Malaysia Pahang, Malaysia
Hala Idrassen	Cadi Ayyad University, Maroc
Sweety Vermas	Inje University, South Korea
Sunq Won Kim	Korea National University of Transportation, Korea
Michel De Paepe	Ghent University, Belgium

Contents

Renewable Energy and Clean Energy Technology

Environmental Pollution Analysis and Pollution Treatment

A Study of Arsenic Extraction Efficiency from Heavy Metal Contaminated Soils

H. Jeon and S. Park[(✉)]

Korea University of Technology and Education, Cheonan 31253, South Korea
spark@koreatech.ac.kr

Abstract. Timely on-site detection of heavy metal contaminations in soil and ground water is crucial for environmental monitoring and minimizing the risk to human health. In this study, a single extractant based method for the extraction of arsenic ions from soils has been developed and evaluated. The designed protocol has been modified by adjusting the acid mixing volume and digestion time, and the efficiency has been evaluated with three different types of soils (standard, spiked, and field soils). Comparisons have been made between the proposed method and the standard laboratory based protocol using aqua regia extraction. The proposed method has shown reduced processing steps and time, allowing a simple and rapid on-site sample pre-processing for soil monitoring.

Keywords: Soil analysis · Heavy metals · Arsenic · Extraction

1 Introduction

Arsenic contamination poses a great threat to the living organisms even in small traces [1–6]. Especially, arsenic contamination in soil affects the wide variety of living organisms, and is recognized that carcinogenesis can possibly be caused to humans even in trace amount. While several protocols are available, conventional methods for analyzing heavy metal contamination in soil and water generally require laboratory equipped instruments and complex procedures, and thus have limited applicability for onsite sensing and monitoring of contaminated area [7–12]. The heavy metals in the soil environment exist in diverse ways, such as adsorbed or precipitated on the surface of minerals, co-precipitated with carbonate or oxide minerals, combined with organic compounds, or involved between silicate mineral lattices. However, the differentiation of these diverse forms of bound heavy metals is challenging or often impossible. The analytical process generally requires a sample preprocessing steps such as extraction of target metal ions from the soil and subsequent quantification of analytes. The sample pre-processing step has dominant importance for maximizing the analytical accuracy, however, labor-intensive and tedious process with strong acids hinders the on-site operation, which has been the actual bottle neck of developing an automated soil monitoring system [13, 14].

Due to the simplicity of the operation, a single extractant based extraction procedure is generally preferred and widely used. However, it is difficult to apply a single method universally and each method requires the optimization step because the forms of heavy

metals in soils are influenced by soil properties and various environmental factors. In this study, simplified protocols for arsenic extraction from contaminated soils with a single extractant are presented. Acid based extraction (1M HCl) has been designed and tested with spiked as well as field samples collected from arsenic contaminated sites in South Korea, and the extraction efficiencies have been measured. In order to assess the performance of the proposed protocol, the extraction efficiencies are compared with the standard laboratory protocol.

2   Materials and Methods

2.1   Soil Samples

3 types of samples, standard, spiked, and field samples, were prepared for the evaluation of the extraction efficiencies. The standard soil, BAM-U112a, was purchased from Odlab, South Korea. Two spiked samples were prepared in laboratory. Soils were first collected from the uncontaminated sites and filtered with 150 m mesh, then dried outside. All collected soils were kept in dried and dark container for the future laboratory use. To spike arsenic, NaAsO2 (Sigma-Aldrich, USA) was diluted with DI water and mixed with the soils. Then the spiked soils were dried in 100 °C oven for 2 h. Similarly, three field samples were collected from the arsenic contaminated sites in South Korea. Figure 1 shows different types of soil samples in this study. The composition of heavy metal ions in all test samples were analyzed by the standard laboratory method with inductively coupled plasma optical emission spectrometry (ICP-OES). Table 1 summarizes the concentration of heavy metal ions in each test sample.
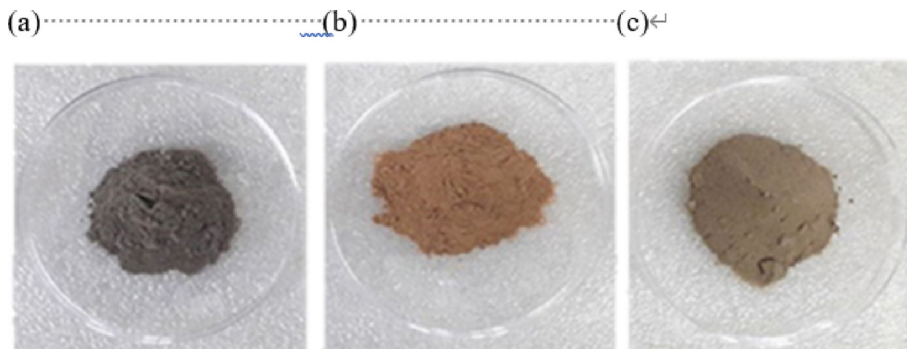
Fig. 1.   Test samples (a) Standard soils (b) As spiked soils (c) As contaminated field soils.

Table 1. I: Heavy metal ion concentration (ppm) in test soils

Soils	As	Cd	Cu	Ni	Pb	Zn	Hg	Fe
Standard (BAM)	10.3	4.12	75.5	10.1	198	198	16.3	1
Spiked sample 1	378.5	NA	NA	NA	NA	NA	NA	NA
Spiked sample 2	211.3	NA	NA	NA	NA	NA	NA	NA
Field sample A	2	0	2.02	0	1.5	3.66	-	191.3
Field sample B	214.8	NA	NA	NA	NA	NA	NA	NA
Field sample C	260.7	NA	NA	NA	NA	NA	NA	NA
Field sample D	280	NA	NA	NA	NA	NA	NA	NA
Field sample E	500	NA	NA	NA	NA	NA	NA	NA
Field sample F	595	NA	NA	NA	NA	NA	NA	NA
Field sample G	719.1	1	15.6	14.2	143.6	177.1	4.61	NA
Field sample H	1028	1.38	13.6	8.7	246	250	4.01	NA
Field sample I	2052	NA	NA	NA	NA	NA	NA	NA

2.2 Extraction

Arsenic extraction from the soil samples was tested using hydrochloric acid, HCl (Samchun chemicals, South Korea) and sodium hydroxide, NaOH (Merck, Germany). Extraction of arsenic ions was performed by mixing 200 mg of soil samples with 1–40 ml of 1M HCl in a centrifuge tube and homogenizing with the tube shaker for 30–60 min at 60 rpm. If needed, sonication was applied at 60 °C for 0.5–2 h. Samples were then diluted with DI water and filtered through the 12 m filter paper (Chmlab, Spain) and collected in a tube. For the comparison of the extraction efficiency, the standard extraction protocol, ES07000 from Korea Ministry of Environment, was selected and applied, which is based on aqua regia digestion.

2.3 Statistical Analysis

The difference in the extraction parameters was analysed by one-way ANOVA (SPSS 16.0 software; Macrovision Corporation Santa Carlo, California, USA) followed by

turkey's post-hoc test to compare the differences between the time points. P < 0.05 was considered as statistically significant.

3   Results

Many types of acidic or basic solutions have been applied for the extraction of arsenic from soils in the literature, and strong acids such hydrofluoric acid (HF), phosphoric acid (H_3PO_4), and sulfuric acid (H_2SO_4) are generally known as highly efficient extractants (Alam and Tokunaga, 2006). However, these strong acids may cause environmental and handling hazards for on-site operations. In this study, we have selected relatively mild extractants, 1M HCl and 2M NaOH. The binding between soils and heavy metal ions is affected by various physical, chemical and biochemical factors, and a parametric study is generally required for extracting target ions. Figure 2 shows the comparison of the efficiencies of the arsenic extraction from standard soils. 200 mg of soil is extracted with 40 ml of each extractant. HCl has shown relatively higher efficiency of 73.8% compared to the case of NaOH, having 38.4%. Including standard soils, HCl has shown higher efficiencies for most of test samples, and thus further parametric studies have been performed by using HCl as an extractant.
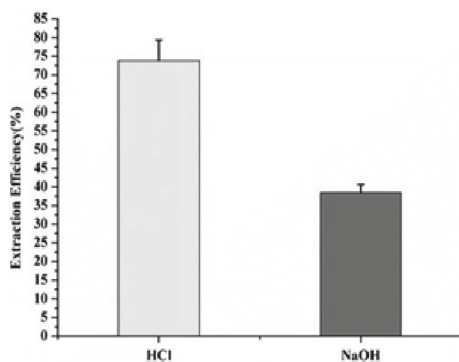
Fig. 2. Arsenic extraction efficiencies from standard soils using HCl and NaOH

Elution of heavy metals bound in soils can generally be increased with the digestion time, but the rapid operation requires the minimized processing time. In order to observe the effect of digestion time, we have tested the extraction from spiked soils. Soils with concentrations of 211.3 and 378.5 ppm were prepared by spiking sodium nitrite aqueous solution (NaAsO2) into the field collected soils. As shown in Fig. 3, the extraction efficiencies for two different spiked samples at different arsenic concentration were increased with the digestion time. The recovery rate of the target ion was higher than 90% when the digestion time of 60 min were applied, which can then be selected as the reduced processing time.

The elution of metal ions requires the time for chemical diffusion as well as extractant volume [15]. The tests were conducted in two ratios, 1:5 and 1:200. As shown in Fig. 4,
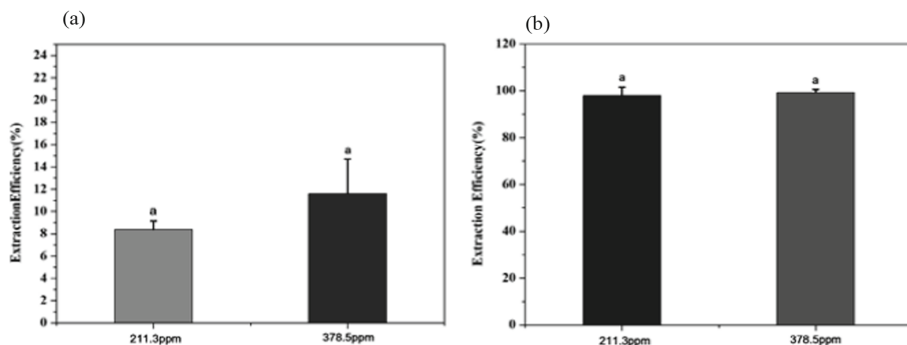
Fig. 3. Arsenic extraction efficiencies from two different spiked soils with the digestion time of (a) 30 min (b) 60 min. Soil-to-acid ratio was 1:200.

higher soil-to-acid ratio has shown better extraction efficiency in case of the spiked soil samples. The low soil-to-acid ratio, 1:5, showed low efficiencies of 7% and 12% at 211.3 ppm and 378.5 ppm soils, respectively, whereas the 1:200 ratio showed high efficiencies of 97% and 99%.
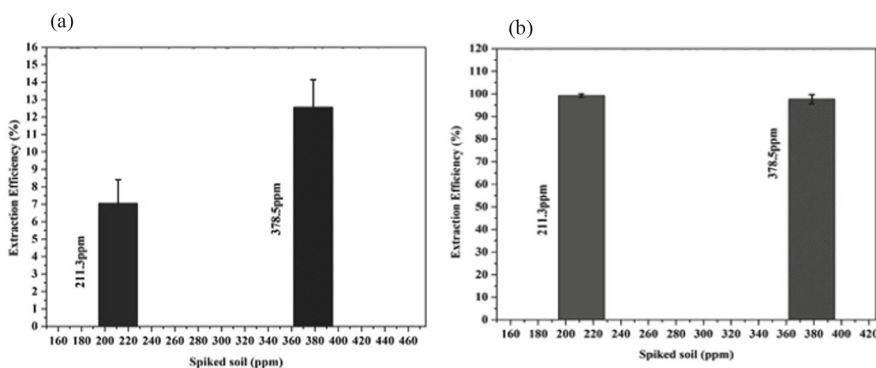
Fig. 4. Arsenic extraction efficiencies from two different spiked soils with the soil-to-acid ratio of (a) 1:5 (b) 1:200. Digestion time was 60 min.

However, the effect of extractant volume was statistically insignificant ($p \leq 0.05$) in the case of field soil samples as shown in Fig. 5. Four different field soils at the arsenic concentration of 42.5, 62.4, 218.8, and 280.0 ppm have been tested and the average extraction efficiency were found to be 36.9% and 38.4% for 1:5 and 1:200 soil-to-acid ratio, respectively. In the literature, it is reported that more stable ion binding can be formed in field soils due to aging, which can reduce the effect of the extractant volume [16–18]. Because the high soil-to-acid ratio provides less dilution factor for maximizing the analytical accuracy and the handling in small volume is also favorable for on-site operations, 1:5 soil-to-acid ratio was selected in the finalized protocol for the field soil extraction.
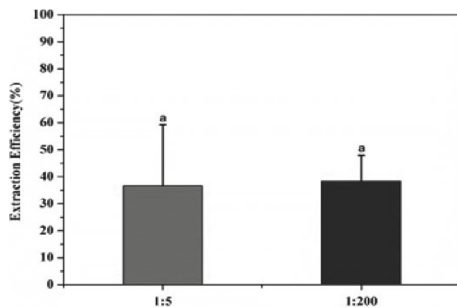
Fig. 5. Averaged arsenic extraction efficiencies from 4 field soil samples with the soil-to-acid ratio of 1:5 and 1:200. Digestion time was 60 min.

The spiked and standard soils also have been tested for the finalized protocol to check the variability of the extractions. As shown in Fig. 6, the averaged extraction efficiency for the spiked and standard samples were observed to be 94.5% and 51.8%, respectively. Weak binding feature of arsenic ions in spiked samples caused relatively high recovery rate compared to the standard samples. However, the comparative efficiency with the aqua regia based standard method is high enough to be applied in the subsequent analytical processes.
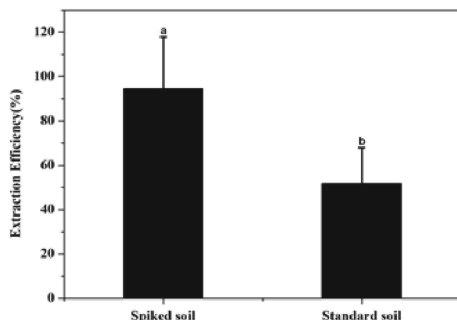
Fig. 6. Arsenic extraction efficiencies from standard soils with the soil-to-acid ratio of 1:5. Digestion time was 60 min.

In order to examine the efficacy of the developed protocol, 9 different field samples with various arsenic concentration, ranging from 2 to 2052 ppm, have been tested for the extraction efficiency. All soil samples were filtered with a sieve after collection, and digested with 1M HCl for 60 min at 1:5 soil-to-acid ratio. After the digestion, the residue was filtered through a 12 m filter paper, and the filtrate is transferred to a 50 mL centrifuge tube for analysis. Figure 7 shows the results of extraction efficiencies. Depending on the soil composition, extraction efficiencies ranging from 11.5% to 66.7% have been achieved. It should be noted that field soils with low arsenic concentration show lower extraction efficiencies. Leaching may be accelerated at higher concentration

due to the chemical nature, however, heavy metal binding features are still dependent on the chemical, physical, and biological profile of soils [19, 20].
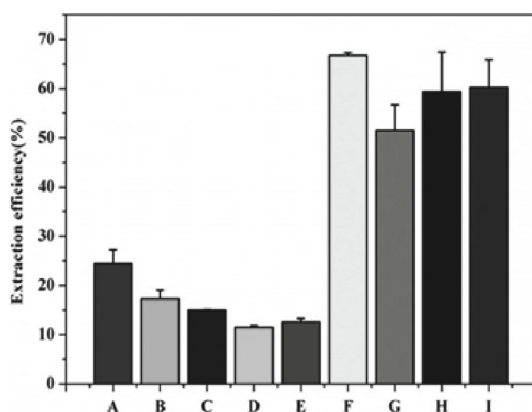
Fig. 7. Arsenic extraction efficiencies from field soil samples with the soil-to-acid ratio of 1:5 and digestion time of 60 min.

4 Conclusions

In this study, we have presented a single acid based extraction method for arsenic extraction from contaminated soils. With the utilization of a relatively mild acid, 1M HCl, high recovery rate of over 70% has been validated for laboratory samples of standard and spiked soils. The performance of the method has been confirmed with the field sample collected from various contaminated sites, and the extraction efficiencies ranging from 11 to 66% have been demonstrated. With the simplified processing step, the presented protocols eliminate the complexity of the standard method and enable streamlined analytical sample preparation. Future study includes the implementation of the developed protocol with a portable analytical system and the validation of its effectiveness.

References

1. Jayasumana, C., et al.: Phosphate fertilizer is a main source of arsenic in areas affected with chronic kidney disease of unknown etiology in Sri Lanka. Springerplus **4**(1), 1–8 (2015). https://doi.org/10.1186/s40064-015-0868-z

2. Smith, S.: A critical review of the bioavailability and impacts of heavy metals in municipal solid waste composts compared to sewage sludge. Environ. Int. **35**(1), 142–156 (2009)
3. Nriagu, J.: A global assessment of natural sources of atmospheric trace metals. Nature **338**, 47–49 (1989)
4. Mandal, B., Suzuki, K.: Arsenic round the world: a review. Talanta **58**(1), 201–235 (2002)
5. Molin, M., Ulven, S.M., Meltzer, H.M., Alexander, J.: Arsenic in the human food chain, biotransformation and toxicology–review focusing on seafood arsenic. J. Trace Elem. Med. Biol. **31**, 249–259 (2015)
6. Podol'skaya, V.I., Gruzina, T.G., Ul'berg, Z.R., Sokolovskaya, A.S., Grishchenko, N.I.: Effect of arsenic on bacterial growth and plasma membrane ATPase activity. Appl. Biochem. Microbiol. **38**, 48–52 (2002)
7. Jung, M.C.: Heavy metal concentrations in soils and factors affecting metal uptake by plants in the vicinity of a Korean Cu-W mine. Sensors **8**, 2413–2423 (2008)
8. Wang, C., Li, W., Guo, M., Ji, J.: Ecological risk assessment on heavy metals in soils: use of soil diffuse reflectance mid-infrared Fourier-transform spectroscopy. Sci. Rep. **7**, 40709 (2017)
9. Gleyzes, C., Tellier, S., Astruc, M.: Fractionation studies of trace elements in contaminated soils and sediments: a review of sequential extraction procedures. Trends Anal. Chem. **21**(6), 451–467 (2002)
10. Tessier, A., Campbell, P.G.C., Bisson, M.: Sequential extraction procedure for the speciation of particulate trace metals. Anal. Chem. **51**(7), 844–851 (1979)
11. Quevauviller, P.: Operationally defined extraction procedures for soil and sediment analysis I Standardization. Trends Anal. Chem. **17**(5), 289–298 (1998)
12. Sahuquillo, A., Rigol, A., Rauret, G.: Overview of the use of leaching/extraction tests for risk assessment of trace metals in contaminated soils and sediments. Trends Anal. Chem. **22**(3), 152–159 (2003)
13. Park, J.H., Lamb, D., Paneerselvam, P., Choppala, G., Bolan, N., Chung, J.W.: Role of organic amendments on enhanced bioremediation of heavy metal (loid) contaminated soils. J. Hazard. Mater. **185**(2), 549–574 (2011)
14. Pueyo, M., Rauret, G., Bacon, J.R., Gomez, A.: A new organic-rich soil reference material certified for its EDTA-and acetic acid-extractable contents of Cd, Cr, Cu, Ni, Pb and Zn, following collaboratively tested and harmonised procedures. J. Environ. Monitor. **3**(2), 238–242 (2001)
15. Tandy, S., et al.: Extraction of heavy metals from soils using biodegradable chelating agents. Environ. Sci. Technol. **38**(3), 937–944 (2004)
16. Hamels, F., Maleve, J., Sonnet, P., Kleja, D.B., Smolders, E.: Phytotoxity of trace metals in spiked and field-contaminated soils: linking soil-extractable metals with toxicity. Environ. Toxicol. Chem. **33**(11), 2479–2487 (2014)
17. Lesniewska, B., Gontarska, M., Godlewska, B.: Selective separation of chromium species from soils by single step extraction methods: a critical appraisal. Water Air Soil Pollut. **228**, 274 (2017)
18. Smit, C.E., Van Gestel, C.A.M.: Effects of soil type, prepercolation, and ageing on bioaccumulation and toxicity of zinc for the springtail Folsomia candida. Environ. Toxicol. Chem. **17**(6), 1132–1141 (1998)
19. Rieuwerts, J.S., Thornton, I., Fargo, M.E., Ashmore, M.R.: Factors influencing metal bioavailability in soils: preliminary investigations for the development of a critical loads approach for metals. Chem. Speciation Bioavailability **10**(2), 61–75 (1998)
20. Tariq, S.R., Shafiq, M., Chotana, G.A.: Distribution of heavy metals in the soils associated with the commonly used pesticides in cotton fields. Scientifica **2016**, 7575239 (2016)

Design of a Rushton Turbine
for the Improvement of the Bioreactor
in the Wastewater Treatment Plant in the City
of Morococha (Carhuacoto)-Peru

Anieval Peña ⓘ, Steve Camargo ⓘ, Frando Condor(✉) ⓘ, Angela Tunque ⓘ,
and Ashley Verano ⓘ

Continental University, Huancayo 12002, Perú
{apenar,46935319,72146015}@continental.edu.pe

Abstract. The study is carried out in a domestic wastewater treatment plant (DWWTP) in the city of Morococha in Peru, with a population of 9 thousand inhabitants, at an altitude of 4200 m.a.s.l., has a processing capacity of $1620\,m^3$/day with a flow that is not constant, focuses on secondary treatment consisting of a sequential biological reactor (SBR) of aerobic technology. The problem is the excess flow in certain periods of time and the incoming wastewater was not processed in an optimal way, as an objective a redesign of the bioreactor was proposed, incorporating a Rushton Turbine of 6 horsepower (H.P.) of power with 6 propellers and dimensioned according to mathematical models, the results were the improvement of effluent quality for turbidity, dissolved oxygen, pH and residual chlorine, improving the reaction speed, and controlling the treatment flow, providing a better quality effluent to the receiving body which is a nearby river in this way the negative environmental impacts are reduced for the population.

Keywords: PTARD · Bioreactor · Aerobic · Settler · SBR · Biological · Turbine

1 Introduction

Currently, one of the greatest global challenges is to ensure water quality [1]. According to the World Health Organization (WHO), water quality is directly related to poverty, as municipal industrial wastes, as well as human products, are released daily into aquatic ecosystems. [2] since municipal industrial wastes, as well as human products, are released daily into aquatic ecosystems due to severe effects on microorganisms in low concentrations through wastewater [1, 2]. The activities carried out by the population generate an increase of heavy salts [3], organic matter and various toxic elements that affect and cause the degradation of water resources worldwide [4]. One of the challenges in the wastewater treatment plants are the biosolids waste, trying to find an alternative solution worldwide, focusing on the transformation processes, an adequate treatment and finally its final disposal, to obtain or convert it into important and mainly useful material to improve its productive chain [5]. 54% of Mexico's wastewater is not treated correctly

[4]. 25% of the population of Costa Rica only covers the sewage system [5]. Therefore, it is very convenient to study different wastewater treatment technologies for the development of the countries [6]. On the other hand, Colombia is facing the problem of water resources in order to be able to save water to avoid overexploitation of groundwater, which is mostly generated by groundwater pollution [7]. The main part is generated by pollution in the rivers, which is 90% of its population generating the discharge of wastewater without any treatment [8].

In Peru, the major problem is that 7 to 8 million Peruvians do not have access to drinking water supply or access to safe drinking water. [9] and the absence of sewage systems. Likewise, 24% of wastewater is treated and an unknown percentage of industrial wastewater is not treated [10]. According to the World Health Organization (WHO), water pollution represents a threat to public health. This is evidenced by the volume of 40 m^3/s of water that is not adequately processed and therefore is discharged directly into rivers and about 40,000 hect. are affected in agriculture [11].

The problems of this broad issue of wastewater management mainly in urban areas and in developing countries, are deficient and scarce in the treatment before its final disposal in water bodies, such as rivers as well as not treated enough for its reuse in industry and some services. In Mexico, city authorities often do not have the budget to do so, and they do not know of many alternatives to solve the problem, so the situation worsens every day as wastewater flows increase, posing a challenge to the authorities in charge of wastewater disposal [12].

Considering the problem of excess water in the bioreactor at the wastewater treatment plant in the Morococha Carhuacoto sector, the bioreactor is the focus. For this reason, an adequate design is proposed for the effluent liquids, taking as a fundamental basis the installation of the wastewater treatment plant that is in the place.

The wastewater treatment plant uses sequential biological reactor (SBR) technology, which are discontinuous reactors in which the wastewater is mixed with a biological sludge with air injection (process called wet combustion), its process capacity is 5 m^3/h, 110 m^3/day and the average monthly capacity is 115 m^3.

With such information from the plant an effluent surplus was highlighted giving as main point the proposal to improve the capacity of the (DWWTP), since it presents a Rushton turbine in the SBR bioreactor. [13] these effluents are discharged directly into the river. For this reason, agitators will be implemented to optimize a constant flow inside the bioreactor, improving the water quality of the effluent for turbidity, dissolved oxygen, pH and residual chlorine, improving the reaction rate, and controlling the treatment flow and water hygiene for the population as well as contributing to safeguarding the biodiversity of the city of Carhuacoto. The objective of wastewater treatment is to ensure that domestic and industrial processes are treated without endangering human health and with the least impact on the environment [14].

Installation of wastewater treatment systems
Is one of the strategies to reduce pollution in rivers. These systems aim to reduce organic and inorganic pollutants in these waters through physical, chemical and biological processes. [4] in this regard. The Rushton turbine is of the radial flow type showing efficiency in its operation, thus it is determined that it is viable for wastewater treatment [15].

1.1 Environmental Standards in Peru

Only two levels of headings should be numbered. Lower-level headings remain unnumbered; they are formatted as run-in headings.

Table 1. Environmental quality standards.

Parameters	Unit of measure	Primary contact	Secondary contact
Biochemical Oxygen Demand (BOD5)	mg/l	5	10
Chemical Oxygen Demand (COD)	mg/l	30	50
Dissolved Oxygen (minimum value)	mg/l	≥ 5	≥ 4
Hydrogen Potential (pH)	pH unit	6,0 a 9,0	**
Turbidity	UNT	100	**

The impact indicators include the Environmental Quality Standards (EQS) of the water shown in Table 1, which reports the authorization of discharges of treated wastewater. Applying the turbine design, the parameters are within the range.

(LMP). It is the measure of the concentration or degree of elements, substances or physical, chemical, and biological parameters that characterize an emission, which when exceeded causes or may cause damage to health, human welfare, and the environment. Its compliance is legally enforceable by MINAM (Ministry of the Environment) and the agencies that make up the Environmental Management System.

Table 2. Physical parameters.

Sampling time	Inflow of treated effluent to the PTARD – Initial Chamber				
	PH (6.5–8.5)	$O_2(\geq 4$ mg/lt)	T°C(<35 °C)	Turbidity (<20NTU)	Chlorine (0.5–1.5 mg/l)
08:00	8.58	5.01	13.1	26.4	0.70
13:00	8.59	5.17	14.7	25.5	0.68
17:00	8.57	5.13	14.0	22.8	0.59

According to the regulations, Table 2 shows that the Maximum Permissible Limits (MPL) are exceeded in the following parameters such as pH, dissolved oxygen, settled solids, turbidity, and oxygen. A Rushton turbine will be implemented in the wastewater treatment process to obtain better results from the treated water.

2 Methodology

A Rushton turbine is designed with the mathematical criteria complementing with the Solid works program, AutoCAD for the elaboration of the design and operation for the

correct functioning in the wastewater treatment in the city of Morococha, mainly in the secondary treatment, inside the bioreactor SBR [16] and aerobic for the retention of the liquid, taking into account the diameters of the tank, considering the established dimensions that are: Agitator measurements, impeller bore distance, impeller diameter, length and width of blades, deflector plates dimensions [17].

Generating the efficiency of the water velocity holding capacity by applying the equation with the Reynolds Number is $2.36 * 10^{-14}$ and the power number is $2.28 * .10^{-14}$ to identify the angular velocity is 1917. Where the Rusthon turbine has six deflector plates with a width of 1/10.

The Rushton turbine has the function of analyzing fluids using the impellers at the same time being constant with speed, air, bubbles can also operate at low agitation conditions from 200 rpm to 600 rpm [15].

2.1 Final Indicators

Retention time is efficient.
Regarding the retention time, it will be between 120 and 240 h since it presents a more efficient reduction of organic matter as well as the reduction of thermotolerant coliforms [18].

The SBR reactor is a viable alternative, as it shows efficiency in the treatment of industrial wastewater with respect to organic load, mainly in the removal of Total Organic Carbon (TOC) showing optimal effluent quality results [19]. The SBR Bioreactor process is divided into two processes: the first one consists of the biological removal of phosphorus (EBPR) and denitrification (DN) in the main reactor (SBRP) [20], where a reduction of BOD, TSS and total nitrogen is obtained.

The reactor consists of two zones: preliminary and main. Both areas are separated by a baffle wall. The wastewater continuously reaches the primary zone and enters the main reactor through openings in the lower zone of the baffle. Ensuring that the inflow of raw water does not affect the quality of the wastewater in the sedimentation stage [21].

Aerobic reactor with biofilter with aeration for different aeration rates in the reactor, showing that the process achieves higher nutrient removal with carbon demand Low and efficient aeration rate [20].

As this interaction progresses, volatile suspended solids concentrations decrease because microbial cells die faster than newly synthesized cells, which determines the rate of degradation of the substances and their specific residue [13].

3 Results

3.1 SBR Reactor Analysis

Sequential Biological Reactor (SBR) [16]. This bioreactor processes anaerobic microorganisms [22]. The SBR system consists of at least four cyclic processes: filling, reaction, sedimentation and emptying of both wastewater and sludge [23]. The design of the bioreactor is cylindrical as it has several advantages, such as less possibility of dead sludge

formation, and the size, volume, collection point and flow rate can be manipulated. The bioreactor design is basically implemented for "Organic Matter Removal". Which includes process steps, filling, aeration agitation, sludge settling and discharge of treated water [22]. This is the only bioprocess in which reaction, aeration and SBR cleaning are combined in the same vessel. In the first stage, known as static filling, excess water is introduced into the system under static conditions. Filling can be dynamic if it occurs during the response time. In the second stage of the cycle, the wastewater is mechanically mixed to remove any surface scum and prepare the microorganisms for oxygen uptake [23]. In this second (reaction) stage, air is introduced into the system. The reaction stage is a time-varying process in which the wastewater is continuously mixed and aerated, allowing biodegradation to occur. The third cycle, known as the sedimentation phase, creates resting conditions throughout the basin where the sludge can settle. In the final stage, or emptying phase, the treated water is sucked out of the tank by the removal system over the liquid surfaces. Finally, the sludge generated can be filtered clean to maintain the concentration at a constant level [23].

3.2   Diagram Your Capabilities

In the Fig. 1, the improved design of the sequential biological reactor (SBR) is shown, being more effective and homogeneous in the treatment of wastewater, incorporating the Rushton turbine, which is more suitable for the removal of organic matter.
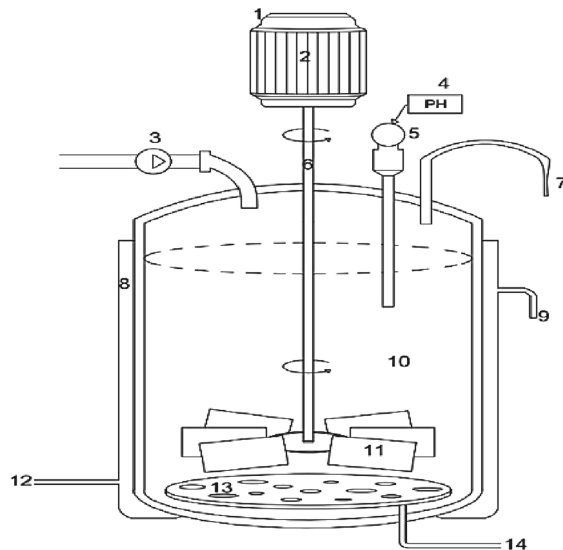
Fig. 1. Design of the bioreactor with the turbine.

The parts of the turbine bioreactor can be seen in Table 3, which consists of 14 parts, as shown in Fig. 1. The design of the Bioreactor implementing the Rushton turbine.

Table 3. Turbine part of bioreactor.

Nª	Part of the turbine bioreactor
1	Agitation System
2	Engine
3	Feed Pump
4	PH Controller
5	Acid/Base Container and Pump
6	Agitator shaft
7	Waste
8	Jacket
9	Cooling Water Outlet
10	Crop Mixture
11	Rushton Turbine
12	Cooling Water Inlet
13	Air Bubble Distributor
14	Sterile Air

3.3 Turbine Analysis

The Rushton turbine has a modern technology that recovers wastewater with oxygen injection (process called wet combustion). It has a process capacity: 5 m^3/h and with a process capacity per day: 110 m^3 and with an average/monthly process: 115 m^3. The efficiency of oxygen transmission is improved by the design of the Rushton turbine, as well as the energy saving, therefore, the results show the operation of the system that favors the efficient mixing of water and oxygen. It was possible to determine the oxygen transmission rate which was influenced by the size and number of bubbles caused by the type of aeration system as it reduces the low availability of dissolved oxygen [24].

3.4 Overall Dimensions

It was determined with respect to using the implementation of the turbine, considering the data of the pond measurements, the respective measurements to be included in the agitator will be shown below.

In the turbine, the measurements were considered, which was carried out with the calculations of the agitator in Table 4, taking into account the general dimensions.

Reynolds number (Re)

For the Reynolds value, the characteristic of the fluid is identified if it is laminar or turbulent, defining that the change from laminar to turbulent regime is slow [25], as it goes through a transition will be presented below:

Table 4. Agitator power calculation.

Dimensions	Unit
Distance bottom to base of impeller(E)	345 mm
Impeller diameter (Da)	345 mm
Pallet length (g)	90
Pallet width (W)	70
Dimensions of baffle plates (4 each @ 45°)	
Plate width (J)	205
Space between plate and tank (f)	20

Reynolds is 2.36 * 10^{-14} which is within the laminar regime range: Re < 10 laminar favoring the design.

Reynolds number

$$Re = \frac{Nd^2 * \rho}{c}$$

(1)

Table 5. Description of Eq. 1

Dimensions	Unit
Density Caustic Soda (ρ)	1100
Viscosity (μ)	0.001
Angular Velocity (N)	1917
Stirrer diameter (d)	335

Applying the Reynolds Number formula, Eq. 1 was found as shown in Table 5, obtaining the caustic soda density, viscosity, angular speed and the diameter of the agitator, with their respective results.

Power number (Np)

$$Np = \frac{P}{N^3 d^5 * \rho}$$

(2)

In Eq. 2, the power number (Np) was calculated to determine the angular velocity, angular diameter and caustic soda density as evidenced in Table 6.

Table 6. Description of Eq. 2

Dimensions	Unit
Angular Velocity (N)	1917
Stirrer diameter (d)	335
Density Caustic Soda (ρ)	1100

Table 7 below shows the KL and KT constants for ponds with six baffle plates with a width of 1/10 of the pond diameter that was considered for turbine optimization.
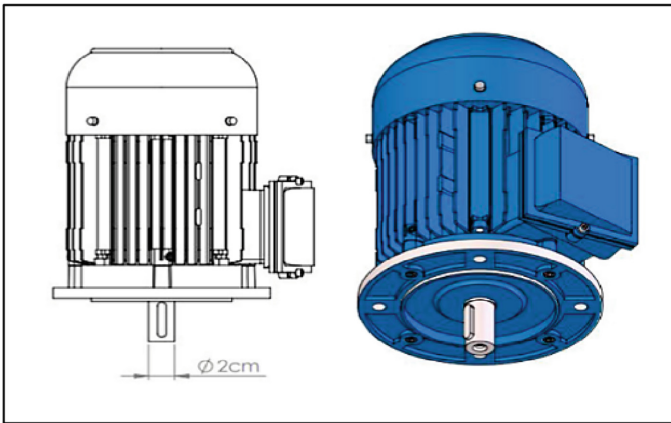
Fig. 2. Three phase electric motor

Table 7. Equation 2

Impeller type	KL	KT
Square pitch propeller, three blades	41.0	0,32
2 pitch propeller, three blades	43,5	1,00
Turbine, six flat blades	71,0	6,30
Turbine, six curved blades	70,0	4,80
Fan turbine, six blades	70,0	1,65
Two flat blades turbine	36,5	1,70
Closed turbine, six curved blades	97,2	1,08

The Fig. 2, shows the most efficient three-phase motor with a good weight, size and power ratio, since it is of the squirrel cage type and has one or several groups of coils

distributed 120° apart in its circular state. Being more compact and lighter than the initial engine.

In the industrial environment, the three-phase motor is used because it is an efficient motor with a good ratio of weight, size, and power, since it is of the squirrel cage type, where the motor has one or several groups of bovines distributed at 120° of distance in its circular stator, being more compact and lighter where the motor is very efficient.

The Fig. 3 shows one of the most widely used types of propellers in the industry, the 6-blade straight radial propeller, also known as the 6-blade Rushton turbine [26]. It is suitable for moving low-viscosity, high-velocity fluids. It is used for gas-in-liquid dispersion, solid dispersion, insoluble liquid mixing and heat exchange. Distributes energy evenly. Mixed flow type [27] Power 6 HP.
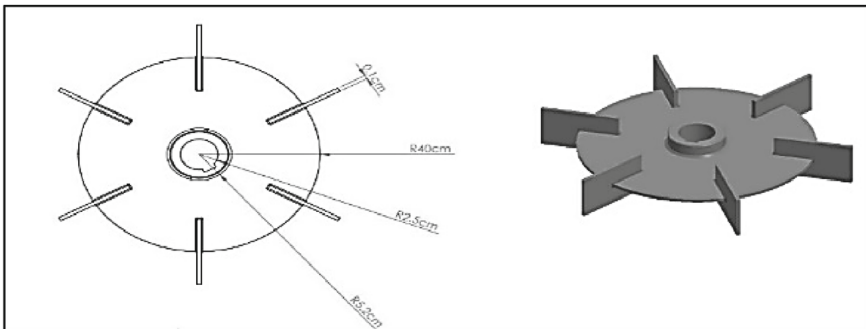
Fig. 3. Rushton turbine propellers
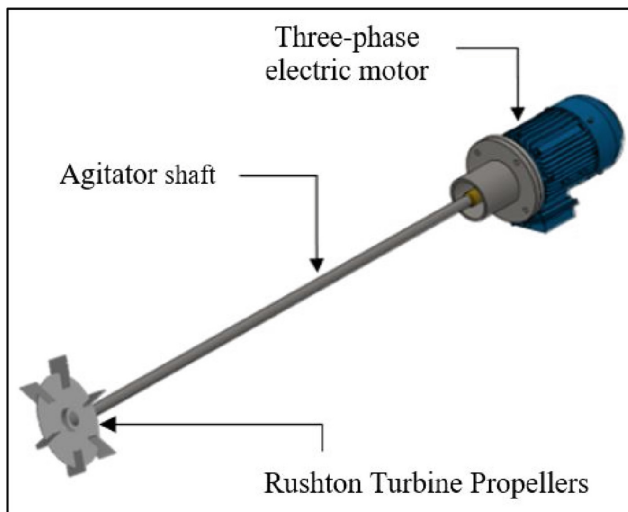
Fig. 4. Design and Shaft, turbine whit coupling to the electric motor

According to the Fig. 4, the Rushton turbine was designed to achieve optimization within the bioreactor, thus improving dissolved oxygen, pH, and residual chlorine, improving the reaction rate, and controlling the treatment flow, avoiding excess wastewater and improving people's health and contributing to safeguarding biodiversity.

3.5 Effluent Quality

Table 8. Physical and chemical parameters of the effluent.

Sampling time	Inflow of treated effluent to the PTARD – Initial Chamber				
	PH (6.5–8.5)	O_2($\geq$4 mg/lt)	T°C($<$35 °C)	Turbidity ($<$20NTU)	Chlorine (0.5–1.5 mg/l)
08:00	8.29	4.01	1301	19.2	0.57
13:00	8.31	4.17	14.7	18.3	0.63
17:00	8.22	4.13	14.0	18.7	0.55

According to Table 8, it can be determined that the data with respect to the effluent output has a favorable result that shows a decrease in the three samples presented, which indicates that with the implementation of the Rushton turbine in the bioreactor, the quality parameters improve.

4 Conclusions

The implementation of the Rushton turbine design for the wastewater treatment plant, with respect to the flow rate, obtained adequate results since it is within the parameters established according to the Peruvian Environmental Quality Standard (PEQS) and Maximum Permissible Limits (MPL).

The speed is kept constant, due to the design of the Rushton turbine, which consists of six propellers, improving the efficient process performance of the SBR bioreactor in the domestic wastewater treatment plant.

With respect to the turbidity parameter the following result was manifested which was from 26.4 NTU to 19.2 NTU showing a remarkable decrease of 7.2 NTU due to the design of the Rushton turbine in the SBR bioreactor.

The main process for the implementation or planning of any design is the approval and evaluation of all possible changes to achieve the desired results. Water is available for reuse in irrigation.

The quality of the influent and effluent have a favorable difference when implementing the Rushton turbine design, since there is a significant change in the following parameters: pH with a decrease of 0.37, turbidity with a variation of 8.1 NTU in the wastewater, Chlorine is reduced by adding to the wastewater treatment plant at 21.43% mg/l, O2 decreases by 1.16 mg/l.

References

1. Borja-Aragón, J.L., La Garza, J.A.R.D., Ríos-González, L.J., Garza-García, Y., Rodríguez-Garza, M.M., Martínez-Amador, S.Y.: Domestic wastewater treatment using Chlorella vulgaris in an airlift bioreactor. Mex. J. Biotechnol. **2**(2), 40–52 (2017). https://doi.org/10.29267/mxjb.2017.2.2.40
2. Organización Mundial de la Salud: Organización Mundial de la Salud (2019). https://www.who.int/es/news-room/fact-sheets/detail/drinking-water. Accessed 23 Feb 2022
3. Madera, C.A., Silva, J.P., Peña, M.R.: Sistemas combinados para el tratamiento de aguas residuales basados en tanque séptico - filtro anaerobio y humedales subsuperficiales. Ing. Y Compet. **7**(2), 5 (2011). https://doi.org/10.25100/iyc.v7i2.2512
4. Zacarías, V.H.R., et al.: Hidroquímica y contaminantes emergentes en aguas residuales urbano industriales de Morelia, Michoacán, México. Rev. Int. Contam. Ambient. **33**(2), 221–235 (2017). https://doi.org/10.20937/RICA.2017.33.02.04
5. Porras, Á.C., González, A.R., Gómez, F.E.G.: Análisis de la dinámica biológica presente en un sistema piloto de lombricultura para el manejo de biosólidos provenientes de aguas residuales. Rev. Ing. Univ. Medellín **12**(22), 13–23 (2013). https://doi.org/10.22395/rium.v12n22a1
6. Rincón, C.G.B., Higuera, D.A.S.: Análisis del Uso de Biorreactores de Menbrana Para Tratamiento de Aguas Residuales y Posible Implementeción en Colombia, pp. 14–15 (2017)
7. Daus, A.: Almacenamiento y recuperación de agua en acuíferos: Mejoramiento de la seguridad en el abastecimiento de agua en el Caribe. Oportunidades y Desafíos. Banco Interamericano de Desarrollo (2019). https://publications.iadb.org/publications/spanish/document/Almacenamiento_y_recuperación_de_agua_en_acuíferos_Mejoramiento_de_la_seguridad_en_el_abastecimiento_de_agua_en_el_Caribe._Oportunidades_y_desafíos_es.pdf. Accessed 23 Feb 2022
8. Madera, C.A.: Sistemas combinados para el tratamiento de aguas residuales basados en tanq...: EBSCOhost, Ingeniería y Competitividad Revista Científica y Tecnológica. https://web.p.ebscohost.com/ehost/detail/detail?vid=38&sid=27a8f6ce-85fb-47f8-a6b0-f3161a841252%40redis&bdata=Jmxhbmc9ZXMmc2l0ZT1laG9zdC1saXZl#AN=22956366&db=egs. Accessed 11 Dec 2021
9. de Miraflores, M.: Un crimen recurrente: la falta de agua potable. Municipalidad de Miraflores (2021). https://www.miraflores.gob.pe/un-crimen-recurrente-la-falta-de-agua-potable/. Accessed 11 Mar 2022
10. Tong, D.B.C.: Direccion de gestión de la calidad de los recursos hídricos. ANA Perú (2012)
11. Arsénico: "Arsénico". Organizació n Mundial de la Salud (2018). https://www.who.int/es/news-room/fact-sheets/detail/arsenic. Accessed 23 Feb 2022
12. Ramón, V.L.: Infraestructura Sustentable: Las Plantas de Tratamiento de Aguas Residuales. Quivera. Rev. Estud. Territ. **12**(2), 58–69 (2010)
13. Paola, L., Guevara, B., Plata, D.P.: Construcción y Operación de Reactor SBR a escala para tratamiento de Vinaza proveneniente de un Ingenio Azucarero (Valle del Cauca), p. 15. Univ. el Bosque (2019)
14. Barrantes, E.A.B., Nuñez, M.C.: Eficacia del tratamiento de aguas residuales de la Universidad de Costa Rica en la Sede de Occidente, San Ramón, Costa Rica. UNED Res. J. **9**(1), 193–197 (2017). https://doi.org/10.22458/urj.v9i1.1697
15. Jenish, I., Appadurai, M., Irudaya Raj, E.F.: CFD analysis of modified rushton turbine impeller. Int. J. Sci. Manage. Stud. 8–13 (2021). https://doi.org/10.51386/25815946/ijsms-v4i3p102
16. Mauricio, C.E.: Evaluacón del Funcionamiento de un Reactor Biológico secuencial (SBR) contruido para la remoción de materia orgánica en las aguas residuales Domésticas, vol. 25, no. 1 (2020)

17. Chambergo, J.C., Valverde, Q., Pachas, A.A., Yépez, H.: Estudio del Comportamiento Fluido-Dinámico de un Agitador a Escala Reducida Estudio del Comportamiento Fluido-Dinámico de un Agitador a Escala Reducida Mediante Simulación Numérica Study of the Fluid-Dynamic Behavior of a Reduced Scale Stirred Tank throug. Inf. Tecnológica **28**(3), 37–46 (2017). https://doi.org/10.4067/S0718-07642017000300005

18. Poma, D.K.C., Vera, G.M.C., Bedoya-Justo, E.: Eficiencia de Eisenia foetida, Eichornia crassipes e hipoclorito de calcio en la depuración de aguas residuales domésticas en Moquegua, Perú. Ecol.a Apl. **20**(1), 83 (2021). https://doi.org/10.21704/rea.v20i1.1692

19. Restrepo, A., Rodríguez, D.C., Peñuela, G.A., Restrepo, A., Rodríguez, D.C., Peñuela, G.A.: Eficiencia de un reactor SBR para la remoción de la materia orgánica presente en el agua residual de una industria de teñido de flores. Rev. ION **34**(1), 47–59 (2021). https://doi.org/10.18273/REVION.V34N1-2021005

20. Santa Cruz, J.A., Scenna N.J., Mussati, M.C.: Análisis económico de un proceso basado en reactores discontinuos secuenciales (SBR) para la reducción de nutrientes biológicos de aguas residuales. Repositorio Institucional CONICET Digital (2017). https://ri.conicet.gov.ar/handle/11336/75223. Accessed 15 Mar 2022

21. Nuevo, D.: Reactor biologico secuencial (SBR) | Formación de ingenieros. TECPA Ingeniería y Medio Ambiente (2015). https://www.tecpa.es/reactor-biologico-secuencial-sbr/. Accessed 17 Mar 2022

22. Durant Carbajal Estela Alejandra, M.C.F.I.: Diseño y construcción de un reactor biológico secuencial (SBR) para el tratamiento de aguas Residuales lácteas procedentes de la Planta Agroindustrial del Perú S.A.C. Majes – Arequipa. Repositorio Universidad Católica de Santa Maria (2012). http://tesis.ucsm.edu.pe/repositorio/handle/UCSM/3786. Accessed 17 Mar 2022

23. Reyes, W.: Optimización del tratamiento de aguas residuales domésticas mediante la implementación del sistema MBBR en la provincia Cayllo. Univ. Nac, Mayor San Marcos (2020)

24. Amy, L.P.A.: Influencia del tipo de sistema de aireación difuso en la eficiencia de transferencia de oxígeno en aguas residuales domésticas Huancayo-2020 | Arlitt Lozano Povis - Academia.edu (2020). https://www.academia.edu/49827748/Influencia_del_tipo_de_sistema_de_aireación_difuso_en_la_eficiencia_de_transferencia_de_oxígeno_en_aguas_residuales_domésticas_Huancayo_2020. Accessed 25 Feb 2022

25. Alderson, D., Charles, J., Wall: Capítulo Escalamiento. es el de controlar parámetros fundamentales a escala piloto con condiciones ideales, para. Japanese Soc. Biofeedback Res., pp. 104–105 (1992). https://doi.org/10.20595/jjbf.19.0_3

26. Martínez Nelis, F.M., Valencia Musalem, A.: Estudio numérico de la fluidodinámica de un estanque de agitación utilizando método de mallas deslizantes, p. 2. Repos. Académico la Univ. Chile (2010)

27. Reinhardt, A.T.: Principios Básicos del Diseño de Biorreactores. Parte C: Sistemas de Potencia de Agitación y Mezclado. Bioreactores Biotecnología Practica y Aplicada (2021). https://www.academia.edu/52368706/Principios_Básicos_del_Diseño_de_Biorreactores_Parte_C_Sistemas_de_Potencia_de_Agitación_y_Mezclado. Accessed 17 Mar 2022

Numerical Analysis of Ferro-Alumino-Zirconium Particle Sedimentation Under Passive Waste Pre-treatment Scenario

Ralph Carlo Evidente[1]([✉]), Michelle Almendrala[2], Zhane Ann Tizon[2], Bonifacio Doma[2], and Marc Jazer Esguerra[2]

[1] POSTECH, Pohang, Gyeongbuk 37673, South Korea
`ralphcarlo@postech.ac.kr`
[2] Mapúa University, 1002 Manila, Philippines

Abstract. Computational Fluid Dynamics-Discrete Element Method (CFD-DEM) coupling algorithm was used in this study to assess the sedimentation and coolability of stainless steel, aluminum, and zirconium solid particles in a liquid pool. This phenomenon is associated with the micro-to-nanosized multi-particle cooling phase encountered in metal powder and hazardous solid waste sedimentation pre-treatment facility. To determine the effect of fluid as simulant, a sedimentation scenario was simulated with multicomponent particle system (500 K) entered in a cylindrical pool, and cylindrical and cylindrical-trapezoidal configuration. All the computational frameworks involve two pool simulants: air and water. This numerical analysis focused on the characteristics of particle falling (i.e. falling time and average velocity) and of particle agglomeration (i.e. bed height distribution and melt spreading distance). Numerical results in cylindrical configuration showed good agreements with other computational data from previous studies using simulant of water. The new cylindrical-trapezoidal configuration shows promising results, where spreading dominates over agglomeration.

Keywords: CFD-DEM · Sedimentation · Coolability · Ferro-alumino-zircon

1 Introduction

Discharges from steelmaking electric furnace consist mainly of zircon concentrate, aluminum powder, and ferrous alloys collectively called as debris bed, which can be recycled back to smelting process unit through the affordable use of passive coupled sedimentation and coolability process. There have been several experimental and numerical researches concerning the assessment of debris bed coolability. Recently, the importance of the debris bed characteristic was shown in the numerical approach for the overall progression of the ex-vessel scenario [1–3]. Sensitivity and uncertainty analyses of debris bed cooling have been studied, and results show that long-term coolability has been sensitive from the debris bed characteristics such as bed height. This is vital, since coolant

ingression is associated with the debris bed pressure drop, which is heavily dependent on the particle size and shape [4, 5]. The particle geometry affects the two-phase flow in particle bed, and also affects the pressure drop that controls the water ingression.

However, there have been limitations in investigating the transient state of sedimentation, because of the following: (1) particle size variation was not considered, (2) actual coolant in the process unit might have a different fluid property as compared to what the experimental and numerical studies used, (3) CFD validation was not given, and (4) geometrical configuration has always been the same (i.e. cylindrical cavity). Most importantly, few studies associated with the numerical approach have rarely been performed, given its advantage in visualizing the transient state at high pressure and temperature condition. Hence, the numerical approach will help in reducing the uncertainties in the designs with regard to passive sedimentation and coolability.

The codes used in this study incorporated Eulerian-Lagrangian algorithm for the debris particle sedimentation and considered the interaction between solid particles and two-phase (fluid-solid) with turbulence factor that highly affects on the debris spreading. With its consideration in three-dimensional analysis, the Computational Fluid Dynamics-Discrete Element Method (CFD-DEM) coupling algorithm was used in this study, which also has greater applications in powder technology, food science, civil engineering, where the hydrodynamic interaction between solid and fluid particles is significantly considered. Using cylindrical and cylindrical-trapezoidal configuration, respectively, the multivariate particle size simulation focused on the characteristics of particle falling (falling time and average velocity) and that of particle agglomeration (bed height distribution and melt spreading distance).

2   Numerical Methodology

2.1   Cylindrical Cavity

To verify the applicability of the CFD-DEM coupling algorithm to the simulation of the solid particle sedimentation in the liquid pool, a comparison based on an experimental condition with spherical particles and quiescent pool without vapor phase with the previous numerical data was performed [1, 6]. The experimental facility is comprised of a cylindrical acrylic pool with an inner diameter of 375 mm and a depth of 1020 mm. The cylindrical pool was filled with water up to 825 mm from the bottom of the catcher plate. A funnel with a 92 mm long nozzle is located at the center of the cylindrical pool, about 720 mm above the catcher plate. The nozzle inlet was initially blocked with a plug, and solid particles with total volume of 5 L were initially settled in the funnel. The plug was pulled out thereafter and the momentum of the solid particles was induced by free fall to the bottom of the catcher plate. Here, no initial convection of fluid exists [6, 7].

To consider the multivariate simulation in a cylindrical cavity, the configuration to be simulated is exactly similar to previous experimental and numerical studies. The range of ratios (3.0 to 10.0) of the fluid cell size to the particle diameter for the CFD-DEM analysis is considered reasonable based on previous studies [8–11]. By way of a grid convergence test, the ratio of the minimum cell size to the particle diameter in this study was determined to be 3.0.

In this simulation, the effect of initial gas entrainment was negligible since the nozzle inlet was submerged in the water pool 125 mm below the water surface. Moreover, a detailed analysis for the gas phase above the water surface was not considered in this condition, because the effect of natural circulation on the free surface was negligible during the particle sedimentation. Using OpenFOAM for CFD and LiGGGHTS for DEM and 28 numerical cores, initialization was done using the input conditions in Table 1, parameter variables in Table 2, and case setup in Table 3.

Table 1. Input condition for solid particle and liquid phase

Parameter	Value
Particle Number	63800
Poisson Ratio (υ), -	0.27
Stiffness Correlation Constant (α_{tn}), -	300
Damping Correlation Constant (α_{cn}), -	0.03
Sliding friction coefficient (μ_s),-	0.3
Rolling friction coefficient (μ_r),-	0.1
Time step for DEM (Δt_{DEM}), s	1.0×10^{-5}
Time step for CFD (Δt_{CFD}), s	1.0×10^{-4}

Table 2. Multivariate particle property

Material	Density	Particle diameter	Volume fraction
Al_2O_3	3600	0.002	0.25
Al_2O_3	3600	0.004	0.25
ZrO_2	6000	0.006	0.25
Stainless steel	7800	0.006	0.25

Table 3. Cases for the cylindrical cavity configuration

Case	Cone attached	Air	Water
Case 1	✓	✓	
Case 2	✓		✓
Case 3		✓	
Case 4			✓

2.2 Cylindrical-Trapezoidal Cavity

The last part of this numerical study involves the attachment of a trapezoidal cavity with a length of 400 cm, height of 82.55 cm, and hole height of 10 cm, as presented in Fig. 1. This newly proposed configuration has not yet been performed experimentally, but aims to prevent particle agglomeration that threatened the pressure vessel integrity. It is subdivided into two simulations: (1) with no jet case considered (i.e. passive case) and (2) with melt jet. Particle properties and variables can be seen in Table 4.

Table 4. Particle property for the cylindrical-trapezoidal cavity configuration

Material	Density	Diameter	Volume fraction
Stainless steel	7800	0.006	0.70
Al_2O_3	3600	0.004	0.30
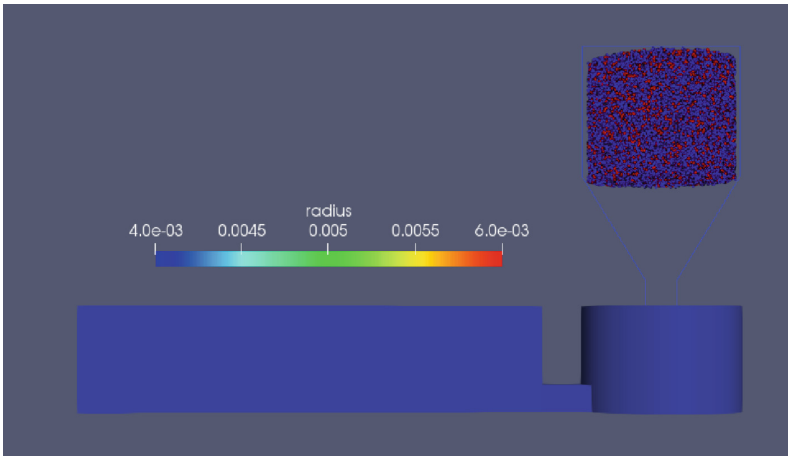
Fig. 1. 63800 particles were inserted in a hopper located above the cylindrical chamber. The air-water case task is divided with (1) no initial velocity, and (2) an initial jet velocity of 0.5 m/s.

3 Results and Discussion

The multivariate simulation visual results can be seen in Fig. 2. The chaotic nature of the particles with the simulant of air prevents them to settle smoothly and slowly. During the early jet phase, smaller particles tend to be the first one to settle in air case and as it progresses, they tend to surround the bigger ones, whereas opposite is observed in water case. Figure 3 shows that bigger particles tend to get concentrated around the end part of side wall for this air case simulation; meanwhile, water case shows that bigger particles tend to settle on central part, surrounded by the smaller particles.

Figure 4 indicates the solid particles in water tend to settle longer than air as seen in particle falling temporal profile. Interestingly, the complete settling temporal profile shows that those with attached cone on bottom part of cavity tend to settle completely and faster than those with none. On the other hand, it has been found out [7–14] that lateral dispersion depends on particle falling time which holds true in Fig. 5. Dispersion width for water case is much longer than those in air, from which the former tends to settle much slower. Although the trend is increasing for all cases, the data from water case give much larger difference with regard to the slope between time of 0.20 and 0.30 s. Finally, Fig. 6 signifies that those with no attached cone tend to have lower bed height; moreover, since water case produces longer falling time, it produces higher bed height [4].
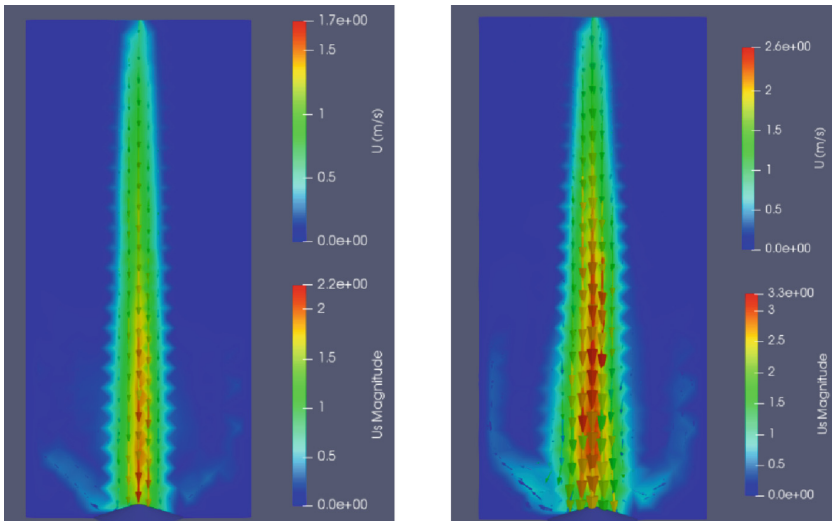
Fig. 2. Vector plot of simulant flow in cross-sectional view at transient state (~5 s) for (a) water (left) and (b) air (right).

The last part of this study consists of cases, which can capture the effect of physical phenomena from 63800 particles inserted at the hopper that can be found on the top of cylindrical cavity as it jets into a pool filled with either of air or water. It is subdivided into two: (1) no initial particles' velocity (*Case name: Rosau_fluid*) and (2) an initial velocity of 0.5 m/s (*Case name: Rosau_fluid_velocity*).
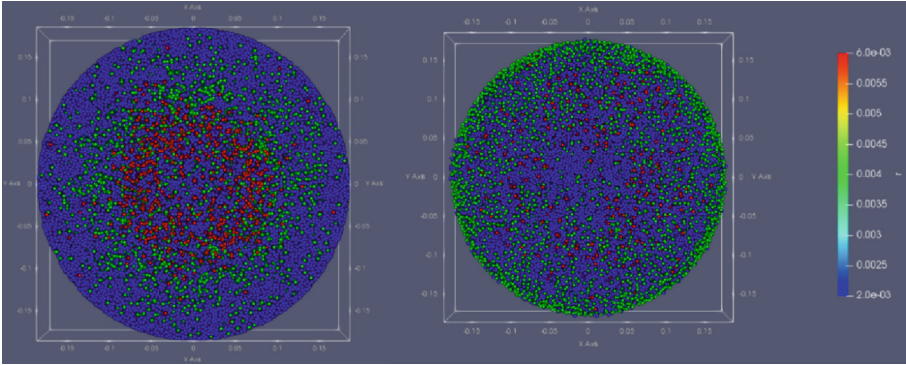
Fig. 3. Topview of particle bed after simulation endtime for (a) water (left) and (b) air case (right).
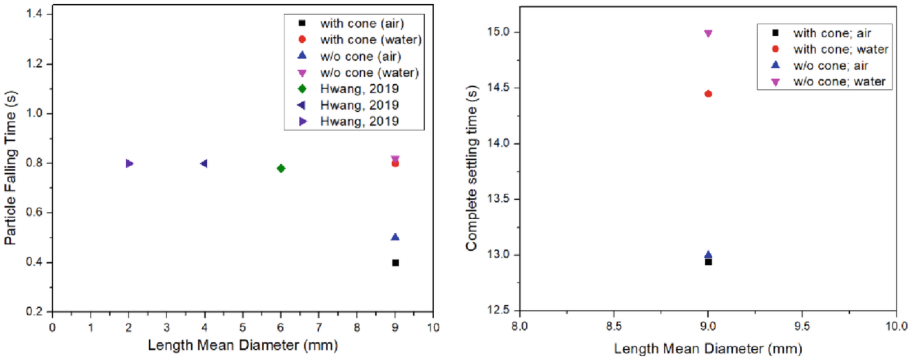
Fig. 4. Particle falling according to particle diameter (left) & complete settling time (right).

Particle Falling time is defined as the falling duration of the solid particles from the nozzle exit to the bottom of the catcher plate. As observed in Fig. 7a and Fig. 7b, the water simulation among all the four cases took the longest time for the particles to fall down, followed by air, air with initial particles velocity, and water with initial particles velocity, respectively. Surprisingly, the last two were closest in value, which indicates that the initial velocity plays a significant role in improving the settling time of the particles.
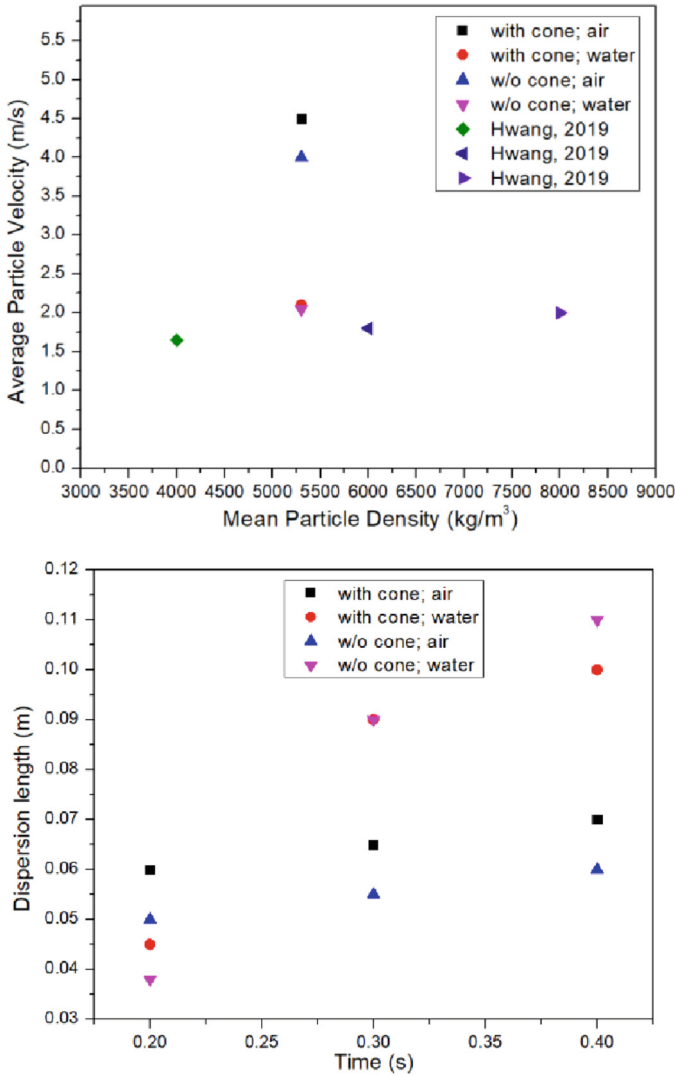
Fig. 5. Average particle velocity according to particle density (top) & temporal particle dispersion width (bottom).

The indication of having a high value of particle bed height even the configuration has changed to cylindrical-trapezoidal cavity means a possibility of agglomeration that prevents the coolant penetrating into the debris bed, and the bed reaches a non-coolable state, which threatens the containment integrity. For this, it is observable in the Fig. 7c that water case has the most maximum bed height, followed by water case with initial particles velocity, air, and air with initial particles velocity, respectively.
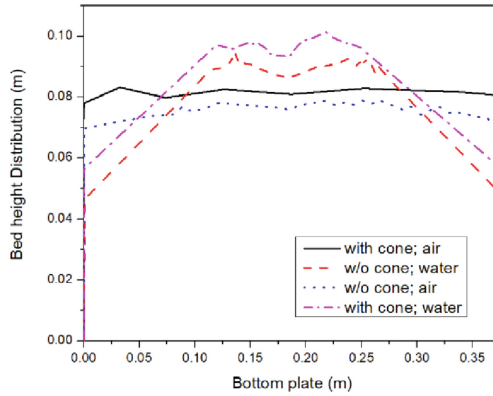
Fig. 6. Particle bed height distribution
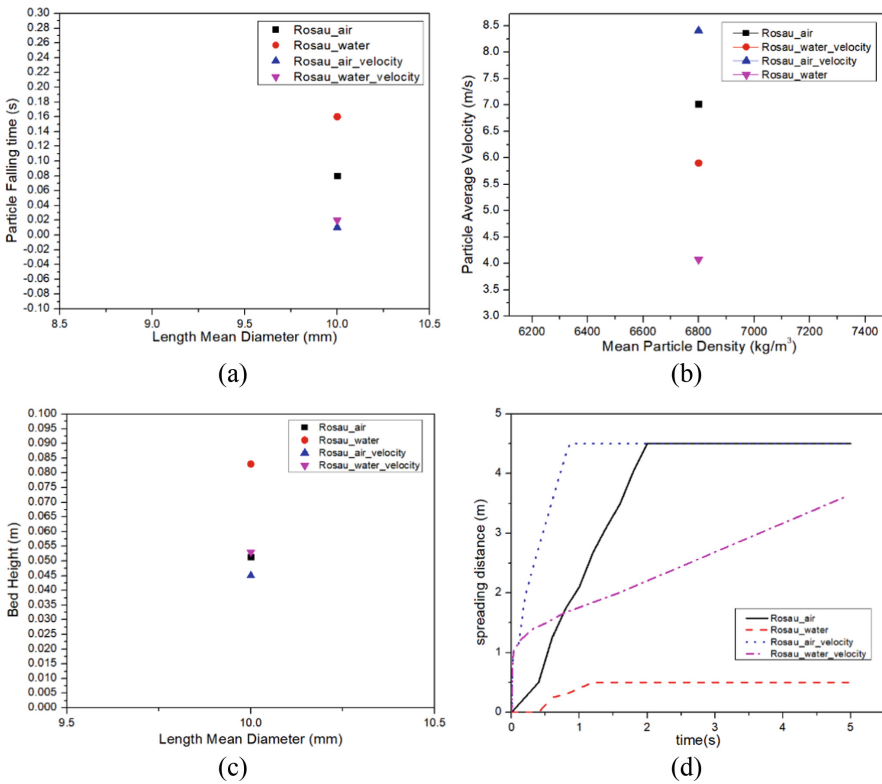
Fig. 7. (a) Particle falling time, (b) Average particle velocity, (c) Bed height distribution, and (d) Temporal spreading distance

All the simulations were set at end time of 5 s, and all the cases have all their particles settled by such. Water case alone only reached up to the end part of the neck

of the cylindrical-trapezoidal cavity; hence, as seen in Fig. 7d, among all the cases, it spreads the least. Next is the water case with initial particles velocity, which has a linear plot with respect to time. Although it did not achieve a constant trend after the linear peak, one can intuitively tell that by increasing the particles velocity would mean the further that these particles would disperse in the horizontal direction. The trend between the air case and air with initial velocity case is almost similar, with almost the same slope on the linear graph, except that the latter has reached its peak much faster by 1.14 than the former.

4   Conclusion

Investigating the debris bed particle sedimentation is an important issue in the aspect of ex-vessel phase coolability that aims to describe particle falling (falling time and av-erage velocity) and that of particle agglomeration (bed height distribution and melt spreading distance). To this end, the Computational Fluid Dynamics-Discrete Ele-ment Method (CFD-DEM) coupling algorithm was utilized in this study to assess the sedimentation and coolability of solid particles in a liquid pool. Previous numerical approaches have not fully investigated the effect of changing the simulant from water to gas state (i.e. air) and the multivariate conditions which satisfy that actual passive progression of high-temperature ferro-alumino-zircon particle sedimentation; moreover, most of 3D analyses in the past were only focused in the cylindrical configuration.

The first part of this study shows how multivaried-sized particles are distributed differently depending on the fluid simulant used. Particle bed distribution is depend-ent on the cone attachment to the bottom cavity and property fluid, in which the latter alters the dispersion width seen on the early phase of melt jet phenomena. Even as the particle sizes were varied, numerical results in cylindrical configuration showed good agreements with other computational data from previous studies utilizing water as simulant. Finally, the new cylindrical-trapezoidal configuration shows promising results, with spreading dominates over agglomeration. Therefore, the algorithm has potential in reducing uncertainties in cooling of the ex-vessel debris bed.

It should be noted that the simulation target has some limitations because of lack of experimental data in the proposed cylindrical-trapezoidal cavity to this date, of the sphericity of the particle, and of the isothermal conditions. In addition, the pre-sent algorithm has a computational constraint for calculating the real condition. Hence, large-scale design, non-spherical particles, and phase changes should be con-sidered to shed light behind the debris particle sedimentation phenomena. Especially the trajectory of solid particles is sensitive to the vigorous flow with evaporation, so that the prediction of particle sedimentation in gas-liquid two-phase regime should be performed in the near future.

References

1. Hwang, B., Park, H.S., Jung, W.H., Lee, M., Kim, M.H.: Numerical validation and investi-gation for the sedimentation of solid particles in liquid pool using the CFD-DEM coupling algorithm. Nucl. Eng. Des. **366**, 110364 (2019)

2. Hwang, B., et al.: Sensitivity and uncertainty analyses of ex-vessel molten core cooling in a flooded cavity during a severe accident. Nucl. Eng. Des. **328**, 121–133 (2018)
3. Hwang, G., et al.: FARO tests corium-melt cooling in water pool: roles of melt superheat and sintering in sediment. Nucl. Eng. Des. **305**, 569–581 (2016)
4. Lee, M., Park, H.S., Park, J.H., Moriyama, K., Kim, M.H.: Two-phase flow friction at high void fraction in porous media with small particles and its impact on dryout heat flux evaluation. Int. J. Multi. Flow **118**, 75–86 (2019). https://doi.org/10.1016/j.ijmultiphaseflow.2019.06.007
5. Lee, M., Park, H.S., Park, J.H., Oh, J.H., Kim, M.H.: Two-phase flow pressure loss through packed particle bed for wide void fraction range. Exper. Thermal Fluid Sci. **108**, 85–94 (2019). https://doi.org/10.1016/j.expthermflusci.2019.06.001
6. Shamsuzzaman, M., et al.: Experimental investigation of debris sedimentation behavior on bed formation characteristics (2012)
7. Goniva, C., Kloss, C., Deen, N.G., Kuipers, J.A., Pirker, S.: Influence of rolling friction on single spout fluidized bed simulation. Particuology **10**, 582–591 (2012)
8. Ma, W., Yuan, Y., Sehgal, B.R.: In-vessel melt retention of pressurized water reactors: historical review and future research needs. Engineering **2**(2016), 103–111 (2016)
9. Hager, A., Kloss, C., Pirker, S., Goniva, C.: Parallel open source CFD-DEM for resolved particle-fluid interaction. In: Proceedings of 9th International Conference on Computational Fluid Dynamics in Minerals and Process Industries, pp. 1–6 (2012)
10. Hager, A., Kloss, C., Pirker, S., Goniva, C.: Parallel resolved open source CFD-DEM: method, validation and application. J. Comput. Multiphase Flows **6**, 13–27 (2014)
11. Kloss, C., Goniva, C., Hager, A., Amberger, S., Pirker, S.: Models, algorithms and validation for opensource DEM and CFD-DEM. Progress Comput. Fluid Dyn. Int. J. **12**, 140–152 (2012)
12. Shamsuzzaman, M., et al.: Numerical study on sedimentation behavior of solid particles as simulant fuel debris. J. Nuclear Sci. Technol. **51**, 681–699 (2014)
13. Ai, J., Chen, J.F., Rotter, J.M., Ooi, J.Y.: Assessment of rolling resistance models in discrete element simulations. Powder Technol. **206**, 269–282 (2011)
14. Shamsuzzaman, M., et al.: Experimental study on debris bed characteristics for the sedimentation behavior of solid particles used as simulant debris. Ann. Nuclear Energy **111**, 474–486 (2018)

Mining Environmental Liability and Its in Situ Treatment with Calcium Oxide for Zinc Removal

A. A. Campos-Llantoy$^{(\boxtimes)}$, J. M. Huanay-Condor, A. A. Muñoz-Navarro, P. C. Espinoza-Tumialán, and N. Tantavilca-Martinez

Universidad Continental, Avenida San Carlos, Huancayo, Junín 12000, Peru
77690148@continental.edu.pe

Abstract. Mining environmental liabilities have negative effects on human health, the ecosystem and property. This study was conducted at the Cercapuquio Mining Environmental Liability (MEL) in the district of Chongos Alto. The wastewater analysis was conducted at Universidad Continental and data were obtained on metal content and hydrogen potential. This investigation revealed that the Cercapuquio MEL wastewater had a higher concentration of zinc, 9,916 mg/L, and the pH level was 7.53 (alkaline), which is why this effluent exceeds the maximum permissible limit of the annual average. A neutralizing reagent was also prepared by recycling eggshells, calcined at 1000 °C for 40 min, obtaining quicklime with 61.30% calcium oxide (CaO). For wastewater treatment, the quicklime obtained in neutralizing solution was used, which, when applied to the effluent, had the effect of lowering the zinc concentration from 9.916 mg/L to 0.051 mg/L and the pH from 7.53 to 10.36. The average zinc removal achieved in the effluent is 96%.

Keywords: Calcium oxide · Eggshell · Environmental liabilities and wastewater

1 Introduction

Peru has a long mining tradition dating back to pre-Inca times. During the XX century, exploration works have been intensified throughout the country, especially in the Andes, which has allowed the opening of new mining deposits. Several of them are still in operation, while the others, for reasons of profitability, have been abandoned [1]. However, at present, Peruvian mining has many challenges to face, such as: guaranteeing the community a sustainable mine closure and avoiding the generation of Mining Environmental Liabilities (MEL), some private companies have taken possession of the MELs to give them an effective solution, because they constitute a problematic outcome for Peruvians [2].

Peru has implemented a law to manage MELs. Law N° 28271 of 2004, establishes criteria that regulates the identification of MELs for their remediation both in the affected areas and in their surroundings, that is, to mitigate their negative impacts on property, ecosystem and human health. MELs are those effluents, emissions, construction debris and waste produced by mining operations, which are currently abandoned or inactive,

are also registered in the inventory of the Ministry of Energy and Mines (MINEM) [3] The main problem for the remediation of MELs is not being able to identify those responsible for the Ex Mining Units (EMU), which is why the State is responsible for their remediation [3]. Soil contamination is a damage caused by the abandonment of a MEL, as these works have generated a clear impact effect, as is the case of the abandonment of mining waste [4]. When abandoned, heavy metals tend to concentrate in plants and organic tissues [5]. The concentrations of heavy metals found constitute an alarm on the ecosystem, due to their possible bioavailability in certain environmental circumstances and at the same time impair water quality [6].

Entrepreneurs in industries with sufficient capital are not interested in installing effective treatment techniques due to weak governmental control and poor enforcement of environmental regulations. The environment can be harmed by heavy metal pollution. They remain for a long time in solution in soil and water and do not decompose like other organic pollutants. Heavy metal contaminants are all soluble at low pH, so toxicity problems are greater in the environment. In the removal of heavy metals from effluents, several types of treatments are used, which are divided into physical, chemical and biological methods. In relation to other procedures, chemical for the treatment of waste from the mining industry, adsorption is the most widely used procedure due to its ease and versatility of design, as well as its performance. The most common adsorbents, such as activated carbon, silica gel, applied aluminum oxide and ion exchange resins, have high performance [7]. This research was carried out with the objective of recycling eggshells to obtain calcium oxide and determine its effectiveness for the neutralization of zinc in wastewater.

2 Methods and Materials

2.1 Study Area

The research study was carried out in the Mining Environmental Liability (MEL) Ex Mining Unit (EMU) Cercapuquio, located in the district of Chongos Alto, province of Chupaca, department of Junin (See Fig. 1); at an altitude of 4327 m.a.s.l. and UTM 454934.074E 8626061.783N. This MEL is registered in the inventory of the Ministry of Energy and Mines (MINEM) 2021 with the following code 010319603; 010347794 [8].

2.2 Sampling Method

A monitoring chain of custody was used, we chose an important point of the tailings dam of the Cercapuquio MEL to determine the study of the metal content and the pH level of the wastewater; we extracted the sample with a sterilized 1000 ml container and then added 20 drops of nitric acid to capture the metals. The analysis study was carried out in a private laboratory. In Table 1 we specify the test methodology used by the laboratory to determine the metal content and pH.
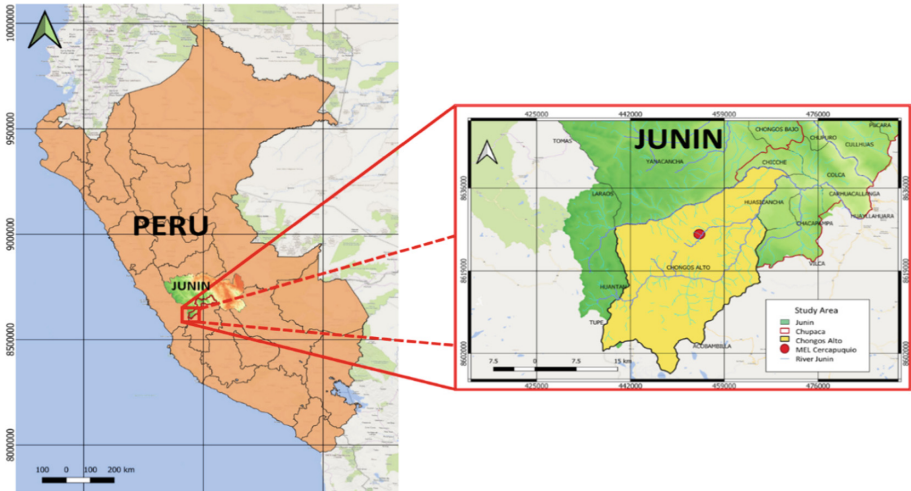
Fig. 1. Geographic location of the Cercapuquio MEL.

Table 1. Standards applied in the analysis of heavy metals and pH.

Assay	Reference method	Description
Arsenic	SMEWW-APHA-AWWA-WEF Part 3500-As B, 23nd Ed.2017	As, Atomic Absorption Spectrometric Method
Copper	SMEWW-APHA-AWWA-WEF Part 3500-Cu B, 23nd Ed.2017	Cu, Atomic Absorption Spectrometric Method
Zinc	SMEWW-APHA-AWWA-WEF Part 3500-Zn B, 23nd Ed.2017	Zn, Atomic Absorption Spectrometric Method
Iron	SMEWW-APHA-AWWA-WEF Part 3500-Fe B, 23nd Ed.2017	Fe, Atomic Absorption Spectrometric Method
Lead	SMEWW-APHA-AWWA-WEF Part 5210-Pb B, 23nd Ed.2017	Pb, Atomic Absorption Spectrometric Method
pH	SMEWW-APHA-AWWA-WEF Part 4500 - H+ B, 23nd Ed.2017	pH Value. Electrometric Method

The results obtained from the laboratory show in Table 2 that the wastewater from the Cercapuquio MEL has a higher presence of zinc, 9.916 mg/L and low iron content, 0.218 mg/L, and the pH level is 7.53, which indicates alkalinity. With the sampling method used, no other heavy metals were detected.

Table 2. Results of heavy metals and pH.

Assay	Result	Unit
Arsenic	<0.001	mg/L
Copper	<0.001	mg/L
Zinc	9.916	mg/L
Iron	0.218	mg/L
Lead	<0.001	mg/L
pH	7.53	pH unit

2.3   Maximum Allowable Limit

In Table 3 specifies the parameters of the Maximum Permissible Limit (MPL) that effluents from mining activities must have, the concentration of chemical elements at the annual average is 1.2 mg/L of zinc and 1.6 mg/L of iron. If the effluent exceeds the heavy metal concentration limits, it can be harmful to human health and the environment. According to the regulations of Supreme Decree N. 010–2010-MINAM, the established parameters must be met [9].

Table 3. Maximum allowable limit.

Parameters	Unit of measurement	Annual average
Zinc	mg/L	1.2
Potential Hydrogen (pH)	pH unit	6.0 to 9.0

3   Laboratory Analysis

3.1   Preparation of Quicklime

For the in situ treatment of the PAM Cercapuquio effluent, we required a reagent that could trap or remove zinc; we decided to prepare calcium oxide (CaO) also known commercially as quicklime (CaO). We chose to obtain quicklime by calcining eggshells. Eggshells are mainly composed of calcium carbonate (CaCO3), which, when calcined, transforms its chemical composition and becomes CaO. In Table 4 describes the procedure we performed in the Continental University laboratory.

Table 4. Preparation of quicklime.

Standards	Process	Formula
Specific Research Method	We recycled 300 g of eggshell, proceeded to clean it by removing as much testicular membrane as possible and left it to dry for 8 h. In the laboratory of the Continental University, we used equipment and materials to carry out the calcination process. In a mortar we started grinding the eggshell and then we poured it into two 125g crucibles, the obtained weight of the eggshell was 220 g	$CaCO_3$
Law of Conservation of Mass	We introduced the two crucibles in the muffle at room temperature, we waited for it to reach 1000 °C and let 40 min elapse, we turned off the muffle and let it cool at room temperature, after 4 h the muffle had a temperature of 300 °C, we removed the two crucibles and put it in the Schreiber desiccator to accelerate the cooling. Finally we sprayed it with the mortar and filled it in a zipper bag eliminating as much air as possible to avoid humidity. The product was weighed on an analytical balance and 116g of quicklime were obtained	$CaCO_3 + \Delta = CaO + CO2$

The purity of quicklime was sent to a private laboratory for analysis; the result obtained is 61.3% calcium oxide and the remaining is inert material. That is to say that in 116 gr. of quicklime, the CaO purity is 71.1 g.

3.2 Calcium Oxide Effect

In Table 5 describes the application of calcium oxide in the wastewater of the Cercapuquio MEL, it is expected that the calcium oxide reagent can remove zinc.

4 Statistical Analysis

The wastewater samples were collected at the Cercapuquio MEL, this study focused on the removal of zinc from different tests with quicklime; statistical results were obtained synthesized by bar and scatter plots, Ms Excel software was used. They were also tested by analysis of variance (ANOVA) by the F value, the critical value of F and a confidence level of 95%.

Table 5. Application of calcium oxide in wastewater.

Standards	Process	Formula
Specific Research Method	We performed the experiment in 4 containers by pouring 1L, 3L, 5L and 10L of waste water into each container. For the reagent, we dissolve 15 g of calcium oxide in 100 ml of drinking water. With a syringe we extracted 1 ml of the reagent and applied it in 1 L of wastewater, after 15 min. we observed that the zinc was sedimenting, but the water still had low turbidity. Then we filtered with qualitative filter paper in one bottle. For the other bottles, 1 ml of reagent was applied for each 1 L, that is, for 3 L we applied 3 ml of the reagent and so on for 5 L and 10 L of wastewater	Removal % $= \frac{Ci-Cf}{Ci} * 100$ Where: Ci: Initial concentration Cf: Final concentration
D. S. N° 010–2010-MINAM	After the procedure, we measured the pH of each container with a potentiometer, giving alkaline results	pH $= -\log [H+]$

5   Results

Table 6 shows 4 tests that we performed with CaO, the dose of 0.613 g of CaO per 1 L of wastewater was applied, the initial zinc concentrate is 9.916 mg/L, in the 1 L test, zinc decreased to 0.051 mg/L, 3 L test decreased to 0.375 mg/L, 5 L test decreased to 0.425 mg/L and in the 10 L test it decreased to 0.742 mg/L. CaO proved to be efficient in the reduction of zinc concentrate with an average efficiency of 96%.

Table 6. Results of zinc removal.

Assays (L)	Initial zinc content (mg/L)	g. of CaO/L of wastewater	Final zinc content (mg/L)	Efficiency (%)	pH initial	pH final
1	9.916	0.613	0.051	99.49	7.53	10.36
3		1.839	0.375	96.22		9.84
5		3.065	0.425	95.71		9.23
10		6.130	0.742	92.52		8.82

The results of the tests in 1 L, 3 L, 5 L and 10 L, the zinc content is reduced to less than 1.2 mg/L allowed and it is observed that the zinc has decreased when CaO is applied to an average of 0.4 mg/L. (See Fig. 2).
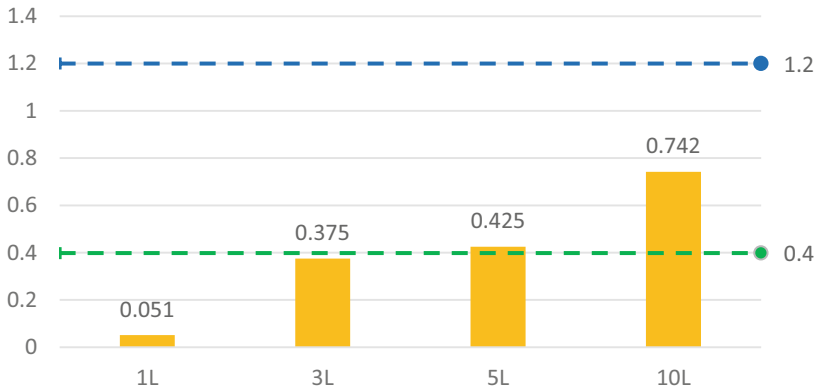
Fig. 2. The final zinc content complies with the maximum permitted limit.

The alkalinity increases slightly when the volume of wastewater is lower, as can be seen in the difference between the 1 L and 10 L tests. The average hydrogen potential of the tests is 9.56 pH, being remarkable the difference with the initial pH 7.53. (See Fig. 3).
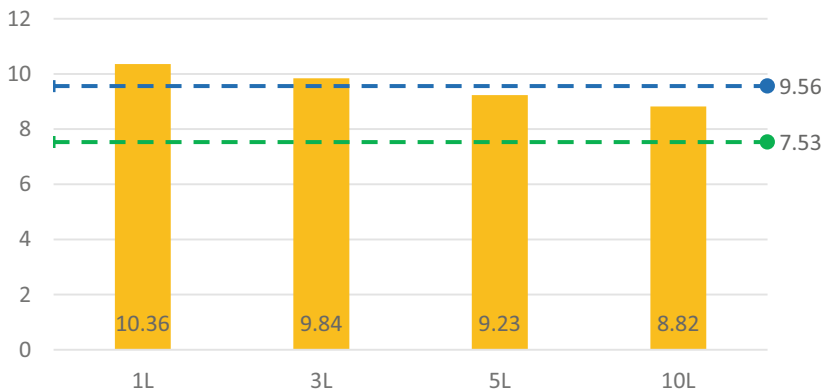
Fig. 3. Hydrogen potential of the assays.

The determined dose decreases its zinc removal efficiency each time the volume of wastewater increases. The effect of pH on zinc removal efficiency, i.e., the highest removal efficiency is 99.49% in the 1 L wastewater test and the pH increases its alkalinity from 7.53 to 10.36, while the removal efficiency in the 10 L wastewater test is 92.52% and the pH increases its alkalinity from 7.53 to 8.82. (See Fig. 4).

5.1 Analysis of Variance

The statistical analysis in Table 7 shows that the total sum of squares is 41.2757558, a degree of freedom of 15 observations was determined. For the row (wastewater) F is
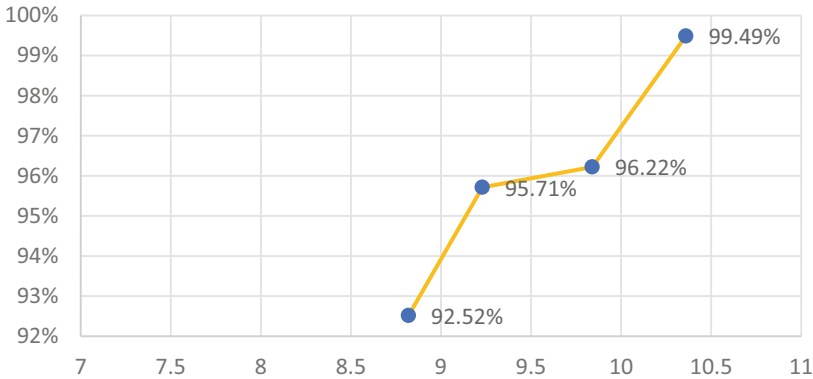
Fig. 4. Effect of pH on zinc removal efficiency.

greater than the critical value, meaning that the H0 that there is a difference between the amounts of wastewater is rejected, and for the column (CaO dose) F is less than the critical value, meaning that the H0 that there is no difference between the CaO doses is accepted.

Table 7. Analysis of variance of two wastewater factors.

Origin of variations	Sum of squares	Degrees of freedom	Mean of squares	F	Probability	Critical value for F
Files	18.2733013	3	6.09110042	4.68315981	0.030968955	3.862548358
Columns	11.2967033	3	3.76556775	2.89516743	0.094356241	3.862548358
Error	11.7057513	9	1.30063903			
Total	41.2757558	15				

H_{oFA}: $\mu R1 = \mu R2 = \mu R3 = \mu R4$
H_{iFA}: At least one of the wastewater quantities is different.

6   Discussion of the Results

Water contamination by metal ions causes different effects on the environment and human health. Therefore, eggshell adsorption is proposed as a simple and low-cost procedure to remove these pollutants from wastewater [10]. Eggshell as waste was efficiently used as a neutralizer for effluent treatment. Eggshell powder efficiently removed heavy metal ions from wastewater and its removal efficiency reached 99% [11]. According to the results of zinc adsorption, it is shown that the metallic content reduced in the 4 wastewater tests, after applying CaO or quicklime, this means that it reduced 96% = 0.396 mg/L of the metallic content when CaO was applied. Since it complies with the

maximum permissible limit of zinc 1.2 mg/L [9]. The MEL wastewater has an alkaline pH of 7.53, and it is also affected when CaO is applied to it, this is observed in Fig. 3 the pH variation in the 1 L, 3 L, 5 L and 10 L tests and the average pH tends to reach 9.56.

7   Conclusion

With the results presented in this research, it was demonstrated that calcium carbonate calcination is an efficient and sustainable method to reduce the concentration of zinc in an effluent. Eggshell was used, applying a calcination process to obtain calcium oxide. The calcium oxide was used for a zinc removal treatment, a dose of 0.613 mg/L was applied to reduce the zinc concentration in the effluent. The results obtained were very positive as zinc was removed with an average efficiency of 96%. By analyzing these results, we conclude that eggshell is an effective element to apply to effluents with high zinc concentration.

References

1. Chappuis, M.: Remediación y activación de pasivos ambientales mineros (PAM) en el Perú (2019)
2. Rodríguez, C., Julca, D.: Gestión del cierre de minas Estudio técnico-legal sobre el alcance de la legislación peruana (2020)
3. Catillo, L., Satalaya, C., Paredes, Ú., Encalada, M., Zamora, J., Cuadros, M.: Pasivos ambientales mineros en el Perú: Resultados de la auditoría de desempeño sobre gobernanza para el manejo integral de los PAM. Documento de Política en Control Gubernamental. Contraloría General de la República (2021)
4. Somgohano, R.E.: Evaluación de la fitotoxicidad en suelos contaminados por metales pesados en pasivos ambientales minero-metalúrgicos (2013)
5. Gobierno de la Rioja: Salud y metales pesados - Medio ambiente - Portal del Gobierno de La Rioja. https://www.larioja.org/medio-ambiente/es/calidad-aire-cambio-climatico/calidad-aire/red-biomonitarizacion-metales-pesados-rioja/salud-metales-pesados
6. Aguirre, S.E., Piraneque, N.V., Linero-Cueto, J.: Heavy metals concentration and physical-chemical water quality of the Ciénaga Grande de Santa Marta. Rev. U.D.C.A Actual. Divulg. Cient. **24** (2021). https://doi.org/10.31910/rudca.v24.n1.2021.1313
7. Stadelman, William J.; Cotterill, O.J.: Eggs and egg products. Wiley, New York, NY, USA (2000)
8. Ministerio de Energía y Minas - R.M. Nº 200-2021-MINEM/DM – Minería. http://www.minem.gob.pe/_legislacionM.php?idSector=1&idLegislacion=13423
9. Ministerio del Ambiente: Decreto Supremo N° 010-2010-MINAM | Ministerio del Ambiente. https://www.minam.gob.pe/disposiciones/decreto-supremo-n-010-2010-minam/
10. Zonato, R. de O., Estevam, B.R., Perez, I.D., Aparecida dos Santos Ribeiro, V., Boina, R.F.: Eggshell as an adsorbent for removing dyes and metallic ions in aqueous solutions. Clean. Chem. Eng. **2**, 100023 (2022). https://doi.org/10.1016/J.CLCE.2022.100023
11. Hassan, E.S.R.E., Rostom, M., Farghaly, F.E., Abdel Khalek, M.A.: Bio-sorption for tannery effluent treatment using eggshell wastes; kinetics, isotherm and thermodynamic study. Egypt. J. Pet. **29**, 273–278 (2020). https://doi.org/10.1016/j.ejpe.2020.10.002

Ecological Environment Protection and Sustainable Development

The Dalcahue Fire Risk Prevention Plan as a Restorer of the Landscape and Degradation

Vicente Valdebenito[1], Stefania Pareti[2(✉)], Loreto Rudolph[1], and David Flores[3]

[1] Federico Santa María Technical University, Valparaiso, Chile
{vicente.valdebenito,loreto.rudolph}@sansano.usm.cl
[2] Andres Bello University, Santiago, Chile
s.pareti@uandresbello.edu
[3] Pontifical University, Santiago, Chile
daflores2@uc.cl

Abstract. The present research aims to explore how the implementation of a risk prevention plan for the commune of Dalcahue can facilitate habitat reconstruction, landscape degradation and restoration.

The commune of Dalcahue is selected as a case study because (1) it contextualizes Dalcahue as one of the most fire-prone communes in the region (country) due to interests related to agricultural activities (2) most of the buildings in this area are made of wood, a highly flammable material, (3) among these buildings are churches declared World Heritage by UNESCO (4) the commune is located within the ecoregion of Chiloé, protected by its native fauna and vegetation. (5) Dalcahue does not have a forest fire prevention plan in place at the communal level.

The methodology is carried out through the analysis of the regional prevention plan of Los Lagos and the work of title Plan of Territorial Protection against Forest Fires for the commune of Dalcahue, together with secondary sources, followed by an analysis of 15 headlines of the year 2021, because it was a peak period of fires in the area.

It is concluded that the prompt implementation of an institutional fire prevention plan for the commune of Dalcahue is necessary, since it facilitates habitat reconstruction, landscape degradation and restoration, as has occurred in the safeguarding of the commune of Dalcahue in Chiloé.

Keywords: Landscape degradation and restoration after fire · Habitat reconstruction after fire · Fire prevention plan

1 Introduction

The objective of the research is to explore how the implementation of a risk prevention plan for the commune of Dalcahue can facilitate habitat reconstruction, landscape degradation and restoration.

Chiloé (Fig. 1) is an archipelago located in southern Chile. The island of Chiloé is the largest of all the islands. The Valdivian Forest is the flora originally found on the island, it is a green forest with a great diversity of plant species, both large trees and ferns or mosses [1]. With the arrival of the farming people, burning began to be common with the aim of clearing land for agriculture and later for livestock, so that many forests became farmland and meadows, while several of these lands were abandoned and currently being used in an uncontrolled manner a species of shrub introduced, the espinillo.

Due to the wide variety of forests, the use of wood for the construction of houses and churches is quite typical of the area and has become a heritage asset over the decades. Centennial churches and vernacular constructions are fundamental to generate this heritage that is valued both nationally and internationally.

Fig. 1. Map of Chiloé, commune of Dalcahue, Chile.

2   Theoretical Framework

The theoretical framework of this study focuses on landscape degradation and restoration after fire (1), habitat reconstruction after fire (2), fire prevention plan (3).

Deforestation, desertification, loss of biodiversity, loss of productive potential, soil erosion, among other impacts associated with landscape degradation, are the result of

human activity. It is necessary to understand the preservation of the natural system to address the environmental problem, which requires avoiding or reducing degradation and restoring degraded ecosystems.

Land and ecosystem degradation neutrality aims to maintain or improve the resource condition, while forest landscape restoration aims to reduce soil loss and improve soil quality and health by maintaining and increasing organic matter [2]. Land degradation is considered as any alteration of land that is detrimental excluding natural disasters, however, human activities can directly affect phenomena such as forest fires [3].

Restoration of burned areas in post-fire zones consists of helping in the recovery of land degraded, damaged, or destroyed by fire. The return of the structure, composition, species diversity and functioning closer to the initial state, are considerations for the restoration of an ecosystem, a difficult application that is becoming more and more relevant [4], having as focus to counteract the water imbalance, or the hydrological restoration and the population impact that comes with it, generated after a fire catastrophe.

Forest fires represent a significant cause of loss of national heritage, this is related to the fact that during the last decades the State has led several administrations that managed to consolidate the Chilean economy at international level, translated into exports based on natural resources, becoming the main economic engine of Chile. The growth of exports has strong demands on natural resources, impacting the environment, losing thousands of hectares of natural habitats that are difficult to recover [5]. The Chilean economic model is likely to remain based on the export of products, so the implementation of environmental policies focused on the sustainable use of resources and the recovery of ecosystems is important to ensure development.

Ecological restoration [6] is an activity that initiates or accelerates the recovery of an ecosystem, helps to restore what has been damaged or destroyed, both for integrity and sustainability. Although it may seem contradictory, forest fires restore and improve the forest ecosystem, promoting and enriching the native biodiversity of the affected areas, creating habitats with optimal conditions for wildlife in the forest [4]. Ecological restoration is a concept and also a process, which requires necessary stages after the disturbance by fire, these can be carried out in a linear or synchronous way and are mainly synthesized in: collection of information of the affected plant groupings; Definition of the ecosystem towards which it is intended to redirect; Inventory of the burned area - Analysis of the collected information; Plan, program or restoration project; Execution of the actions.

A fire management program considers four basic aspects: Prevention, Budgeting, Fire Fighting and Fire Use. Prevention. These are measures that prevent the occurrence or spread of forest fires. It controls risk and danger; risk is the agent that originates or causes a fire, and danger is the degree of conflict that a fire can reach once it has spread. It will depend on topographic, vegetational and atmospheric conditions. Budgeting. It is planned and programmed prior to the occurrence of the fire, to evaluate the problems that may arise. Fighting. It is the activity that controls the forest fire, aimed at extinguishing the fire. This is carried out to break the fire triangle [7].

The commune of Dalcahue, according to Köppen's classification, the commune is under the influence of two types of climates. The first corresponds to the warm temperate rainy climate without dry season (Cfb), which is present towards the west of

the commune, and the second corresponds to the warm temperate rainy climate with Mediterranean influence (Cfsb), present towards the eastern sector of the communal territory. The high rainfall means that the commune has a large percentage of use destined to native forest, covering 43% of the total area. These characteristics added to an irregular geomorphic terrain, shaped by the rocky coastal mountain range and the dismemberment of the Central Valley due to the sea entering the island, [8] generate an inaccessible terrain when fighting fires that, together with the lush vegetation, give way to fires that spread rapidly and are difficult to extinguish with conventional equipment.

Dalcahue is characterized for being a city built with local materials, mainly wood, which comes directly from the trunk and is not subjected to fireproofing treatments, which makes it combustible when subjected to temperatures above 120 °C [9] and starts a chemical deterioration, turning it into charcoal and releasing flammable gases. The church of San Francisco de Ancud, is one of the famous wooden temples of Chiloé that is part of the group of unique wooden churches declared World Heritage Site by UNESCO in 2000, on January 20, 2020 suffered an incendiary catastrophe that caused the structure to yield in its entirety, The day after the fire, the Ministry of Cultures, Arts and Heritage announced plans to rebuild it [10], however, two years after the fire there is still no funding for the design or reconstruction of the church [11].

3   Methodology

The study was carried out based on the analysis of the Regional Forest Fire Prevention Plan, focusing the study on the city of Dalcahue. This is complemented with the analysis of secondary sources to support the results obtained from the plan.

Finally, a study is made of the headlines of 15 press releases published during the year 2021, understanding that during its course many fires occurred. The following filters were used for the search: Fires - Dalcahue - 2021. This last exercise will allow understanding the current situation with respect to the tragedies that have occurred, how the response to these tragedies has been and what is the role of the mentioned plan within these dynamics, which was also consolidated with the construction of a word cloud that concentrates the most repetitive concepts with respect to the search carried out.

4   Results

A forest fire protection plan corresponds to the organization whose objective is to minimize the occurrence and damage of forest fires. It describes the problems related to the occurrence, spread and damage of fires, the means, and the necessary disposition to solve them, as well as the amount, quality and distribution of the resources that must be available to achieve the proposed objectives [12].

A first superficial analysis of the Regional Forest Fire Prevention Plan indicates that forest fires in Dalcahue are concentrated in rural lands adjacent to roads and near the border with the commune of Castro, establishing this area as a priority for supervision and prevention strategies [13].

The cadaster offered by the Plan identifies as the main underlying factor of the forest fires suffered the use of fire associated with silvoagricultural work, both the authorized burning of plant material and those carried out illegally without warning [13].

In the same line, as the priority of these zones is understood, there is a coordination for the prevention and supervision of these, where the main actors are the SAG (Servicio Agrícola Ganadero), the CONAF (Corporación Nacional Forestal), the INDAP (Instituto de Desarrollo Agropecuario) and the Carabineros. This coordination involves the development of preventive activities ranging from the control of the aforementioned risk activities, the dissemination of preventive messages in risk areas, and the posting of informative signs regarding the legal consequences of illegal burning and the setting of forest fires. Regarding the first point, it should be understood that these tasks work with a regulation, proposing months where the activity is allowed with the proper prior permits, where notice must be given to CONAF, to establish a date and time indicated where the burning can be carried out; this will depend mainly on the meteorological conditions that exist and the occurrence of fires during the previous dates [13].

To contextualize, in the last forest fire seasons, the commune was affected by 11 fires, which translates into 8 hectares burned as an average area, both figures are averages. This places it as one of the 4 communes of the Lakes Region that exceed the average of 10 fires, being surpassed by Castro, with an average of 12, Puerto Varas, with 12 fires and Puerto Montt, which totally escapes the figures with an average of 80 fires. It should be noted that there is no direct or indirect relationship between the number of fires and the number of hectares affected [13].

The latter transforms the commune of Dalcahue into a priority sector for fire surveillance during the high fire season, but paradoxically, at the time of the cadaster, it does not have a strategic axis of community environmental education for fire prevention within the commune, although it is important to note that this was in the process of development [13].

A large part of Dalcahue's land area (Fig. 2) has native forests, so part of the commune is within the Chiloé ecoregion represented by the persistent coastal rainforest, which is composed of evergreen forests that extend along the Coastal Mountain Range with dense, lush vegetation rich in epiphytes, lianas, ferns and large grasses. Species such as the Chiloé oak or coigüe (Nothofagus nítida) can be found. There is also endemic fauna, such as the Pudú Pudú (Pudú Pudú), the Huillín Cat (Lutra provocax) and the Chilote Fox (Canis fulvipes) among others [14].

Along with the ecological importance of the commune, there is also a heritage value. The Church of Nuestra Señora de los Dolores de Dalcahue (Figs. 3 and 4) is a Catholic church located in Dalcahue's Plaza de Armas. It is one of the largest and oldest churches in Chiloé, because although the construction of its current temple was begun in 1893 and completed in 1902, there is evidence that it may date back to 1858. [15] It is one of the exponents of the local architectural style, the Chiloé School of Wooden Architecture, and was declared a Historic Monument by Supreme Decree No. 1750 of July 26, 1971, and a World Heritage Site by UNESCO on November 30, 2000. [Ibid] Considering the fate of other heritage churches, such as the San Francisco de Ancud church, it is important to have a prevention plan to protect this church, built entirely of wood, as well as most of the buildings in the area.
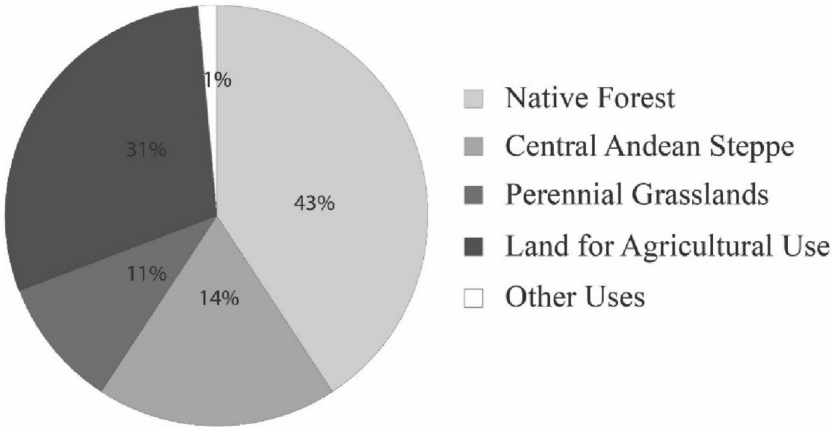
Fig. 2. Land use in Dalcahue commune. Data source from [8]

Fig. 3. Dalcahue's Church Façade. Council of National Monuments of Chile.

Fig. 4. Interior of the Dalcahue Church. Council of National Monuments of Chile

From the word cloud (Fig. 3) it can be observed that the most representative words apart from those found in the filters, are focused on houses, destruction, and Castro. This last word refers to the central city of Chiloé, which although it has also had one more forest fire than Dalcahue between 2020 and 2021 (33 and 32 respectively), the affected area of the former has been 66.75 hectares, while Dalcahue has seen 82.76 hectares of its land affected, a considerable damage as to be overshadowed by Castro in the media. Along with this secondaryization of Dalcahue, it is worth mentioning the lack of news or initiatives on the part of the commune's management for the elaboration of preventive plans. Although the municipality has a detailed emergency plan, it does not have a prevention mechanism that takes precedence over the fire situation. The only prevention plan created for Dalcahue is theoretical and comes from a degree project of the Austral University, an institution close to the island of Chiloé. As seen in the theoretical framework, [8] the case of the Dalcahue emergency plan promulgated by the municipality fulfills the objectives of presuppression, firefighting and fire use, but not prevention.

From the word cloud (Fig. 5 and Table 1) the most representative words, apart from those found in the filters, are focused on houses, destruction, and Castro. This last word refers to the central city of Chiloé, which, although it has also had one more forest fire than Dalcahue between 2020 and 2021 (33 and 32 respectively), the affected area of the former has been 66.75 hect., while Dalcahue has seen 82.76 hect. of its land affected, [considerable damage to be overshadowed by Castro in the media. Along with this secondaryization of Dalcahue, it is worth mentioning the lack of news or initiatives on the part of the direction of the commune of the elaboration of preventive plans. Although the municipality has a detailed emergency plan, it does not have a prevention mechanism that takes precedence over the fire situation. The only prevention plan created for Dalcahue is theoretical and comes from a degree project at Universidad Austral, an institution close to the island of Chiloé. As seen in the theoretical framework, [8] the case of the Dalcahue emergency plan promulgated by the municipality meets the objectives of pre-suppression, combat, and use of fire, but not prevention.

Fig. 5. Word cloud from media headlines.

Table 1. Word cloud and sources.

Example headline	Source
Nearly 140 houses were burned after a raging forest fire in Castro	https://www.cnnchile.com/pais/incendio-castr-chiloe-140-casas-quemadas-20211210/
Authorities insist on calls to prevent forest fires in Chiloé	http://www.gobernacionchiloe.gov.cl/autoridades-insisten-en-llamado-a-prevenir-incendios-forestales-en-chiloe/
Red alert decreed in Castro due to forest fire: more than 20 houses affected	https://www.elmostrador.cl/dia/2021/12/09/decretan-alerta-roja-en-castro-por-incendio-forestal-mas-de-20-casas-afectadas/
Red alert for forest fire in Dalcahue	https://www.diariochiloe.cl/noticia/actualidad/2021/03/alerta-roja-por-incendio-forestal-en-dalcahue
Regional Authorities visit Process Plant in Dalcahue affected by fire	https://www.mintrab.gob.cl/pgm/CanalRegional/LosLagos/autoridades-regionales-visitaron-planta-de-procesos-en-dalcahue-afectada-por-incendio/

5 Conclusions

To conclude this research, we can conclude that the commune of Dalcahue is a valuable area for ecological diversity and native flora and fauna for the island of Chiloé, especially for the native forest area. It is of fundamental importance to create a plan focused on the prevention of fires, as well as to create measures to alleviate the losses generated by past fires and to face in situ those that will occur. It is important to highlight in the creation of these communal plans the efforts made by academia through universities, which, as could be seen in the case of the degree work "Plan de Protección Territorial contra Incendios Forestales para la comuna de Dalcahue, Provincia de Chiloé, Región de Los Lagos" can compile information and proposing strategies based on plans that worked years ago. Another example of contribution to habitat reconstruction is the ecological restoration file for native ecosystems affected by forest fires, carried out by the Faculty of Agronomy and Forestry Engineering of the Catholic University of Chile together with the National Forestry Corporation of the Chilean government, whose mission is to contribute to the development of the country through the conservation of the wild heritage and the sustainable use of forest ecosystems for the integral service of the citizens, protecting wild areas of the state and private individuals against forest fires.

From the analysis of the word cloud, it is possible to identify a lack of dissemination about the problem of the commune of Dalcahue, finding few headlines about the problem related to forest fires in the commune of study, being overshadowed by the commune of Castro. It is essential to develop a prevention plan for the commune of Dalcahue, to protect the fauna and buildings prone to fires.

References

1. Fundación amigos Iglesias de Chiloé. http://www.obispadodeancud.cl/fundacion-amigos-iglesias-de-chiloe/
2. Stanturf, J.A.: Landscape degradation and restoration, pp. 125–159 (2021)
3. United States Department of Agriculture Human Induced Land Degradation is Preventable Through Understanding and Remediation of the Underlying Causes
4. Fernández, I., Morales, N., Olivares, L., Salvatierra, J., Gómez, M., Montenegro, G.: Restauración ecológica para ecosistemas nativos afectados por incendios forestales (2010)
5. CONAMA: Una Política Ambiental para el Desarrollo Sustentable, 47 pp (1998). http://www.sinia.cl/1292/articles-26000_pdf_politica.pdf (Last visit: January 2022)
6. Clarke, M.F., et al.: Fire and its interactions with other drivers shape a distinctive, Semi-Arid 'Mallee' ecosystem. Front. Ecol. Evol. (2021). https://doi.org/10.3389/fevo.2021.647557
7. Julio, G., Bosnich, J.: Fundamentos del Manejo de Fuego, p. 285. Universidad Austral de Chile. Facultad de Ciencias Forestales. Valdivia, Chile (2005)
8. Ministerio de Agricultura: CIREN 2020 Comuna de Dalcahue, Recursos Naturales. https://www.sitrural.cl/wp-content/uploads/2020/06/Dalcahue_rec_nat.pdf
9. Alberto Mozó, Madera y Fuego. S.f
10. Radio Cooperativa (Santiago) 2020. El Ministerio de las Culturas planea reconstruir "cuanto antes" la Iglesia San Francisco de Ancud Consultado el 08–01–2022
11. Insular 2021 Reconstrucción de Iglesia San Francisco de Ancud se mantiene sin financiamiento. Consultado el 08–01–2022. https://elinsular.cl/noticias/chiloe/2021/09/30/reconstruccion-de-iglesia-san-francisco-de-ancud-se-mantiene-sin-financiamiento/
12. Julio, G.: Método de Determinación de Prioridades de Protección. Universidad de Chile. Escuela de Ciencias Forestales. Manual Docente Nª 10. Santiago. 28 p (1992)
13. CONAF: Plan Regional de Prevención Contra Incendios Forestales. Región de los Lagos (2019)
14. Quintana, C.: Plan de Protección Territorial contra Incendios Forestales para la comuna de Dalcahue, Provincia de Chiloé, Región de Los Lagos (2015). http://cybertesis.uach.cl/tesis/uach/2015/fifq.7p/doc/fifq.7p.pdf
15. Consejo de Monumentos Nacionales. N.D. IGLESIA DE DALCAHUE

The Vulnerability of the Environmental Resources of the Arganeraie Biosphere Reserve - Souss Massa and Its Resilience for Sustainable Development

Hala Idrassen[✉], Said Boujrouf, and Noureddine Ait Mensour

Laboratory of Studies on Resources, Mobility and Attractiveness (LERMA), Faculty of Letters and Human Sciences, Cadi Ayyad University, Marrakesh, Morocco
`hala.idrassen@ced.uca.ma`

Abstract. The Arganeraie Biosphere Reserve (ABR) is an ecosystem whose goal is to reconcile the conservation of natural resources and sustainable socioeconomic development. However, the tendencies of overexploitation of natural resources, the continuous degradation of ecosystems are facts from which the ABR suffers and which threaten its cultural, heritage and natural wealth at different territorial levels. This work aims to produce a vulnerability model adapted to the ABR of Souss-Massa, which constitutes 74% of the total surface of the ABR, through the State-Pressure-Result (SPR) method developed by the Organization for Economic Cooperation and Development (OECD). This method will be applied to the water, soil and biodiversity sectors. This article exposes, in the first place, the state of these three predicted sectors. Secondly, it studies the pressure exerted on these said sectors to frame the vulnerability of the study area. Finally, the article highlights the different measures undertaken by stakeholders to mitigate the pressure on the previous sectors. However, an acceptable level of resilience hasn't been achieved and this paper will discuss the reason why.

Keywords: ABR-SM · Vulnerability · Environmental resources · Resilience · Sustainable development

1 Introduction

Morocco, as part of the implementation of the 1992 Rio Declaration, has embarked on a long participatory process to promote the planning and sustainable management of natural resources. In this perspective, the Arganeraie was recognized in 1998 by UNESCO as the first Moroccan Biosphere Reserve to promote the uniqueness of the ecosystems and the biodiversity of the argan tree.

The development of specific risk profiles (pressures on water, soil, biodiversity) in the ABR (Arganeraie Biosphere Reserve) is a crucial and unavoidable point to diagnose its vulnerability and try to improve and maintain its ecosystem services. Systems that contribute to human well-being. Biodiversity loss, overgrazing, increasing urbanization,

disorderly use of forest massifs and rangelands are the consequences of adopting unsustainable human development models and use systems that threaten the socio-ecological balance of the ABR [1]. What then are the major figures responsible for the vulnerability of the environmental resources of the ABR-SM? And what actions are stakeholders taking to preserve the ecological system and achieve an acceptable level of resilience?

To answer the problem, we will adopt the SPR (State-Pressure-Response) model developed by the Organization for Economic Cooperation and Development (OECD). Before explaining the terminology of these three phases, it should be noted that the choice of ecological factors is adapted and depends on the specificity of the ABR. Firstly, the "State" corresponds to the diagnosis of the qualitative and quantitative aspects of the natural resources of the ABR-SM (Arganeraie Biosphere Reserve Souss Massa). Secondly, we tend to propose "Pressure" to describe the main figures of vulnerability of the ABR-SM summarized in the study of pressure on water, soil and forest and biodiversity. Finally, the "Response" phase identifies the interventions and actions to be taken by all stakeholders to address vulnerability and reduce pressure on resources. Our scientific approach is supported by the cartographic analysis, the field work and the documents collected at the level of the regional administrations of Souss-Massa.

The objective of this paper is to develop a vulnerability model of environmental resources specific to the ABR-SM. This model will be a prototype that can be further strengthened by integrating other indicators. First, this article highlights some vulnerability indicators specific to ABR-SM, which is a first experience at this level. Second, it allows us to identify the actions taken by the actors and to understand how the administration deals with these vulnerabilities and maintains level of resilience for a socio-ecological balance.

1.1 Study Area

The ABR is a territory that is not limited only to a geographical entity but is rather based on more or less organized interactions of a group or groups in "common projects". It is located in west-Central Morocco and is part of the transition zone between the Mediterranean and the Sahara, formed around a forest species endemic to Morocco (Argania spinosa), which is the main characteristic of the Macaronesian sector, with a vegetation of forests, woody plants and Mediterranean sclerophyllous [1]. It includes three regions: the Souss Massa region, which represents 74% of the ABR area, while the Marrakech-Safi region occupies 18% and the Guelmim-Oued Noun region the remaining 8%.

It covers an area of 2.5 million ha, organized as follows:

Administratively, the study area includes the Souss-Massa region, which occupies 74% of the total area of the ABR (Fig. 1). The ABR-SM involves three provinces and two prefectures: Taroudant, Chtouka-Aït Baha, Tiznit, Agadir-Ida Ou Tanane and Inezgane-Aït Melloul.

As for forestry, ABR-SM is under the administration of Water and Forests.
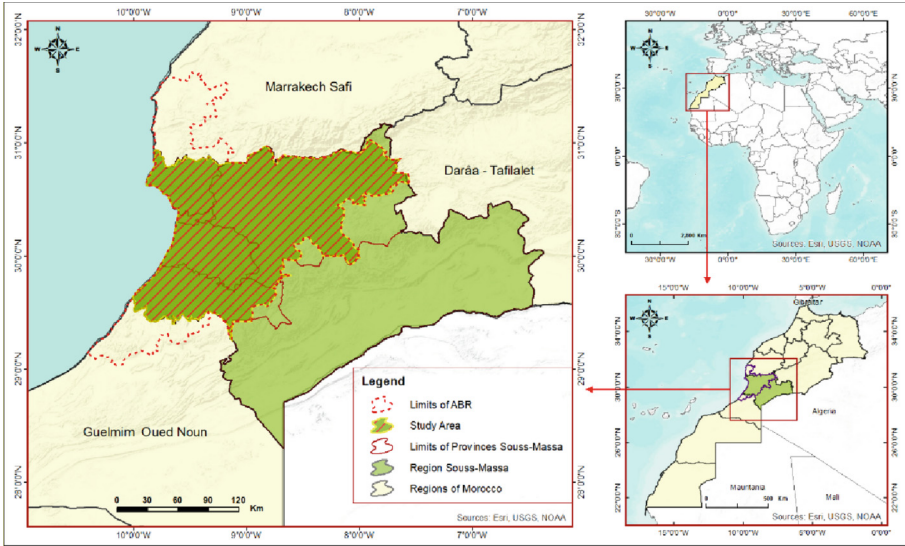
Fig. 1. Location of the study area at ABR level [2]

2 Diagnosis and Condition of Natural Resources in the ABR Souss Massa

This first part concerns the natural resources of ABR-SM namely water, soil and biodiversity.

2.1 Condition of Water Resources: Significant Hydraulic Capital

The ABR-SM offers a variety of hydrological basins with scattered areas drained by a limited number of large wadis, namely [3]: the Souss basin (16,200 Km^2); the Massa basin (6,280 Km^2), the Tamri-Tamghart basin (2,600 Km^2) and the Tiznit plain (2,800 Km^2) [3]. Therefore, it has deep water tables (continuous and discontinuous), namely: sous, chtouka, tiznit and tafraout. In the absence of these aquifers, small aquifers and alluvial aquifers supply the water scarce areas.

Surface Water Resources Condition. The surface water resources are limited and very irregular. Indeed, the flows of the wadis are characterized by a strong interannual irregularity and their runoff is limited to short flood periods. Thus, the average inflow of surface water is 668 million m^3/year. Historically speaking, the minimum and maximum inflows are 35 Mm^3 (1960–61) and 2,160 Mm^3 (1962–63) [3], respectively. In addition, the ABR-SM has a storage capacity of more than one billion m^3 of water, particularly through the two major dams, the Abdelmoumen Dkhila Dam and the Youssef Ibn Tachfine Dam (Fig. 2). Water deliveries during the period from September 1, 2016 to August 31, 2017 from all dams in the Souss Massa (Fig. 2). Water basin amounted to 190 million m^3, distributed as follows: 134 Mm^3 for irrigation, 55 Mm^3 for drinking water supply, and 1.3 Mm^3 for artificial recharge of the water table [5]. The volumes of these
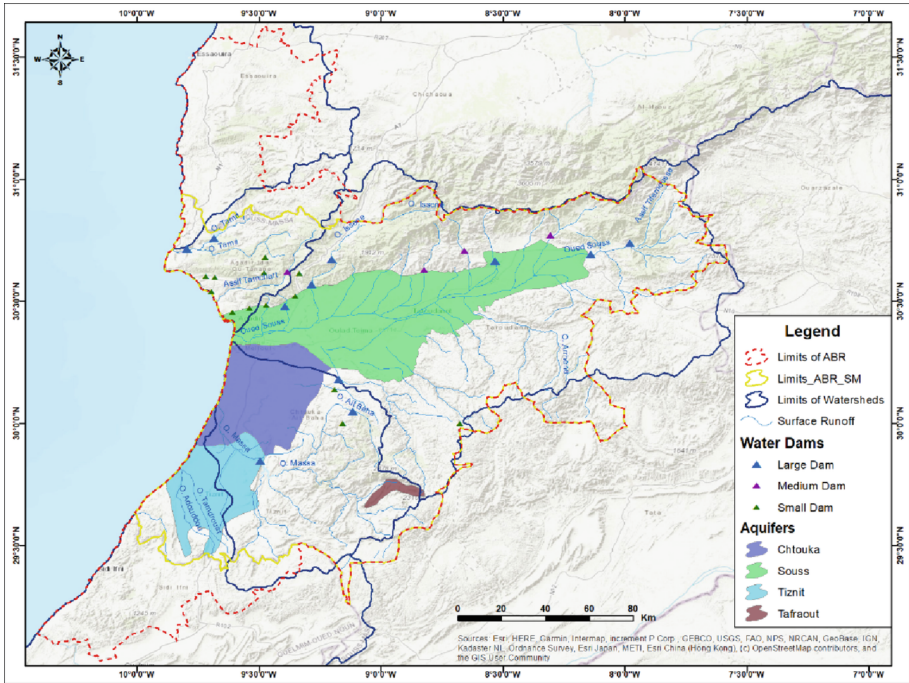
Fig. 2. Authors, groundwater under the ABR-SM, 2022 [4]

supplies vary from one season to another depending on the amount of precipitation, with an average proportion in terms of destination in the order of 70% for agriculture, about 29% for drinking water supply and about 1% for artificial recharge of groundwater [6].

Condition of Groundwater Resources. The ABR-SM has a capital of "renewable" subsurface resources, i.e., exploitable without obvious impact on the sustainability of the aquifers witch a volume of 468 Mm^3/year, distributed as follows [7]:

As for the Chtouka aquifer, the evolution of the water balance shows that this aquifer has been in hydraulic deficit since the 1970s, decreasing from 5 million m^3 in 1972 to -58 million m^3 in 2007. As for the Tiznit aquifer, the available assessments indicate that the sensitivity is relatively low. It has relatively well-preserved reserves, thanks to the recharge of deep aquifers. The aquifer, once in equilibrium (1973), now has a slight deficit, estimated at -1.5 Mm^3 for 2007.

Spatially, the situation is particularly delicate in the High Atlas aquifers. The presence of a significant pluviometric contribution depending on the altitude, combined with the lapiszic nature of the Jurassic strata (limestones, marl limestones), allows a good flow of water in the various springs and recharges mentioned, as well as at the level of the alluvial deposits of the right bank tributaries of the Wadi Souss.

The situation in the mountainous regions (especially in the Anti-Atlas) is more complex. Indeed, the aquifers are less developed and are often limited to localized pockets circulations in fractures. Being poor in reserves (at 129 million m^3/year, they represent 30% of global renewable resources at the basin scale), the limestones and crystalline

inclusions of the Anti-Atlas remain the most problematic in terms of water regeneration and renewal. Their sensitivity to direct recharge from precipitation is increased [7].

As for the Souss Chtouka aquifer simulated two major cones of subsidence, in the center of the plain (from Taroudant Bridge to Biougra via Ouled Teima) and at its hydraulic headwaters (Aoulouz sector). The first cone is mainly the result of intensive exploitation of resources and inappropriate over-extraction [7]. The second one is more a typical hydrogeological character (low thickness of the aquifer, lack of lateral recharge, etc.).

2.2   Condition of the Soil: Wealth with High Agricultural Potential

Soil is a physical environment that performs the biological functions of nourishing plants and supporting human activities. It is also a natural resource that acts as a filter and buffer between the atmosphere and water.
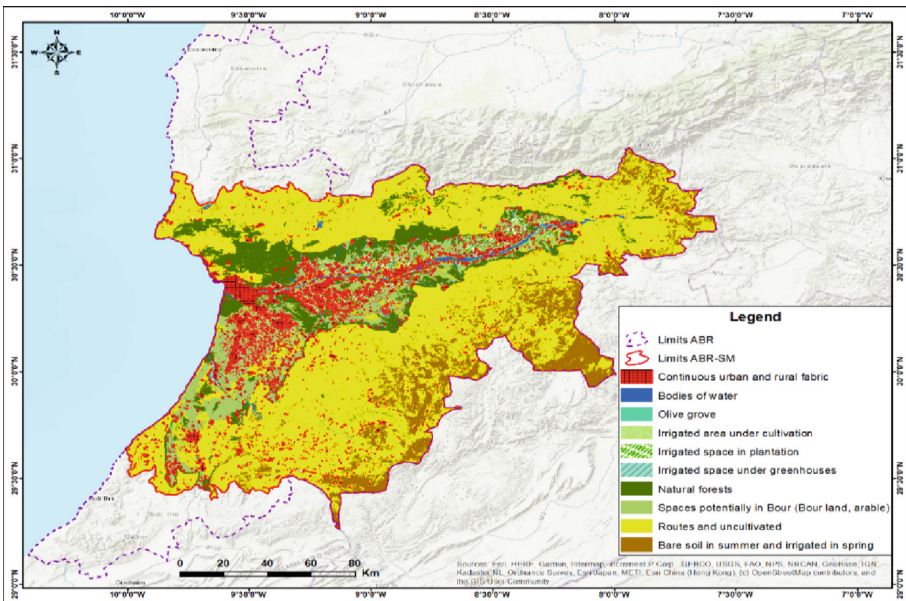
Fig. 3. Authors, types of land use in ABR-SM, 2022 [8]

The ABR-SM is characterized by heterogeneity from a topographic and geomorphological point of view (Fig. 3). In fact, the Souss-Massa valley contains loose soils with the highest agricultural potential.

2.3   The Biodiversity and Endemic Resources of the ABR-SM

The argan tree (Argania spinosa) remains the emblem of ABR-SM, where it practically occupies almost 700,000 ha (Fig. 4). It is a species endemic to the reserve and offers multiple uses (agriculture, livestock). The argan tree has an undeniable socio-economic and cultural importance, but it also plays an important ecological role, being the last green barrier against desertification. It is estimated that the argan tree ecosystem brings in an average of MAD 5.9 billion annually, which is an average contribution to the regional GDP of about 7%. Not to mention the income from hunting, which exceeded MAD 2 million in the 2012–2013 hunting season [1].
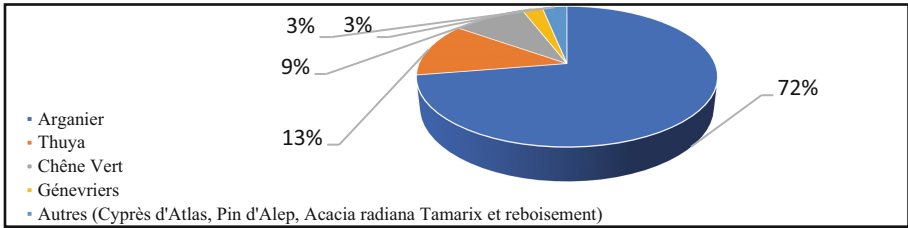
Fig. 4.   Proportion of vegetation type in area at the ABR-SM level [9]
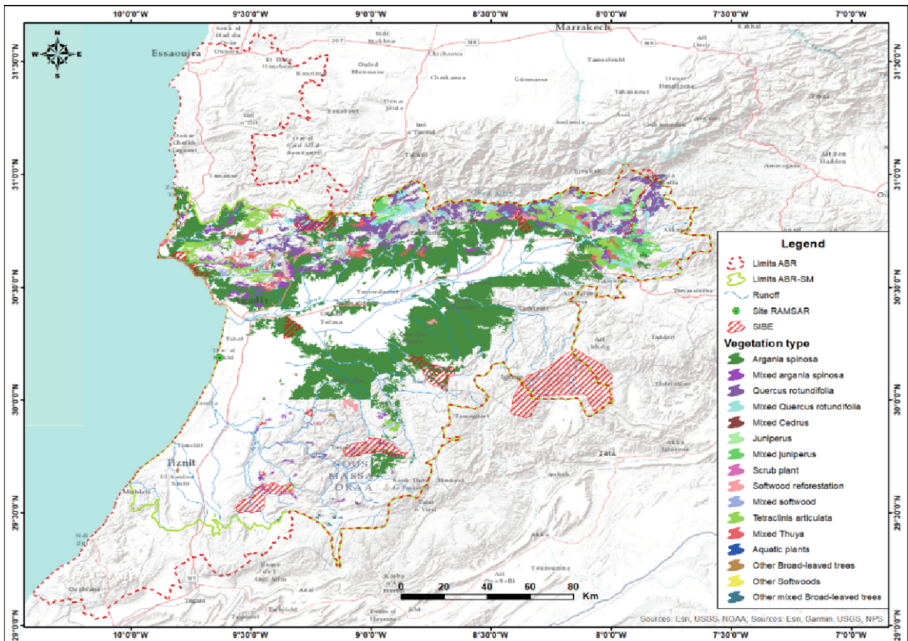
Fig. 5.   Authors, vegetation type in ABR-SM, 2022 [8]

The ABR-SM includes 12 SIBEs and two national parks, namely the Souss-Massa National Park (PNSM) in its entirety and 1/3 of the area of Toubkal Park (Fig. 5). At the level of the PNSM, one wetland combining dunes, green areas and water were included in the RAMSAR list in 2005, namely the estuaries of the Souss and Massa wadis.

At the territorial level, the High Atlas area is home to a very significant mammal diversity, i.e., about sixty species of mammals (Fig. 6). The gradient of diversity gradually decreases towards the south of the territory (Fig. 5). There are endangered species in all units of the territory. These latter are particularly pronounced in the lowland zone and in the Western High Atlas.

| Fauna diversity			Floristic diversity		
Reptiles	Birds	Mammals	Other rare or very rare non-endemic remarkable plants	Remarkable endemic plants	Most remarkable endemic plants
Spiny eyed gecko (Quedenfeldtia trachyblepharus) Brosset's Saurodactyl, (Saurodactylus brushti) Fascinated Saurodactyl (Saurodactylus fasciatus) Western Whiptail (Uromastyx occidentalis)	Bald ibis (Geronticus eremita) Ferocious buzzard (Buteo rufinus) Lanner falcon (Falco biarminus) Peregrine falcon (Falco peregrinus) Booted eagle (Hieracetus pennatus)...	Barbary Sheep (Ammotragus lervia) The caracal lynx (Felis caracal) The gloved cat (Felis Libyaa) The Zorilla (Poecilactis Libyca) Genet (Genetta genetta) The striped hyena (Hyaena byaena) ...	Pistacia atlantica Laurus azorica Davallia canariensis Warionia saharae Linaria sagittata Sonchus pinnatifidus Lavandula pedunculata Anthemis pedunculata Cytisus grandiflorus ..	Senecio anteuphorbium Polygala balansae Lotus marocanus : rare Teucrium tananicum Teucrium rupestre Micromeria arganietorum Ighermia pinifolia....	Argania spinosa Dracaena draco subsp .ajgal Acacia gummifera Olea maroccana

Fig. 6. The floristic and fauna diversity in ABR-SM [10]

3 Pressure on the Environmental Resources: What're the Degradation Factors? For Which Impact?

3.1 Pressure on Water Resources: Precipitation Alarming Situation [11]

Pressure on Surface Water Resources. In a changing climatic context, the contributions in terms of precipitation continue to dwindle compared to normal, particularly in the Souss and Massa basins. This situation constitutes a real threat to the Water Supply Plan of the most populated metropolises in the Region, as well as to the strategic socio-economic sectors for the Region, namely agriculture, tourism and industry.

Pressures on Groundwater Resources. Indeed, all the generalized aquifers show a water deficit, except for the hydrogeological units of the lower Drâa basin, which are in equilibrium. In contrast, the water deficit is significant at the level of the Souss aquifer, for which the deficit was estimated at a volume of 283 million m3/year in 2007.

The analysis of the evolution of the equilibrium of this aquifer (Fig. 7) during the period 1976–2007 shows that the water table is in a state of water deficit, with the exception of the wet year 1996, when exceptional hydrological contributions were recorded
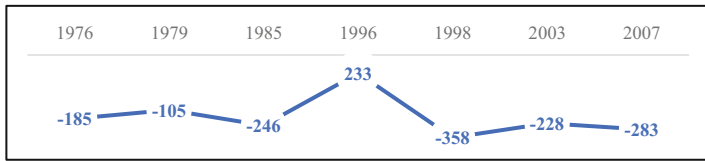
Fig. 7. Evolution of the water deficit for the Souss aquifer in Mm^3/year [10]

and the deficit was temporarily compensated. As for the Chtouka aquifer, the evolution of the water balance shows that this aquifer has been in hydraulic deficit since the 1970s, decreasing from 5 million m^3 in 1972 to -58 million m^3 in 2007. As for the Tiznit aquifer, the available assessments indicate that the sensitivity is relatively low. It has relatively well-preserved reserves, thanks to the recharge of deep aquifers. The aquifer, once in equilibrium (1973), now has a slight deficit, estimated at -1.5 Mm^3 for 2007

Decrease in Flows in Springs and Khettaras. The number and flow of springs and khettaras have decreased significantly in the Souss Plain. Springs were located along the Oued Souss riverbed between Igli and the Atlantic Ocean and also at the Aoulouz elevation. By the 1970s, nearly 62 springs were counted. By the early 1980s, most springs had dried up. The discharge of the Freija was only 56 l/s in 1986, compared to about 2 m^3/s in the early 1970s. Currently it is dry.

Risk of Saltwater Intrusion. The coastal strip of the area is particularly affected by water shortages. Here there is a risk of saltwater intrusion, which [12], is reaching worrying levels. The Bay of Agadir is the most affected, with areas where seawater has gained the upper hand over freshwater with extremely high salinity. Under these conditions, it seems to be a priority to set up a network to monitor salinity and its influence, but also to make adequate decisions on the use of the underground resources of the Chtouka aquifer, but also of the Souss aquifer, since these two systems are interconnected.

Impacts Related to the Degradation of Water Resources. Water resource degradation has low (yellowish color), moderate (orange color), and high (red color) impacts on the economy and health. This diagram explains the different impacts associated with this degradation and at what level it manifests.

Degradation of water resources has negative health and economic impacts. Economically, this degradation creates additional water treatment costs on the order of the reserve (Fig. 8). Beach erosion is evident along the entire coastline of the Reserve.
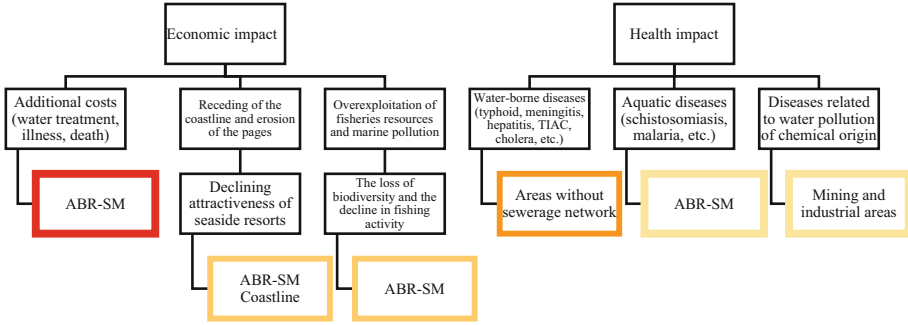
Fig. 8. Impacts associated with the degradation of water resources [13]

3.2   Factors of Soil Degradation by Desertification Effect

The ABR-SM area in general and the Arganeraie in particular are distinctly susceptible to the phenomenon of desertification and soil degradation. This vulnerability is mainly due to many factors acting simultaneously: Overgrazing, water erosion. Intensive agricultural activity and Mine-development.

Water Erosion. It's increasing at an alarming rate, especially in the High Atlas and Anti- Atlas Mountain ranges. It is exacerbated by the weak vegetation cover, the harsh topographic conditions and, above all, the poor distribution of rainfall, which is concentrated in the form of storms [7]. The resulting hazards negatively affect the durability of downstream dams, the fertility of agricultural land, and other infrastructure (roads, etc.). In addition, the growing population and the conversion of agriculture exacerbate the situation by reducing natural resources.

Intensive Agricultural Activity. Due to the limiting edapho-climatic factors, bour-type agriculture remains the most widespread in terms of area in the ABR-SM. However, the irrigated perimeters of this area are among the irrigation areas most affected by soil salinization. The affected area reaches 9,800 ha representing 29% of the irrigated area [13]. The loss of soil fertility caused by the reduction of organic matter is as harmful a form of degradation as salinization. It results from poor management of crop residues (no landfilling), low use of green manure (slurry and compost) and high mineralization of organic compounds. On the other hand, the introduction of monocultures remains the most feared cause. In fact, the organic matter content in soils is generally below 1.5%. The observed yield reductions are about 6 to 10% per year [14]. This agriculture mainly export-oriented, has developed in the plains with loose soils with high production potential and the necessary hydro-agricultural facilities. This has led to the pollution of groundwater, especially by nitrates, the salinization of the soil, the destruction of soil fauna and, consequently, the loss of soil fertility and the aggravation of the phenomenon of desertification.

Development of the Extractive Industry. All small mines located at the level of the ABR-SM are abandoned without redevelopment [15]. As for quarries, 21% of them, or 30 sites, are abandoned. This situation poses a serious threat to the environment and

requires accelerating the rehabilitation of mines and quarries to mitigate the negative impacts they cause.

Impacts Related to Land Degradation. Soil degradation has many economic, health, and environmental consequences. These consequences are listed in the figure below.
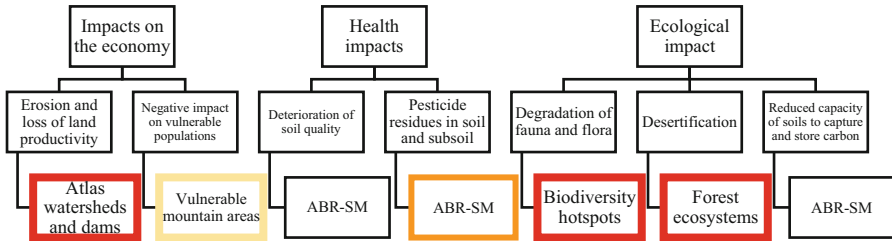
Fig. 9. Effects of soil degradation [27]

The most important impact caused by pressure on soil is desertification, which has negative ecological impacts on forest ecosystems and biodiversity. Erosion, in turn, has significant economic impacts on watersheds and dams, leading to siltation and consequent loss of soil productivity (Fig. 9).

3.3 Pressure on Forest Resources and Biodiversity

Overgrazing. It is caused by the increasing load of animals on grazing areas, which is disproportionate to the production and regeneration capacities of these areas. At ABR-SM, grazing pressure is exacerbated by the low production levels associated with continuous use over time, as there are no opportunities for herd movement. In addition, this area is relatively frequently visited by external herds, especially camels from the southern provinces [15]. The study of transhumance in the argan grove [16] shows that in recent decades, anthropogenic pressures on natural resources (intensive agriculture, urbanization, increase in livestock, etc.), combined with extreme climatic conditions, have led to profound dysfunctions of pastoral ecosystems in Morocco in general and in the geographic area of the argan tree in particular. These dysfunctions have been exacerbated by the social imbalances, the change in land status on rangelands (transition from collective to private use).

Indeed, the mobility of livestock in the Arganeraie area depends on rainfall and the availability of water points for watering during the summer season. In the context of climate change, this problem of overgrazing will be exacerbated by recurrent dry years and the rangeland degradation.

Intensive Agricultural Activity. The development of agriculture in the Souss Massa plains has been at the expense of the argan forests, especially since the 1970s. This decline mainly affected the argan plantations in the plain, such as the Admin forest, where the rate of degradation due to cultivation was estimated at about 600 ha/year

during the period 1969–1986 [17]. The effects of forest displacement by farms include, above all, intensification of production and expansion of greenhouses, accompanied by depletion of water resources and excessive use of chemical fertilizers and pesticides.

Urbanization and Anthropogenic Pressure. At ABR-SM, in particular, the increasing expansion of built-up areas at the expense of the argan forest is a real evil, especially in the areas adjacent to the major urban centers of our study area. In fact, with the expansion of the cities, the argan plantation has been transformed into a land reserve earmarked for real estate projects, social infrastructure, quarries, etc. For example, during the period 1969–2006, an area of 1,400 ha of the Mesguina forest [3] was diverted for urbanization, representing a significant loss of density.

After identifying and diagnosing the ecological factors of the environmental resources of the ABR-SM area. Thereafter, exposed the pressure on these factors and analyze them. We allow ourselves in this last point to see the measures taken by stakeholders to manage the ABR-SM area and how are these measures institutionalized the territorial level?

4   The Environmental Management of the ABR-SM: Between Institutionalization and Resilience for Sustainable Development

In this part, we will study the regulatory, institutional measures as well as the programs and strategies implemented by stakeholders for the sustainable management of the territory ABR-SM.

4.1   Moroccan Regulatory and Legislative Arsenal and the Challenges of Application

Several texts of laws have been governed in order to regulate the sustainable management of the previous sectors (Water, soil and biodiversity resources). In this context, we will see the different legal standards established by Morocco in terms of management of the environment, water, soil and biodiversity of the ABR-SM (Table 1).

There are still regulatory texts elaborated by the ministries, namely: the text on the conservation and use of the forest. This text allows, first of all, the delimitation and the registration of the buildings of the state (Dahir 03 January 1916, Dahir 24 May 1924) [21]. The management of the forest property is regulated by the Dahir of October 10th, 1917 [22], which refers to the conservation and use of the forests. This Dahir grants rights of use to the rights holders (riparian populations), "which are due to those who have always benefited from them" [23]. In terms of biodiversity, it was necessary to regulate activities related to fishing and hunting [24]. Moreover, for the protection and delimitation of the argan forest, a Dahir was issued on March 4, 1925 [25], regulating the rights of use of the traditionally exploiting tribes and factions in the Argan Zone. These are - collection of dead wood - fruit picking - herd paths - land use - cutting firewood, charcoal and timber - cutting branches for fences - removal of soil, sand and stone. These different texts allow strengthening the relationship between the forest and the rural population

Table 1. Legislative and regulatory texts relating to the organization and management of water, soil and biodiversity resources

Water resources	Soil resources	Biodiversity
Law No. 10–95 of 1995 on Water Management [18]: aims to highlight the evolution of resources and also the national needs for investment and exploitation. The water shortage has imposed a limit on the rights of the owners and in no case cede them (rights) only to the owners of agricultural funds. Moreover, industries are taxed according to the "pollution units" discharged, i.e., the emission of pollutants. This law determines the holders of permits valid for 20 years (selection) and establishes the rejection points. This law meets the definition of miracle, but does not meet the criterion of "voluntariness" and the principle of negotiation of Coase	Law No. 11–03 on the Protection and Improvement of the Environment (2003) [19]: stipulates (first section) the development of soil and subsoil resources through rational exploitation. It defines the process of land development for agricultural, industrial, mining, archaeological research, etc., which is subject to giving authorization	Law No. 22–07 on Protected Areas [20]: This law designates the competent authority to ensure the management, control and monitoring of protected areas in coordination with local authorities. In order to preserve the ecological balance, decisions are made in the areas of the forest estate, which make it possible to classify an area, a parc or a reserve by material damage[1]

and encouraging private investment in the forest. In order to encourage investment in environmental protection projects, a system of financial and fiscal incentives has been established that allows for the establishment of government subsidies, partial or total exemption from customs duties, taxes or levies, long-term loans, low-interest loans and any other appropriate incentive measures [26].

4.2 At the Institutional Level

Several institutional actors operate at the level of ABR-SM. However, the management of ABR-SM is controlled by the agency of Water and Forest;

The Division of Parks and Nature Reserves/DLCDPN/DEF & The South-West RDW FCD-SW: A governmental institution, central actor and cornerstone of the management of the entire ABR project & The South-West RDW FCD-SW: A structure responsible for the implementation of forest policies at the regional level, the development of ten-year plans and annual program contracts, and the implementation of annual programs.

---

[1] Material damage is defined by the limitation of previous activities against compensation for the benefit of the owner or the beneficiary under the conditions set by the implemented laws [33].

The Wilaya of Agadir Ida Ou Tanane: A regional administrative structure that follows the borders of the Souss-Massa region and includes the prefectures of Agadir Ida Ou Tanane and Inezgane Ait Melloul and the provinces of Chtouka Ait Baha, Tiznit, Taroudant and Tata.

The Souss-Massa Region: a territorial entity under public law, a strategic actor in the coordination of "sustainable development" actions at the regional level.

The Province and the Prefecture: a constitutional institution whose powers are defined by Dahir [27].

The Territorial Community: basic territorial community with legal personality and administrative and financial autonomy.

ANDZOA (National Agency for the Development of the Oasis and Argan Tree Zones): public body subject to state supervision, with legal personality and financial autonomy.

NGOs & Foundations: at regional and provincial levels, main actors in local development and conservation.

4.3   Resilience and Perspectives of Sustainable Development

Morocco has adopted programs and strategies in the process of sustainable development. These programs promote the mobilization of territorial actors, socio-economic balances and the adoption of cross-sectoral approaches. To alleviate the pressures in each sector, various resilience measures have been implemented, which we will consider in this part.

Water. The budget for implementing the objectives of the National Water Strategy is 82 billion dirhams. Within the framework of water resources management, several other strategies and programs have been launched: the National Sanitation Plan, which aims to achieve a connection rate to the sewage network in urban areas of 75%, 80% and 100% in 2016, 2020 and 2030, respectively. As well as achieving 100% processed wastewater by 2030 [28]; As well as the Group Drinking Water Supply Program for Rural Populations (PAGER), which is based on access to drinking water for the entire rural population (access rate to drinking water 61% in 2004). These national strategies and programs are based, at the regional level, on the summaries of the Master Plans for the Integrated Development of Water Resources (PDAIRE), prepared by the authorities of the watershed in the framework of decentralized planning, which is a planning tool for the management and development of water resources.

Soil. The situation of land resources is under great pressure. To alleviate the extent of this pressure, Morocco adopted a national action plan to combat desertification (PAN LCD) in June 2001. This plan makes it possible to promote local dynamism and strengthen income-generating initiatives while supporting the process of combating desertification. And to combat erosion, the National Plan for Watershed Development (PNABV) proposes mechanisms to protect soils from water erosion and to restore ecosystems.

Biodiversity. Among the strategies and programs for the protection of forests and biodiversity, the National Strategy and Action Plan for Biodiversity in Morocco (SPANB, 2016–2020) is noteworthy; it is a roadmap with the following priorities: The conservation of ecosystem services - The sustainable use of biodiversity - The strengthening of

biodiversity governance - The valorization of biodiversity knowledge - The promotion of citizens' will and behavior change. In order to update biodiversity data, Morocco has launched a national assessment of biodiversity and ecosystem services. This assessment aims to strengthen the link between science and policy on biodiversity, ecosystem functions, and ecosystem services. At the regional level, the regional agency for Water and Forest and for Combating Desertification (AREFLCD) are preparing a ten-year plan for forestry development and combating desertification. The agency of Water and forest localized in Agadir is the management body for the ABR in general. To date, the management body has prepared two action plans for the ABR based on a participatory approach of all stakeholders of the different economic sectors operating at the ABR level. The first covers the period 2008–2017 and aims to strengthen the argan sector and intensify scientific and genetic research on the argan tree [29]. The second phase of the ABR assessment was completed in 2020 for the period 2018–2027.

5   Conclusion

This work was based on the diagnostic study and the state of natural resources of ABR-SM in terms of water resources, soil resources and biodiversity. But these resources are unfortunately not immune to various stresses that contribute to the vulnerability and imbalance of the ecosystems of ABR-SM (desertification, water erosion, overgrazing, intensive agriculture, urbanization, etc.).

Measures and laws have been taken to shape the process of environmental management of the ABR-SM. At the institutional level, the management of the Reserve is supported by the responsibles for water and forests, coordinating with other institutional actors, the issue of governance thus imposes itself. Management bodies have been created for the proper management of the resources of the ABR-SM, namely: the Management Body, the Participation and the Scientific Committee. The management body is represented by the Partnership Service within the water and forests responsibles. It is responsible for planning and implementing programs and developing partnerships in coordination with other stakeholders. The Participatory Body, whose role is to monitor compliance with the objectives, strategy and guidelines for the development and management of the reserve, is chaired by the Wali. The Scientific Committee, which includes representatives from research institutions, non-governmental organizations, associations, etc. Its mission is to program, monitor and evaluate scientific research to understand the dynamics and impacts of the environment and the evolution of biodiversity. At the strategic level, water policy is based on the following indicators: Connection rate to the sewage network - Volume of treated wastewater - Access rate to drinking water. In fact, the RBA-SM has achieved a treatment rate of 60% of the collected water and a connection rate to the sewage network in urban areas of 80%. And by 2030, the volume of treated wastewater is expected to reach 100% [30]. The access rate to drinking water reached 61% in 2004. For soil resources, the following indicators were used: Water erosion, soil salinity, and the presence of quarries. The region's dams received only 30 million cubic meters of water for the hydrological year 2019–2020, instead of 476.5 million cubic meters of water in a normal year [31]. In terms of biodiversity, several indicators were identified, including pastures, agricultural activities, urbanization and anthropogenic pressure.

The new Morocco Forest Strategy 2020–2030 will be implemented with an approach that aims to achieve "inclusive, sustainable and prosperous management that reconciles Moroccans and the forest." It is based on four axes: differentiation and development of spaces according to their destination - reinvention and structuring of the participatory approach - investment and modernization of the core business - reconstruction of the institution around the authority. This new forest management is based on institutions for dialog with the actors and structures of the territory, oriented to the interests of rights holders. Can the environmental stakeholders go towards a convergence of interests or even a consensus between the effective involvement of local populations and the conservation of biodiversity? What is the reserve future in the process of institutional transforming (from public administration into an independent agency) and establishing ODF "forest development organizations"? Will be there a synergy between the different governance instances or just speeches?

References

1. Agency of Water and Forest Souss-Massa: Elaboration du Nouveau Plan d'Action de la ABR 2018–2027. Agadir, Morocco (2020)
2. Construction by the authors based on administrative distribution 2015 and data from DREFLCD-SO. Agadir, Morocco (2022)
3. SIREDD-Souss Massa, Situation Territoriale de lutte contre le Réchauffement Climatique. Souss Massa. Morocco (2016)
4. Construction by the authors based on Digital Elevation Model 30 m and Data from Hydraulic Basin Agency. Souss Massa (2022)
5. ABHSM: http://www.abhsm.ma/. Accessed 12 Oct 2022
6. ABHSM: Renforcement de la recharge artificielle de la nappe du Souss. https://www.riob.org/IMG/pdf/recharge_souss_05.pdf. Accessed 12 Jan 2022
7. ABHSM: http://www.abhsm.ma/. Accessed 13 Jan 2022
8. Regional Observatory of the Environment de Souss-Massa, collected Data. Souss Massa. Morocco (2021)
9. Construction by the authors based on U.S. Geological Survey, Satellite Images Landsat 08 (2022)
10. Construction by the authors based on data from DREFLCD-SO, Elaboration du Nouveau Plan d'Action de la ABR 2018–2027. Agadir. Morocco (2022)
11. Décret n° 2-91-518 du 26 moharrem 1412 (8 août 1991) portant création du Parc national de Souss-Massa
12. Construction by the authors based on data from Rapport sur l'état de l'environnement -2019. Souss Massa region. Morocco (2022)
13. Données de l'ABHSMD, 2020
14. Badraoui M. Connaissance et utilisation des ressources en sol au Maroc (2006)
15. Inventaire des carrières dans la Région SM (2018)
16. Plan National de Lutte Contre la Désertification (2013)
17. Données 2012 de l'Agence Nationales du Développement des Zones Oasiennes et d'Arganier (ANDZOA)
18. El Yousfi, S.M.: La dégradation forestière dans le Sud-Ouest marocain: exemple de l'arganeraie d'Admine (Souss) entre 1969 et 1986; mémoire de 3ème cycle, Agronomie, Inst. Agron. Et Vétér. Hassan II, Rabat, 117 p. (1988)
19. Loi n° 10–95 de 1995 sur la gestion de l'eau (1995 complétée en 2005)

20. La loi-cadre n° 11-03 relative à la protection et à la mise en valeur de l'environnement (2003)
21. La loi n°22-07 des aires protégées
22. Dahir 03 Janvier 1916 portant règlement spécial sur la délimitation du domaine de l'Etat et Dahir 24 Mai 1924 portant sur l'immatriculation des terres
23. Dahir du 10 Octobre 1917 sur la conservation et 1 'exploitation des forêts
24. Articles 21-22-23, Dahir du 10 Octobre 1917 sur la conservation et 1 'exploitation des forêts
25. Dahir du 11 avril 1923 relatif à la pêche dans les eaux continentales et Dahir du 21 Juillet 1923 relatif au contrôle de la chasse
26. Dahir du 04 Mars 1925 relatif à la protection des forêts d'arganier et sa délimitation
27. Section IV : Les incitations financières et fiscales, Dahir n° 1-03-59 du 10 rabii I 1424 (12 mai 2003) portant promulgation de la loi n° 11-03 relative à la protection et à la mise en valeur de l'environnement (B.O. n° 5118 du 19 juin 2003)
28. Article 39, loi n°22-07 des aires protégées
29. Dahir du 15 février (1977)
30. ABHSM: http://www.abhsm.ma/, Accessed 2 Mar 2022
31. Idrassen, H., Boujrouf, S., Baki, N., El Ghiouan, S.: Coordination of actors and innovation: Which model for territorial integration of the Biosphere Reserve of Arganeraie in Morocco? Int. J. Innov. Appl. Stud. **35**(1), 50–62 (2021)
32. Laouina, A. : Rapport Prospective « Maroc 2030 » Gestion durable des ressources naturelles et de la biodiversité au Maroc. Haut-Commissariat au Plan, Morocco (2006)
33. Kadiri, A: https://fr.le360.ma/economie/stress-hydrique-la-situation-est-de-plus-en-plus-critique-dans-la-region-souss-massa-223973. Accessed 15 Feb 2022

Promote Green Mobility as a Mechanism for the Development of Sustainable Cities and Environmental Sustainability. The Case of the ValparaÍSo Trolley as a Green Means of Transport, Chile

Stefania Pareti[1(✉)], Vicente Valdebenito[2], Ignacio Tampe[3], and Claudia Bustamante[4]

[1] Universidad Andrés Bello, Santiago de Chile, Santiago, Chile
s.pareti@uandresbello.edu
[2] Universidad Católica de Valparaíso, Valparaíso, Chile
vicente.valdebenito@sansano.usm.cl
[3] Universidad Técnica Federico Santa María Valparaíso, Valparaíso, Chile
[4] Pontificia Universidad Católica de Chile, Santiago, Chile
claudia.bustamante@sansano.usm.cl

Abstract. The main objective of this study is to explore whether the promotion of green mobility turns out to be a mechanism for the development of sustainable cities and environmental sustainability. The Valparaíso trolleybus is selected as a case study, since (1) it is a green means of transportation, (2) it facilitates the urban mobility of the inhabitants, (3) it decongests traffic and pollutes the place, (4) they are part of the city's industrial heritage legacy, (5) in addition to being a green means of transport, they are a reminder of the city's heritage-tourism heritage. The methodology is carried out through an analysis of the historical route of the trolleybus in Valparaíso, followed by an analysis of the energy efficiency of this means of transport compared to other options. It is concluded that promoting green mobility does turn out to be a mechanism for the development of sustainable cities and environmental sustainability, as observed in the case of the Valparaíso tram.

Keywords: Trolebus · Urban mobility · Green transport · Smart city · Environmental sustainability

1 Introduction

The objective of this study is to study whether green mobility through trolleybuses in the city of valparaíso can contribute to the development of the port as a sustainable city and environment.

Valparaíso is the capital of the fifth region of Chile. It is located 120 km from the national capital Santiago and has about 300,000 inhabitants (Fig. 1).

It is characterized for being historically the main port city of the country, with a geo-graphical conformation in the form of an amphitheater [1]; which concentrates its

pop-ulation along 44 hills that surround the flat center of the city where public spaces, com-mercial and administrative centers and its relationship with the port and the bay are located. It saw its golden years around the 19th century, when it functioned as the main port of the capital, becoming a kind of cultural center where foreigners from all over the world converged in search of trade opportunities in the new republics of America. [2] Its history, the popular stilt architecture of the hills and the conservation of the cultural heritage left by foreigners who lived in the city, earned it recognition as a World Heritage City by UNESCO in 2003.

Fig. 1. Location and morphology of Valparaíso.

After the opening of the railway between Santiago and Valparaíso, the port saw its economic activity grow to the point of requiring new means of public transport in its urban area [3]. After a development in public transportation that began in 1863 with horse-drawn streetcars, 90 years later in 1953 the first 30 Pullman Standard TC-48 ′700' trolleybuses imported from the United States were launched under the administration of the public-private partnership Empresa Nacional de Transportes (ENT). By 2003, 16 of the 30 trolls were still in operation, which, within the framework of the recognition of Valparaíso as a World Heritage Site by UNESCO, were declared historical monuments. These trolleybuses are a means of transportation made up mainly of metal, 12.2 m long and with the capacity to carry 78 passengers [4].

Its main attraction for this research is that it works based on electricity through the power lines that cross the city, which can help in the creation of a city with sustainable logics. After more than 50 years, trolleybuses as a means of transport continue to function. Although they are no longer the same ones imported from the US, they have been added and replenished in number.

2   Theoretical Framework

The continuous expansion of urban fabrics, both in territorial extension and in population density, originates growing demands on the social infrastructure that allows meeting common needs. These dimensions are especially urgent in the case of developing countries, which tend to concentrate very low-income social segments on the periphery of their metropolises, living precariously and with markedly unequal access to the benefits of urbanization. The availability of an adequate urban transport infrastructure, which allows moving people and goods in a dignified, timely, reliable and economical way, undoubtedly integrates that core of common basic needs [5]. However, the development and continuous growth of the world population are the major factors which cause growth of energy consumption and increasing volumes of greenhouse gas emissions [6]. Although Sustainable Development constitutes the current dominant paradigm to guide the economic and social development of humanity. Despite the apparent global agreement about its importance, its practical application is difficult to implement, especially in the Latin American urban environment, where there are multiple gaps that separate the current city from the desired sustainable city [7].

The case of the trolls in the framework of the heritage city of Valparaíso, represents a path of conservation and development of green technologies in a state that is found in few parts of Latin America. Public transport has undergone major changes in recent years. In particular, they relate to the issue of environmental impact [8]. Trolleys as a means of transportation return to the fore in the context of the need for new transportation systems that produce zero emissions and respect the new surface landscape [9] due to the need as a society to reduce our energy impact in the planet. The ability to move public transport based on electricity can mean significant energy savings based on fossil fuels. A sustainable city is a city that follows ecological principles, the idea of eco cities emerges as a new approach to sustainable development, resulting in an environmentally friendly city in terms of pollution, land use and reduction of waste. The causes that contribute to global warming, the trolls comply with developing some of the aspects that characterize sustainable cities, such as: the use of renewable energy, improved public transport systems and promotion of pedestrianization to reduce fuel emissions from automobiles [9].

In the framework of mobility, the possibility of adding green transport to the conception of smart cities can mean an important development in the conception of a sustainable city.

The goal of the smart city concept is modern urban management using technical tools that offer state-of-the-art technologies, considering the applicable ecological standards while saving resources and achieving the expected results [10]. As a city, Valparaíso has the advantage of already having a skeleton and green urban transport assets, which reduces the task of implementing it from scratch, maintaining it, and improving it. Even in this favorable scenario, the trolls have been on the verge of disappearing on several occasions, mainly due to debts due to lack of state subsidies.

Chile as a member country of the OECD has to deal with the standards of the member countries.

In the case of Europe, initiatives have been carried out for years based on the idea of green public transport in which Only low-emission and zero-emission vehicles are to be

used in transport, and mainly those that are powered by electricity in public transport. The development of battery technologies has led to a revolution in the range and operational capabilities of electric buses in the last decade [8]. As examples of public transport based on electricity, we have Poland with the.

The trolleys, as they work on electricity with the city lines, have no emissions and, in contrast to other gasoline-based transports that have been operating in the city since 1965, such as the buses [9], have saved significant amounts of fossil fuel.

3   Methodology

To determine the relevance of the use of the trolleybus in the city of Valparaíso, considering its low energy impact, its contribution to urban mobility and its heritage legacy in the city, this research will first carry out an analysis of the route of lines 801 and 802 of the Valparaíso Metropolitan Transport, corresponding to the routes made via trolleybus. Understanding that the logic behind the route results in understanding the environmental impact produced by this means of transport within the city and also how it contributes to urban mobility. Secondly, an analysis of the energy efficiency of this type of transport will be carried out in comparison with traditional means of transport powered by gasoline or diesel. Understanding that the use of electric public means of transport are methods of low environmental impact when the origin of the electricity used comes from an environmentally friendly source.

4   Results

4.1   Route Analysis

Valparaíso's trolleybuses are a method of heritage transportation, they have been operating in the city for 70 years since they were inaugurated. Being the only fleet of vehicles of this type in Chile. Currently the company owns a fleet of 30 trolleybuses, of which 16 of the Pullman Standard brand were declared historical monuments in 2007 by the National Monuments Council, being trolleybus No. 814 the oldest in operation in the world. The prolonged duration of these vehicles is due to the simplicity of their design, not putting unnecessary stress on any specific part (Fig. 2 and Table 1), and also to the maintenance carried out by the company in charge. (Metropolitan Transportation of Valparaíso). The trolleybus route turns out to be very beneficial for Valparaíso, not only does it connect to the historic center of the city at a low cost (0.3 USD), but its route passes through historic neighborhoods of the city, making a route of tourist attraction. There are currently two routes with power lines designed for trolleybuses: routes 801 and 802. In 2021 route 801 was reincorporated into the schedule, after 14 years of the lack of a trolleybus route through Valparaíso's main artery: Pedro Montt st. Also incorporating GPS location and LED lighting into the trolleys.

As can be seen in Fig. 3 and 4, the trolley routes in Valparaíso are in the nerve center of the city, where all the services it offers are located. The tours start at Argentina ave. Being the access to the city from Route 68, coming from Santiago, then they cross the almond neighborhood: route 802 passes through Colón st. at the foot of the hills,
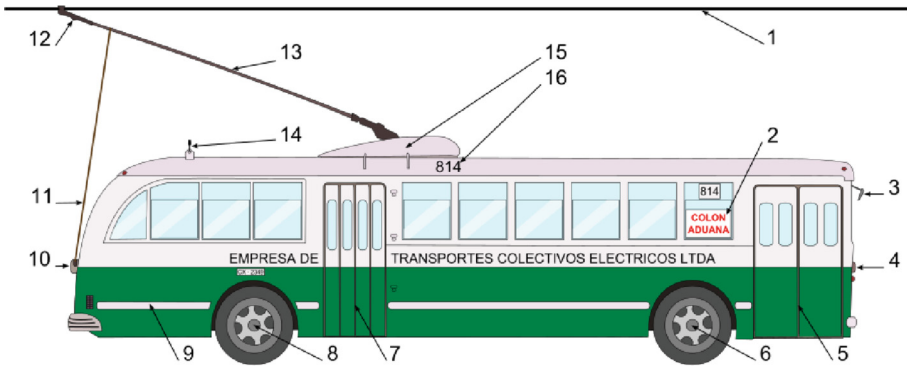
Fig. 2. Diagram of the basic components of a Trolleybus.

Table 1. Components.

1. Power Line	7. Rear doors	13. Trolley Hook
2. Route Sign	8. Rear dual axle	14. Trolleys or feathers
3. External rear view mirror	9. Decorative bars	15. Trolley Base
4. Headlights	10. Tensioner	16. Machine Number
5. Front doors	11. Rope	
6. Front single axle	12. Trolley Head	

Fig. 3. Trolley Route 801.Own Elaboration

while route 801 crosses Pedro Montt st. Where the commerce of the city is located. Both routes then continue along Avenida Brasil as they pass through the main squares of the city (Table 2). Arriving at Blanco st. The route crosses the historic area of Valparaíso, declared a World Heritage Site by UNESCO. The Victorian-style buildings correspond to the financial sector, where the branches of the main banks of the city are located, as well as port and commercial companies. After Sotomayor Square, they cross to the port district. Finally, the one-way tour ends at Wheelwhright Square. The return route crosses the same neighborhoods and monuments.

Fig. 4. Trolley Route 802. Own Elaboration

Table 2. Trolley routes schedule.

Route	Fare	Trip	Operative Days	Stops	Distance
801	250 clp (0,3 USD)	Baron Square to Wheelwhright Square (Through Pedro Montt st.)	Mo, Tu, Th, Fr, Sa Whole Year	18	6,99 km
802	250 clp (0,3 USD)	Baron Square to Wheelwhright Square (Through Colón st.)	Mo, Tu, Th, Fr, Sa Whole Year	38	9,04 km

4.2 Energy Efficiency Analysis

To estimate the energy efficiency of Trolleybuses, a comparative analysis was carried out between this type of transport and other means, mainly comparing energy consumption according to the fuel source administered for its operation, and their respective CO_2 and Greenhouse Gas emissions. (GHG) [11].

The Valparaíso Trolleybuses use electricity as a source of energy (Fig. 5), distributed through a single electrical network divided into four 600 VDC circuits, which are fed with alternating current through two six-phase rectifiers [12]. The operation of this type of transport lies in the administration of electricity from direct current (DC) between 550 V and 750 V [13], whose network is divided into sections of energy distribution fed by traction supply cables from substations that convert electrical energy from the alternating current network to direct current for vehicles [13]. In other words, trolleybuses correspond to an electro-mobile means of transport, characterized by using drive or traction systems by means of electrical energy [14].

Electromobility generates multiple benefits around sustainable development in the environmental, energy and economic fields, since it is an alternative to reduce CO_2 emissions [14]. The implementation of electromobility as a method of transport at the urban level is inserted more and more strongly in the global agenda against climate change, since it corresponds to a favorable alternative in the reduction of CO_2 emissions and other GHG with respect to the use of transport conventional land from motorized vehicles. According to the National Inventory of Greenhouse Gases (INGEI), conventional
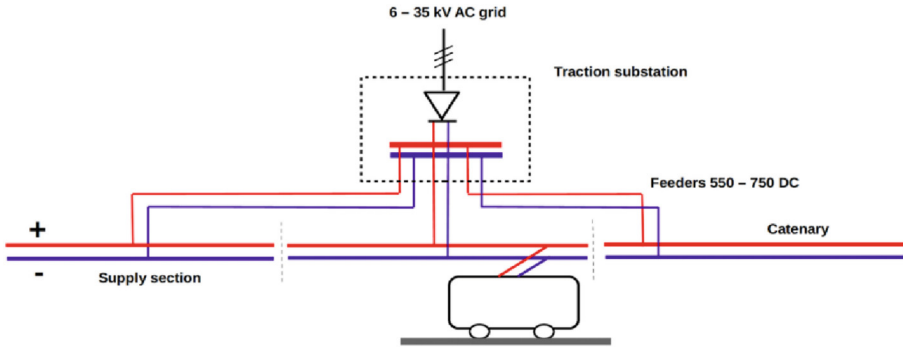
Fig. 5. Fuente: [13]

land transport, which considers buses, trucks, light vehicles and motorcycles (among other types of transport), reaches 24.1% of the responsibility for GHG emissions in Chile compared to other sectors of the industry, equivalent to 37 Gton of CO_2e [15]. In the last decade, energy consumption within the Transportation sector has tended to increase, whose peak is recorded in 2019 with 110,335 TCal consumed (Table 3), being responsible for 33% of total fuel consumption compared to other sectors [16].

Table 3. Change in energy consumption in the Transport sector.

2010	2011	2012	2013	2014	2015	2016	2017	2018	2019	2020
84.597	87.189	87.707	93.910	89.942	95.661	100.936	104.113	108.154	110.335	94.064

Source: Comisión Energía Abierta (2022)

Regarding energy consumption according to the fuel source, in this case petroleum derivatives versus electricity, according to the national energy balance for the year 2020 in Chile, 98.89% use of petroleum-derived fuels was registered in the sector. Transport, contrasted with only 1.11% use of electrical energy for its operation (Table 4). In contrast, as indicated in Tables 5 and 6, GHG emissions by type of transport in the Valparaíso region reach their highest numbers with regard to fossil fuel land transport, reaching their peak during the year 2018 with 2,611.7 ktCO2eq, as opposed to the 3.2 $ktCO_2$eq recorded by land transport based on electricity. Comparatively, GHG emissions from fossil fuel versus electric-based fuels are considerably opposite, with electromobility accounting for less than 0.2% of total fossil fuel GHG emissions.

Table 4. Fuel consumption in the transport sector, year 2020.

National energy balance of the Transport sector to the year 2020		
Fuel source	Energy consumption (TCal)	Percentage
Refinery-Petroleum	93.017	98,89%
Electricity	965	1,11%
Total	**94.064**	**100%**

Source: Balance Nacional de Energía (BNE) (2022)

Table 5. GHG emissions by type of transportation in the Valparaíso region.

Transport to fossil fuels (in ktCO$_2$eq)									
Transport type /Year	2010	2011	2012	2013	2014	2015	2016	2017	2018
Road transport	1.795,2	1.895,3	1.923,2	2.167,0	2.085,8	2.253,4	2.438,2	2.507,3	2.611,7
Railway	5,5	5,7	5,7	5,4	8,5	0,0	9,6	9,7	12,0
Marine transport	314,3	474,9	356,5	656,5	590,8	364,3	509,3	447,2	373,0
Aviation	26,0	22,4	32,4	28,2	27,5	49,6	43,4	14,6	18,1
Off road transport	93,9	88,6	86,8	98,7	98,6	103,3	103,0	107,2	103,2
Total	**2.235,0**	**2.486,8**	**2.404,6**	**2.955,8**	**2.811,2**	**2.770,6**	**3.103,5**	**3.086,0**	**3.118,0**

Source: Balance Nacional de Energía (BNE) (2022).

Table 6. GHG emissions by type of transportation in the Valparaíso region.

Transport to electricity (in ktCO$_2$eq)									
Transport type /Year	2010	2011	2012	2013	2014	2015	2016	2017	2018
Road transport	0,2	0,6	0,6	0,8	2,9	2,1	2,7	5,3	3,2
Railway	4,6	4,7	4,8	5,6	5,3	5,3	13,2	0,0	6,7
Marine transport	1,4	0,0	0,0	0,0	0,0	0,0	7,1	6,8	2,4
Aviation	NO	NO	NO	NO	NO	NO	NO	NO	NO
Off road transport	NO	NO	NO	NO	NO	NO	NO	NO	NO
Total	**6,2**	**5,3**	**5,5**	**6,4**	**8,2**	**7,3**	**23,0**	**12,1**	**12,3**

Source: Ministerio de Medio Ambiente Chile (2020).

5   Conclusion

This study explores how green mobility can contribute to the sustainable development of cities and settlements. The case of Valparaíso trolleys is analyzed as a method of patrimonial, public, accessible and sustainable transport. The daily use of trolleybuses in Valparaíso has been operating for 70 years and has become part of the city's identity, running through its historic area.

Trolley routes run through the most polluted area by private vehicles in the city; the center. And, being the trolleys an electric vehicle, they contribute to reduce greenhouse gas emissions produced by gasoline and diesel vehicles in the most critical sectors of the city. Promoting public and sustainable mobility. In addition to connecting the city center in a sustainable and low-cost way, the trolley route runs through historical areas declared World Heritage Sites by UNESCO, giving the route a tourist and educational attraction. This heritage tour promotes the conservation of the city's heritage and forges the identity of the place. Promoting sustainable development, taking care of its history and the influence it had on its golden years.

The use of electric vehicles in public transport, especially in areas with high vehicular traffic, is an alternative that could radically reduce GHG emissions in cities and settlements. Not only reversing the effects of the climate crisis, but also improving air quality for residents. However, currently 20% of GHGs are produced by means of transport, with road transport vehicles being responsible for the vast majority. Where 99% of vehicles run on fossil fuels. For this reason, vehicles with intensive operation fleets and high annual mileage, such as public transport, can greatly benefit from using electric vehicles. In addition, the high costs of current electric vehicles make it difficult to acquire them privately, especially in countries far from the leading countries in electromobility. This means that the greatest benefits of this technology would be in public transport.

References

1. Eing, C.: Transporte Sostenible, Programa Internacional de Cooperación Urbana (n.d.)
2. Memoria Chilena: Valparaíso, Su Epoca de Esplendor (2021). http://www.memoriachilena.gob.cl/602/w3-article-7670.html
3. Micrópolis (N.A.): Valparaíso, un siglo de historia visual del transporte público. http://www.micropolis.cl/relatos/valparaiso/
4. Cruz. A.:Trolebuses De Valparaíso: Otra Mirada (2020) . https://www.blog.recorrido.cl/destinos/trolebuses-de-valparaiso-otra-mirada/#:~:text=Son%20trolebuses%20articulados%20construidos%20en,y%20capacidad%20para%20124%20pasajeros
5. Sanchez, R., Lupano, J.: Movilidad Urbana Sanchez Políticas de movilidad urbana e infraestructura urbana de transporte (2008)
6. Miskins V, Baublys J, Konstantinavičiūtė I, Lekavicius V. Aspirations for sustainability and global energy development trends
7. Saldía, L.: El Ambiente y el Desarrollo Sustentable en la Ciudad Latinoamericana (2009)
8. Ausubel, J.H., Marchetti, C., MeyerAusubel, P.S.: Toward green mobility: the evolution of transport (1998)
9. Polom, M.: Implementing electromobility in public transport in Poland in 1990–2020. A review of experiences and evaluation of the current development directions (2021)
10. Frenning, A.: Working Group for Sustainable Cities at Harvard University (2020)

11. Winkowska, J., Szpilko, D., Pejić, S.: Smart city concept in the light of the literature review (2019)
12. Identifica puntos de riesgo y reduce costos de la energía con apoyo de Dóminet/Prevent N.A. (2005). http://www.emb.cl/electroindustria/articulo.mvc?xid=2690&tip=6&xit=trolebuses-de-chile-identifica-puntos-de-riesgo-y-reduce-costos-de-la-energia-con-apoyo-de-dominet/prevent)
13. Wolek, M., Wolanski, M., Bartłomiejczyk, M., et al.: Ensuring sustainable development of urban public transport: a case study of the trolleybus system in Gdynia and Sopot (Poland) (2021)
14. https://www.sciencedirect.com/science/article/pii/S095965262033852X
15. Ministerio de Energía N.D. Plataforma De Electromovilidad. https://energia.gob.cl/electr omovilidad/introduccion#:~:text=%C2%BFQu%C3%A9%20significa%20entonces%20e lectromovilidad%3F,a%20distintos%20medios%20de%20transporte.&text=La%20electro movilidad%20genera%20m%C3%BAltiples%20beneficios,ambiental%2C%20energ%C3% A9tico%20y%20econ%C3%B3mico)
16. Ministerio del Medio Ambiente: Inventarios Regionales de Gases Efecto Invernadero, serie 1990–2016 (2021)
17. Ministerio de Energía (2020) Variación del consumo energético.: http://energiaabierta.cl/vis ualizaciones/consumo-por-sector-de-energia/

Renewable Energy and Clean Energy Technology

Solar Rooftop PV Power Generation for a Commercial Building in Thailand

Piyanart Sommani[1(✉)], Jiraporn Nookwan[1],
and Anchaleeporn Waritswat Lothongkum[2]

[1] Department of Electrical Engineering, School of Engineering, King Mongkut's Institute of Technology Ladkrabang, Bangkok 10520, Thailand
piyanart.so@kmitl.ac.th

[2] Department of Chemical Engineering, School of Engineering, King Mongkut's Institute of Technology Ladkrabang, Bangkok 10520, Thailand

Abstract. Solar energy is significant potential for power and heat production. The Alternative Energy Development Plan 2018–2037 (AEDP2018) developing by Thailand's Ministry of Energy demonstrates that solar energy is a key role in renewable energy utilization, especially for power generation. In general, solar photovoltaic (PV) technology is the most common type of solar power generation technology. This paper presented a potential of using grid-connected solar PV power generation system for the rooftop of a commercial building. The design and simulation of the solar rooftop PV power generation system and the economic analysis were accomplished. The installation of 1.85 MWp grid-connected solar PV power generation system on the rooftop area required 3,440 pieces of 540 Wp solar panels. By using PVsyst version 7.2, the solar panel configuration was connected in 20 pieces/string in series and 172 strings in parallel, with 80 kWac string inverters of 18 units. The simulated results of produced energy, specific production, and performance ratio were 2,678 MWh/year, 1,442 kWh/kWp/year, and 80% respectively. As a result, the energy cost saving was 269,317 USD with payback period (PB), net present value (NPV), and internal rate of return (IRR) of 6.37 years, 1,062,430 USD, and 15%, respectively. In conclusion, the installation of 1.85 MWp solar rooftop PV power generation system is technically feasible for the investment.

Keywords: Solar rooftop · PVsyst · Commercial building

1 Introduction

Renewable energy from solar energy, wind energy, biomass, municipal solid wastes (MSW) and others has been considered to substituting fossil fuels for decades. The Ministry of Energy of Thailand, thereby, notifies the Alternative Energy Development Plan 2018–2037 (AEDP2018) to promote the utilization of various renewable energy [1]. Solar energy is the most abundant and plays an important role in accomplishing the AEDP's plan. The target of solar photovoltaic (PV) power plant and rooftop power system is 12,139 MWp, a double capacity of the AEDP2015. It is remarkably that the

PV floating system started in the AEDP2018 to achieve its target of 2,725 MWp. On the other hand, the target of solar heat consumption is downward to 100 ktoe. Based on the solar energy status, as shown in Table 1, from Thailand Alternative Energy Situation 2020 Report [2], the central part of Thailand has the highest amount of on-grid installed capacity and heat consumption. Figure 1 illustrates the distribution of solar PV power plant and rooftop power system in 2020.

Table 1. Solar energy status in Thailand in 2020 [2].

Region	On-grid installed capacity (MW)	Heat consumption (ktoe)
Northern	654.10	2.98
North-eastern	439.93	1.12
Central	1,802.03	5.91
Southern	53.05	0.56
Total capacity	2,949.11	10.57

Solar PV technology is a proven technology worldwide for power generation [3, 4]. It is a competitive technology for power generation after a decade due to dramatic cost declines. The total installation costs of solar PV declined about 74% from 2010 to 2018, because of lower cost of solar PV modules and a balance-of-system in the solar PV power generation market [5]. Several review and research articles as well as the case studies regarding solar rooftop PV power systems in Thailand are widely reported in terms of technical performances, economic feasibility, and environmental impacts [6–14]. It is notably observed that the installation of solar PV power system on the rooftop of commercial and residential buildings has continuously increased in terms of the energy efficiency improvement and building space utilization in electricity generation. It is, therefore, this paper studied on technical and economic feasibility of grid-connected solar PV power generation system installed on the rooftop of a commercial building in Thailand.

2   Methodology

A commercial building in this study is located at Prachuap Khiri Khan province which is in the central part of Thailand. The feasibility study steps are described as follows:

2.1   Collect the Relevant Data and Electricity Consumption of the Commercial Building

The location and geographic coordinate system of the commercial building, the amount of solar irradiation, the rooftop structure and area, and the annual electricity consumption were collected on-site at the commercial building, from the available records, and by interviewing the building owners and solar PV system experts.
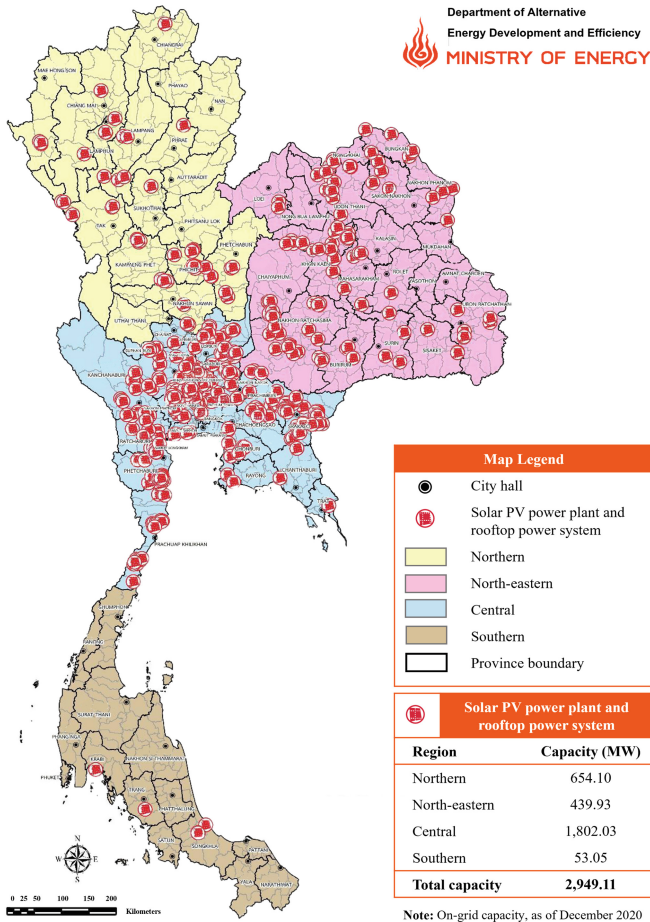
Fig. 1. Thailand solar PV power plant and rooftop power system in 2020 [2].

2.2 Design and Simulate the Solar Rooftop PV Power Generation System by PVsyst Version 7.2

PVsyst is a PC software for studying, sizing, and data analysis of complete PV systems [15]. The PVsyst can be applied to grid-connected, stand-alone, pumping, and DC-grid (public transportation) PV systems. It combines extensive meteo and databases of PV system components, including general solar energy tools. In this study, PVsyst version 7.2 was used to design and simulate the grid-connected solar rooftop PV power generation system of the commercial building.

2.3 Evaluate the Economic Feasibility of the Solar Rooftop PV Power Generation System

Key indicators which are commonly used for the economic feasibility of the solar rooftop PV power generation system includes the payback period (PB), the net present value (NPV), and the internal rate of return (IRR) [4].

- PB is the time required to recover the initial investment cost, thus, it equals initial investment cost divided by net annual cash flow of the project.
- NPV is the difference between the present value of cash inflows and cash outflows over a project period, defined by Eq. (1).

$$NPV = -I_0 + \sum_{t=1}^{n} \frac{ES_t}{(1+i)^t} \tag{1}$$

where I_0 is the total initial investment cost; ES_t is the energy cost saving; i is the discount rate which is determined at 7% according to the effective interest rate [16]; and n is the project period which is considered at 25 years for the solar PV project.

- IRR is the discount rate that makes the NPV of all cash flows zero in the discount cash flow analysis, defined by Eq. (2).

$$NPV = 0 = -I_0 + \sum_{t=1}^{n} \frac{ES_t}{(1+IRR)^t} \tag{2}$$

3 Results and Discussion

3.1 Rooftop Area of the Commercial Building and the Electricity Consumption

The case study commercial building is located at the latitude of 12°34′7″N and longitude of 99°57′28″E. According to the data on solar irradiation, the total solar irradiation in 2020 was at 1,731.5 kWh/m^2 [17]. It was found that the existing roof structure of the building can withstand the additional weight of solar core system components, including PV modules, their accompanying mounting structure, and inverters. The rooftop area of 21,500 m^2 is sufficient to install solar PV power generation system together with enough space for maintenance and inspection activities. The data on electricity consumption of the commercial building was obtained from the electricity bills in 2020, showing the maximum electricity consumption of 4.9 MWp in March.

3.2 Grid-Connected Solar Rooftop PV Power Generation System

Specifications of PV modules and inverters are shown in Table 2. The installation of 1.85 MWp grid-connected solar PV power generation system on the rooftop area required 3,440 pieces of 540 Wp solar panels. The design layout of PV module installation on the rooftop is presented in Fig. 2.

Table 2. Technical specifications of PV modules and inverters.

Component	Type	Capacity	Quantity	Total capacity
PV modules	Monocrystalline half cell	540 Wp	3,440 pieces	1,858 kWp
Inverters	String	80 kWac	18 units	1,440 kWac
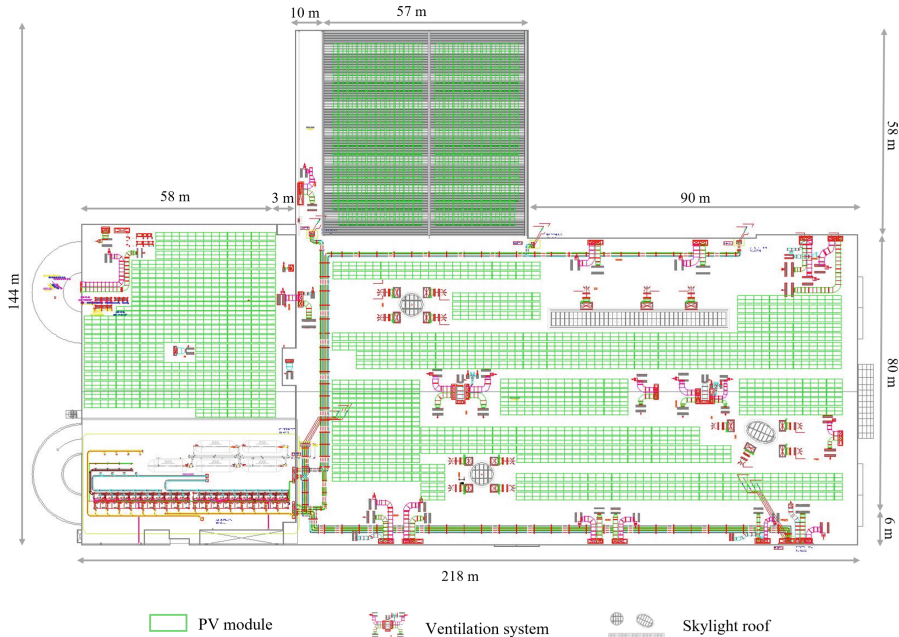
Fig. 2. Layout of PV module installation on the rooftop by AutoCAD.

By using PVsyst version 7.2, the solar panel configuration was connected in 20 pieces/string in series and 172 strings in parallel, with 80 kWac string inverters of 18 units. Figure 3 demonstrates the simulation results of produced energy, specific production, and performance ratio of 2,678 MWh/year, 1,442 kWh/kWp/year, and 80%, respectively. As shown, the installed capacity of the grid-connected solar rooftop PV power generation system is 1.85 MWp; however, the maximum power consumption required for the commercial building in 2020 is 4.9 MWp. To gain sufficient power, therefore, the installation of additional solar PV power generation system will be done.

The flow of solar energy and losses from the global horizontal irradiation to the energy produced to the grid by the 1.85 MWp grid-connected solar rooftop PV power generation system is shown in Fig. 4.
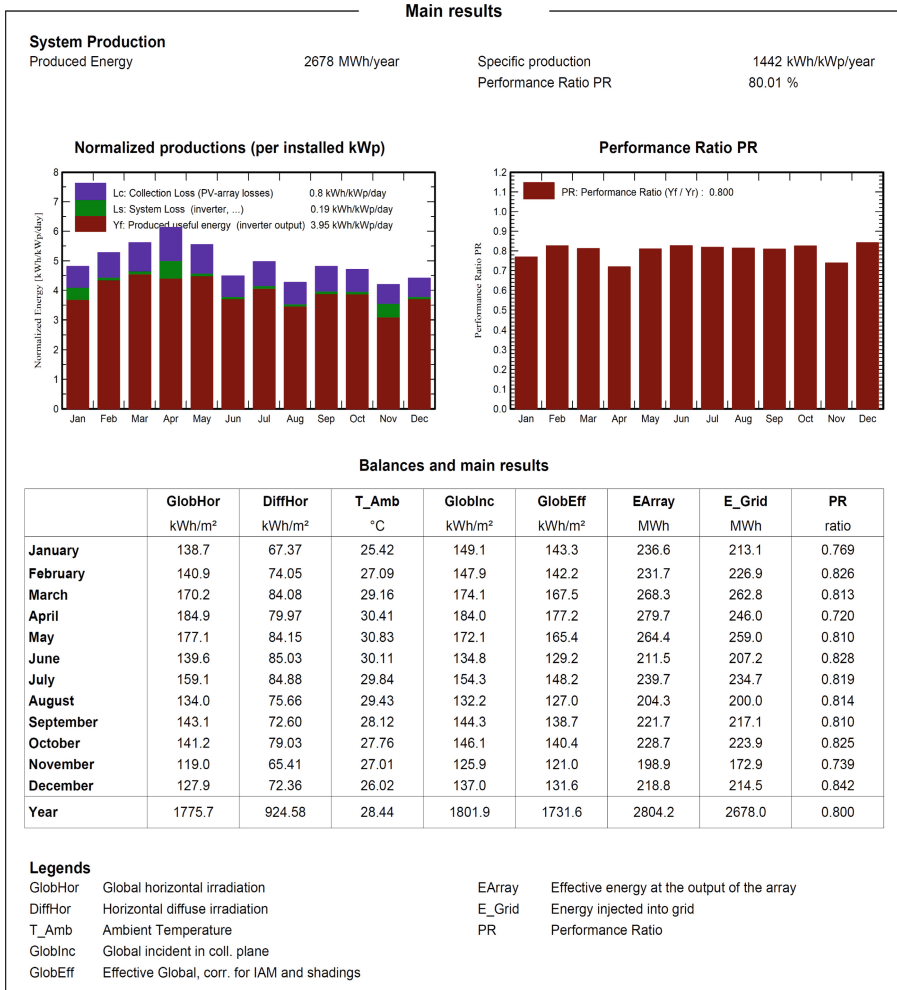
Fig. 3. Simulation results of 1.85 MWp grid-connected solar rooftop PV power generation by PVsyst version 7.2.

3.3   Economic Feasibility

Table 3 shows the details of electricity generation for 25-year operation of solar rooftop PV power generation system. The produced energy was used to estimate the 25-year electricity generation by considering the degradation rate of the PV modules from the specification sheet, which were 2% in the first-year operation and 0.55% for 2-to 25-year operation.
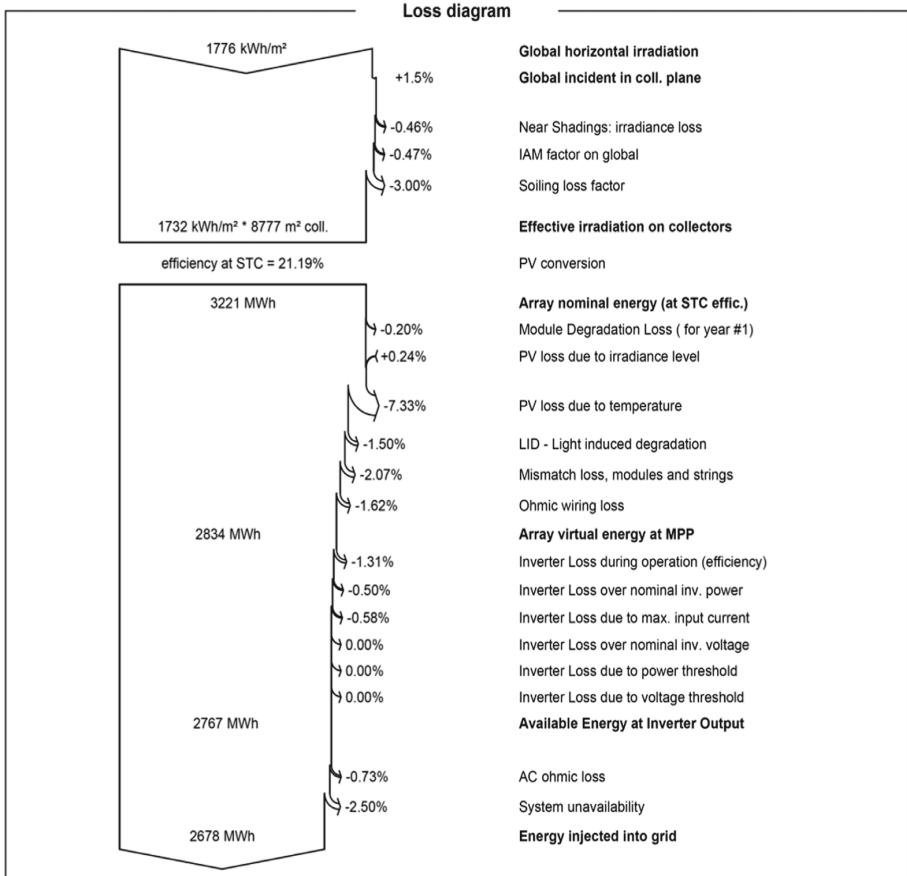
Fig. 4. Loss diagram of 1.85 MWp grid-connected solar rooftop PV power generation by PVsyst version 7.2.

The estimated total initial investment cost was about 1,452,158 USD, mainly for the equipment and the installation cost of the solar rooftop PV power generation system. The energy cost saving in Table 3 was obtained from the calculation of annual electricity generation with the peak and off-peak energy charges. The electricity tariff, which is determined by the Provincial Electricity Authority (PEA), refers to the time of use rate (TOU) in medium general service at the voltage level of 69 kV and over [18]. In the first year, the produced energy of 2,678,659 kWh resulted in energy cost saving of 269,317 USD. Total expenses from year 1 to year 25 accounted for operating and maintenance costs, insurance, utilities, depreciation cost, interests, etc. The economic analysis showed that the PB, NPV, and IRR were 6.37 years, 1,062,430 USD, and 15%, respectively.

Table 3. Economic analysis for 25-year operation of solar rooftop PV power generation system.

Year	Produced energy (kWh)	Energy cost saving (USD)	Total expense (USD)	Net cash flow (USD)	Balance (USD)
0	0	0	0	−1,452,158	−1,452,158
1	2,678,659	269,317	34,089	235,228	−1,216,929
2	2,610,353	265,074	34,231	230,843	−986,087
3	2,595,621	266,214	35,451	230,762	−755,324
4	2,580,888	267,350	36,671	230,678	−524,646
5	2,566,156	268,482	37,891	230,590	−294,056
6	2,551,423	269,610	54,481	215,129	−78,927
7	2,536,690	270,734	55,701	215,033	136,106
8	2,521,958	271,853	56,921	214,932	351,038
9	2,507,225	272,967	58,140	214,827	565,865
10	2,492,492	274,077	59,360	214,717	780,582
11	2,477,760	275,182	61,348	213,834	994,416
12	2,463,027	276,281	61,551	214,730	1,209,146
13	2,448,295	277,374	61,753	215,621	1,424,767
14	2,433,562	278,462	61,956	216,507	1,641,274
15	2,418,829	279,544	62,158	217,386	1,858,660
16	2,404,097	280,620	63,167	217,453	2,076,113
17	2,389,364	281,689	63,369	218,320	2,294,433
18	2,374,631	282,752	63,571	219,181	2,513,615
19	2,359,899	283,808	63,772	220,036	2,733,650
20	2,345,166	284,856	63,973	220,883	2,954,533
21	2,330,434	285,898	65,021	220,876	3,175,410
22	2,315,701	286,931	65,222	221,709	3,397,119
23	2,300,968	287,957	65,422	222,534	3,619,653
24	2,286,236	288,974	65,622	223,352	3,843,005
25	2,271,503	289,983	65,822	224,161	4,067,166

Note: As of 2021, 1 USD = 31.98 THB

4 Conclusions

The installation of 1.85 MWp solar rooftop PV power generation system at the commercial building in this study is technical and economic approved. Using solar energy is sustained for energy efficiency. In the first year, the project achieved energy production of 2,678 MWh resulting in energy cost saving of 269,317 USD. The PB, NPV, and IRR were 6.37 years, 1,062,430 USD, and 15%, respectively. To obtain the electricity sufficiently

to the maximum electricity of 4.9 MWp required in 2020, the installation of additional solar PV power generation system will be done. However, the wastes from end-of-life solar panels should be concerned in terms of the recovery of valuable materials and economic analysis.

References

1. Department of Alternative Energy Development and Efficiency (DEDE): Alternative energy development plan 2018–2037 (AEDP2018) (2020). (In Thai)
2. Department of Alternative Energy Development and Efficiency (DEDE).: Thailand alternative energy situation 2020 report. DEDE, Bangkok (2020)
3. Singh, G.K.: Solar power generation by PV (photovoltaic) technology: a review. Energy **53**, 1–13 (2013)
4. Gorjian, S., Shukla, A.: Photovoltaic solar energy conversion: technologies, applications and environmental impacts. Academic Press, London (2020)
5. International Renewable Energy Agency (IRENA): Future of solar photovoltaic: deployment, investment, technology, grid integration and socio-economic aspects (a global energy transformation: paper). IRENA, Abu Dhabi (2019)
6. Chaianong, A., Pharino, C.: Outlook and challenges for promoting solar photovoltaic rooftops in Thailand. Renew. Sustain. Energy Rev. **48**, 356–372 (2015)
7. Tongsopit, S.: Thailand's feed-in tariff for residential rooftop solar PV systems: progress so far. Energy Sustain. Dev. **29**, 127–134 (2015)
8. Chimres, N., Wongwises, S.: Critical review of the current status of solar energy in Thailand. Renew. Sustain. Energy Rev. **58**, 198–207 (2016)
9. Tongsopit, S., Moungchareon, S., Aksornkij, A., Potisat, T.: Business models and financing options for a rapid scale-up of rooftop solar power systems in Thailand. Energy Policy **95**, 447–457 (2016)
10. Tantisattayakul, T., Kanchanapiya, P.: Financial measures for promoting residential rooftop photovoltaics under a feed-in tariff framework in Thailand. Energy Policy **109**, 260–269 (2017)
11. Eskew, J., Ratledge, M., Wallace, M., Gheewala, S.H., Rakkwamsuk, P.: An environmental life cycle assessment of rooftop solar in Bangkok. Thailand. Renew. Energy **123**, 781–792 (2018)
12. Chaianong, A., Tongsopit, S., Bangviwat, A., Menke, C.: Bill saving analysis of rooftop PV customers and policy implications for Thailand. Renew. Energy **131**, 422–434 (2019)
13. Tongsopit, S., Junlakarn, S., Wibulpolprasert, W., Chaianong, A., Kokchang, P., Hoang, N.V.: The economics of solar PV self-consumption in Thailand. Renew. Energy **138**, 395–408 (2019)
14. Narkwatchara, P., Ratanatamskul, C., Chandrachai, A.: Performance analysis of electricity generation from grid-connected photovoltaic system using all-sky index for smart city projects in Thailand. Renew. Energy **171**, 315–327 (2021)
15. PVsyst Homepage. https://www.pvsyst.com/help/general_descr.htm. Accessed 2 May 2022
16. Bank of Thailand (BOT) Homepage. https://www.bot.or.th/Thai/FIPCS/Documents/FPG/2562/ThaiPDF/25620216.pdf. Accessed 20 May 2022. (In Thai)

17. Department of Alternative Energy Development and Efficiency (DEDE) Homepage, https:// www.dede.go.th/ewt_dl_link.php?nid=55493&filename=solar_intensity. Accessed 20 May 2022 (In Thai)
18. Provincial Electricity Authority (PEA) Homepage. https://www.pea.co.th/Portals/_default/ Documents/Rate2015.pdf. Accessed 20 May 2022

A Perspective on the Influencing Factors in the Use of Antioxidants for Biodiesel Oxidation Stability Enhancement

Chi Hou Lau[1], Suyin Gan[1(✉)], Harrison Lik Nang Lau[2], Lai Yee Lee[1], and Suchithra Thangalazhy-Gopakumar[1]

[1] Faculty of Science and Engineering, University of Nottingham Malaysia, Jalan Broga, 43500 Semenyih, Selangor Darul Ehsan, Malaysia
suyin.gan@nottingham.edu.my
[2] Malaysian Palm Oil Board (MPOB), No. 6, Persiaran Institusi, Bandar Baru Bangi, 43000 Kajang, Selangor Darul Ehsan, Malaysia

Abstract. Biodiesel is a renewable alternative to diesel which is used in transportation and industrial sectors. However, it is more susceptible to oxidation compared to diesel hence the use of antioxidants is proposed to enhance its oxidation stability. This paper aims to provide a concise perspective on the influencing factors in the use of commonly reported antioxidants for biodiesel oxidation stability enhancement. The scope here covers the type of antioxidant, concentration of antioxidant, biodiesel blend, storage time and temperature, with focus on the implications on palm biodiesel oxidation stability over an extended period. Data analysis suggests the order of effectiveness of synthetic antioxidants to be TBHQ > PY > PG > BHT $\geq$ BHA while for natural antioxidants, the order is quercetin $\geq$ curcumin > α-tocopherol. A higher applied antioxidant concentration generally results in higher IP extension though the relationship is not directly proportional. Further work can investigate the threshold of antioxidation activity with increasing concentration. Increasing the blend ratio enable the possibility of reducing antioxidant cost, but this would not be a major influencing factor unless the practice of adding antioxidant first prior to blending changes. The storage time is a major influencing factor in the context of stored biodiesel used as a backup energy source. At least 6 months to 1 year is recommended for such tests. Temperature affects the thermodynamics and kinetics of antioxidants performance. More studies on this for palm biodiesel are recommended for comparison and elucidation of the underlying mechanisms.

Keywords: Antioxidant · Biodiesel · Oxidation stability · Storage stability

1 Introduction

Worldwide, the use of non-renewable fossil fuels like diesel has resulted in environmental pollution and serious health impacts. As such, alternative fuels such as biodiesel has been developed, researched, and adopted in transportation cum industrial sectors.

Biodiesel made up of fatty acid methyl esters (FAME) originates from vegetable oils and animal fats. It has characteristics such as better degradability, higher flashpoint, negligible sulphur content and good lubricity compared to diesel [1]. Biodiesel combustion results in reduced carbon monoxide, particulate matter and unburnt hydrocarbons, but higher nitrogen oxides (NO_x) [2]. Nevertheless, biodiesel is more prone to oxidative degradation due to their unsaturated and polyunsaturated FAME [3]. This in turn poses difficulties in the storage of biodiesel and its wide-scale application as a renewable fuel [4]. To increase the oxidation stability of biodiesel during storage, an antioxidant can be added to delay the oxidation process that occurs naturally through exposure to air, metal and light [5].

The effects of synthetic antioxidants such as tert-butylhydroquinone (TBHQ), butylated hydroxytoluene (BHT), butylated hydroxyanisol (BHA), pyrogallol (PY) and propyl gallate (PG) in biodiesel have been extensively studied [6–18]. Natural antioxidants such as α-tocopherol, curcumin and quercetin have also been proposed as safer antioxidant alternatives [6, 10, 12, 16, 19–22]. When assessing the oxidation stability of biodiesel, the induction period (IP) in hours is typically measured. A higher IP value would be interpreted as the biodiesel lasting longer before it oxidises to an unacceptable level. The minimum biodiesel oxidation stability measured in IP is 3 h and 8 h for the ASTM D6751 and the EN 14214 standards, respectively.

With the rise in research on antioxidants in biodiesel over the years, this review aims to provide a concise perspective on the influencing factors in the use of commonly reported antioxidants for biodiesel oxidation stability enhancement. The scope of work discussed here covers the type of antioxidant, concentration of antioxidant, biodiesel blend, storage time and temperature. The novelty of this review lies in providing a fresh interpretation of the reported data with palm biodiesel in mind, for which limited studies exist. More specifically, the implications of the reported data in view of the fuel oxidation stability over an extended period as backup energy source is of interest here. Finally, this review also aims to identify future research directions based on the status of development in this area.

2 Type of Antioxidant

Among the most widely studied synthetic antioxidants over the past two decades, tert-butylhydroquinone (TBHQ) has constantly showed high antioxidation activities on different biodiesel types. This is evident from Table 1 which compiles the IP increments measured when TBHQ is added to different biodiesel fuels. For instance, in [6], TBHQ at 100 pm was already found to be effective in increasing the IP value of distilled palm oil methyl ester (DPOME) to above 8 h, the limit specified in the EN14214 standard. At 500 ppm, the antioxidant raised the IP even further to 26.68 h. The data aligns with the results obtained for beef tallow [15], where 5000 ppm of TBHQ was able to achieve a 9-fold increase in the standard IP value. Interestingly, the findings reported in [8] for waste cooking oil methyl ester (WCOME) showed a similar trend to that for DPOME whereby the increments of IP at 100 ppm and 500 ppm for both biodiesels were noticeably close.

When comparing the results of [6] and [8] for butylated hydroxytoluene (BHT) as shown in Table 2, it appears that BHT is more effective in enhancing the IP value for

DPOME compared to WCOME. Nevertheless, the trends of increment are still similar, and it might be possible to predict the IP outcomes by the difference between the increment rates for both antioxidants for higher concentrations, say 2000 ppm. Additionally, comparing Tables 1 and 2, TBHQ outperforms BHT in terms of antioxidation potential in the context of DPOME, as TBHQ requires as little as 100 ppm to achieve the minimum of 8 h IP value as required by the EN14214 standard. Here, it is hypothesised that BHT performs better in methyl esters with higher unsaturated fatty acid percentage based on the data for [6] and [8] since the reported C18:2 for [8] is 27.78% compared to 10.25% for [6]. The application of BHT in used cooking oil methyl ester (UCOME) in [12] resulted in the IP values increasing by 7 and 10 h at 300 and 600 ppm, respectively, corresponding to having 83.9% unsaturated C18 fatty acids combined. Their base IP value was also very stable, which was 8 h without any addition of antioxidants. For most of the biodiesels listed in Tables 1 and 2, the use of BHT is not as effective as TBHQ. Furthermore, a decline in the IP value was noted when BHT was dosed at 1000 to 1500 ppm in *C. inophyllum* biodiesel [17].

From Table 3, the performance of butylated hydroxyanisole (BHA) is similar to BHT. It is seen that BHA underperforms compared to BHT in both rapeseed methyl ester (RME) and soybean methyl ester (SME) [18]. The same observations for SME are shown in [16], even though the differences between the IP increase for both antioxidants at multiple concentrations are insignificant. Out of all the studies listed in Table 3, only 500 ppm in RME and 600 ppm SME [18], 500 ppm and above in WCOME [8], and 1000 ppm in Karanja oil methyl ester (KOME) [11] are above the limit of 8 h IP value.

There are fewer studies using propyl gallate (PG) and pyrogallol (PY) in biodiesels compared to TBHQ, BHT and BHA as the latter three antioxidants are cheaper and generally demonstrate high antioxidation capabilities. Even so, the compilation of data from multiple studies listed in Tables 4 and 5 show that both PG and PY have comparable, if not stronger effects, than that of TBHQ in Table 1. It is important to note that all the biodiesels listed in Tables 4 and 5 have high percentages of C18:1 and C18:2, with Camelina biodiesel (CBD) having the highest C18:3 (33.5%) [14]. PG in WCOME was less effective compared to TBHQ while PY surpassed TBHQ. Similar findings were reported for KOME where PG and PY were more effective than TBHQ [11]. Meanwhile, it was also reported that PY was the better antioxidant followed by TBHQ and PG for SME [10]. It is possible that PG and PY perform better in fuels with higher unsaturated fatty acid contents, but further studies are warranted to fully understand the relationship between the extension of IP and fatty acid composition. Another interesting thing to note is that while KOME in study [13] showed a similar trend in terms of the ranking of antioxidants, all antioxidants used performed poorly at the same concentrations as compared to study [11]. The former reported 13.57% of C18 present in their fuel. There might be a relationship between the saturation level of FAME with the performance of antioxidants.

For natural antioxidants, α-tocopherol or vitamin E is found predominantly in plant-based feedstock. It is not as widely studied as an alternative to current biodiesel additives due to its high cost. As seen in Table 6, 3000 ppm of α-tocopherol can increase the IP value to 11 h for DPOME [6]. Based on the IP increment value from 1000 ppm to 3000 ppm, it is estimated that at least 2000 ppm is required to ensure the stability of

DPOME. Conversely, [10] and [16] discussed the ineffectiveness of α-tocopherol in SME, whereby 250 ppm was only able to increase the IP value by 0.10 h. Furthermore, there were also other studies that showed α-tocopherol was incapable of protecting the fuel from oxidation.

Meanwhile, curcumin is more widely studied as compared to α-tocopherol. Different from α-tocopherol, the antioxidation potential of curcurmin in UCOME [12] and SME [20] showed promising results even at low concentrations. At 500 ppm, curcumin was able to boost the IP of cottonseed methyl ester (CSME) to 7.9 h [21]. Although in this study the exact composition of CSME was not reported, it was stated that the fuel contained high unsaturated fatty acid chains. The results based on [12] and [20] showed that while the IP increases were lesser than those of synthetic antioxidants, curcumin is still considered as an effective natural-based antioxidant.

Comparing the performance of curcumin and quercetin in [21], it is noted that both antioxidants showed the same increment in IP value at 500 ppm. This alone proved that quercetin is another antioxidant that has stronger antioxidation capability compared to α-tocopherol. Additionally, quercetin also performed better than curcumin when dosed into biodiesel at a higher concentration. At 3000 ppm, the final IP value of CSME was exactly 16 h, which was doubled the standard requirement. Another study by [22] also showed that quercetin performed equally well as curcumin in SME.

Table 1. IP increment for TBHQ.

Biodiesel (Base IP, h)	Antioxidant concentration (ppm)	IP increment (h)	Reference
Distilled palm oil (3.52 h)	50, 100, 500	5.32, 8.58, 26.68	[6]
Safflower oil (1.70 h)	100, 250, 500, 750, 1000	0.40, 1.70, 2.70, 4.25, 7.30	[7]
Waste cooking oil (3.01 h)	100, 250, 500, 750, 1000	9.35, 19.29, 30.44, 33.81, 48.11	[8]
Sunflower oil (0.75 h)	200, 500, 1000, 2000, 2500	0.33, 0.88, 2.36, 10.68, 23.82	[9]
Soybean oil (3.60 h)	250, 500, 1000	1.20, 3.20, 7.40	[10]
Karanja oil (1.82 h)	300, 500, 700, 1000	1.67, 1.78, 2.14, 3.82	[11]
Used cooking oil (8 h)	300, 600, 1000	3.50, 8.00, 10.50	[12]
Karanja oil (0.33 h)	500, 1000, 2000, 3000	0.55, 1.21, 2.58, 5.86	[13]
Camelina oil (2.30 h)	500, 1000, 3000	3.20, 6.50, 19.00	[14]
Beef tallow (0.55 h)	5000	73.65	[15]

Table 2. IP increment for BHT.

Biodiesel (Base IP, h)	Antioxidant concentration (ppm)	IP increment (h)	Reference
Distilled palm oil (3.52 h)	50, 100, 500, 1000	2.65, 4.23, 9.58, 13.08	[6]
Waste cooking oil (3.01 h)	100, 250, 500, 750, 1000	1.51, 3.26, 5.28, 6.62, 7.82	[8]
Sunflower oil (0.75 h)	200, 500, 1000, 2000, 2500	0.53, 1.36, 2.23, 3.69, 4.34	[9]
Soybean oil (3.60 h)	250, 500, 1000	0.60, 1.40, 2.80	[10]
Karanja oil (1.82 h)	300, 500, 700, 1000	1.82, 2.05, 2.73, 4.08	[11]
Used cooking oil (8 h)	300, 600, 1000	7.00, 10.00, 19.50	[12]
Karanja oil (0.33 h)	500, 1000, 2000, 3000	0.47, 1.43, 2.81, 4.55	[13]
Camelina oil (2.30 h)	1000, 2000, 3000	4.60, 6.00, 19.00	[14]
Beef tallow (0.55 h)	5000	83.73	[15]
Soybean oil (2.80 h)	500, 1000, 1500, 2000	1.50, 2.00, 3.20, 3.40	[16]
C. inophyllum (8.47 h)	375, 750, 1000, 1125, 1500	15.37, 15.43, 19.51, 18.45, 17.98	[17]
Rapeseed oil (5 h)	453	3.00	[18]
Soybean oil (5 h)	568	3.00	[18]

Table 3. IP increment for BHA.

Biodiesel (Base IP, h)	Antioxidant concentration (ppm)	IP increment (h)	Reference
Safflower oil (1.70 h)	100, 250, 500, 750, 1000	0.40, 0.80, 2.50, 3.30, 4.20	[7]
Waste cooking oil (3.01 h)	100, 250, 500, 750, 1000	1.93, 4.23, 6.17, 7.22, 8.09	[8]
Soybean oil (3.60 h)	250, 500, 1000	0.90, 1.80, 2.90	[10]
Karanja oil (1.82 h)	300, 500, 700, 1000	1.81, 4.50, 4.72, 6.47	[11]
Karanja oil (0.33 h)	500, 1000, 2000, 3000	0.43, 1.37, 2.63, 4.69	[13]
Camelina oil (2.30 h)	1000, 2000, 3000	2.70, 3.70, 3.20	[14]
Soybean oil (2.80 h)	500, 1000, 1500, 2000	1.30, 2.30, 3.00, 4.20	[16]
Rapeseed oil (5 h)	500	3.00	[18]
Soybean oil (5 h)	600	3.00	[18]

Table 4. IP increment for PG.

Biodiesel (Base IP, h)	Antioxidant concentration (ppm)	IP increment (h)	Reference
Waste cooking oil (3.01 h)	100, 250, 500, 750, 1000	7.06, 12.09, 16.56, 19.72, 21.50	[8]
Soybean oil (3.60 h)	250, 500, 1000	3.20, 4.90, 6.60	[10]
Karanja oil (1.82 h)	300, 500, 700, 1000	3.05, 5.89, 8.44, 11.37	[11]
Used cooking oil (8 h)	300, 600, 1000	9.50, 16.00, 22.00	[12]
Camelina oil (2.30 h)	500, 1000	5.20, 7.60	[14]

Table 5. IP increment for PY.

Biodiesel (Base IP, h)	Antioxidant concentration (ppm)	IP increment (h)	Reference
Waste cooking oil (3.01 h)	100, 250, 500, 750, 1000	13.10, 17.06, 19.69, 21.33, 22.88	[8]
Soybean oil (3.60 h)	250, 500, 1000	5.40, 7.20, 8.00	[10]
Karanja oil (1.82 h)	300, 500, 700, 1000	4.35, 12.83, 15.37, 20.67	[11]
Karanja oil (0.33 h)	500, 1000, 2000, 3000	2.53, 4.66, 24.69, 34.02	[13]

3   Concentration of Antioxidant

The concentration of antioxidants is widely studied in the literature over the past decades. Multiple types of antioxidants, synthetic and natural included, have been investigated in varying concentrations to understand the relationship between the antioxidant concentration with the IP value.

From Table 2, taking BHT as an illustrative antioxidant, it is noticeable that the IP extension generally increases with the increase in concentration of BHT. However, the IP extension is not directly proportional to the concentration increase. For instance, [16]'s results for SME showed small increase when the dose was increased from 1500 to 2000 ppm. This was further proved in [11]. The IP extension dropped from 8.48 h (from 4.35 h at 300 ppm to 12.83 h at 500 ppm) to 2.54 h (from 12.83 h at 500 ppm to 15.37 h at 700 ppm), then it further increased by 5.30 h when increased to 1000 ppm (20.67 h).

Furthermore, it is also obvious that IP values of *C. inophyllum* [17] showed a decreasing trend after 1000 ppm of BHT application. Similarly, the same trend was recorded by [14] for BHA use in Camelina biodiesel. The IP extension decreased from 3.7 h to 3.2 h when the dosage was increased from 2000 to 3000 ppm. It is noteworthy that these observations occur when the concentrations are in the order of thousands. This implies

Table 6. IP increment for α-tocopherol, curcumin and quercetin.

Biodiesel (Base IP, h)	Antioxidant	Concentration (ppm)	IP increment (h)	Reference
Distilled palm oil (3.52 h)	α-tocopherol	1000, 3000	2.90, 7.68	[6]
Soybean oil (3.60 h)	α-tocopherol	250, 500, 1000	0.10, 0.30, 0.40	[10]
Soybean oil (2.80 h)	α-tocopherol	500, 1000, 1500, 2000	0.30, 0.70, 1.20, 1.60	[16]
Used cooking oil (8 h)	curcumin	300, 600, 1000	5.50, 9.50, 15.00	[12]
Soybean (2.97 h)	curcumin	500, 1000, 2000, 5000	0.47, 0.91, 1.53, 2.62	[19]
Soybean with bovine tallow (8.79 h)	curcumin	500, 1000, 2000, 5000	1.23, 1.44, 2.00, 3.42	[19]
Soybean (4.97 h)	curcumin	500, 1000, 1500	1.38, 3.06, 4.14	[20]
Cottonseed oil (4.70 h)	curcumin	500, 1000, 2000, 3000	3.20, 4.20, 7.30, 7.50	[21]
Cottonseed oil (4.70 h)	quercetin	500, 1000, 2000, 3000	3.20, 5.30, 10.10, 11.30	[21]
Soybean oil (3.77 h)	quercetin	3000	8.29	[22]

there might be a maximum limit of activity whereby when the antioxidants dosage has reached a certain threshold, it is no longer effective to protect the fuel. Furthermore, there might also be some reactions yet to be understood at this current stage of research and development.

Most studies on antioxidants concentration conclude with the concentration needed for the biodiesel to meet the required standard while evaluating and comparing different antioxidants to see which has the best performance. This would be sufficient for biodiesel that is distributed quickly to the end-users such as petrol stations. However, for ensuring long-term fuel stability for use in backup generators, it would be preferable to screen the type of antioxidants first at a fixed concentration considering the large differences seen and discussed in Sect. 2.

4 Biodiesel Blend

In industrial practice, after B100 production, the antioxidant is added into the fuel prior to further processing to biodiesel blends such as B7 to B20. It is particularly important to add the antioxidant as soon as possible since biodiesel oxidises as soon as it is produced.

The results adapted from [23] as presented in Table 7 show a drastic change in biodiesel oxidative stability when raw B100 is blended to B5, B7 and B10. Significantly, even without the presence of antioxidants, the IP values are at least 15 h, which is way higher than the EN14214 standard limit of 8 h. In the Malaysian context, the minimum

IP value for palm B100 without antioxidants is at least 10 h. If the same formula is applied to palm B100, its IP value might hit at least 30 h even without any antioxidants added. The main reason why it is important to raise the initial IP so high is because it will gradually drop as time passes. The high initial IP ensures high stability even after long storage period. Interestingly, the IP values do not increase at 200 ppm and 300 ppm of BHT in both B5 and B10 mixed methyl ester (MME). As previously discussed, there might be a limit in the antioxidant capability in the fuel as the fatty acid compositions for rapeseed methyl ester (RME) and MME used were quite similar, with less than 2% differences in C16, C18:1 and C18:2.

The stability of biodiesel blends dosed with antioxidants increases not only with increased concentration of antioxidants but also with higher percentage of blended diesel. However, TBHQ was reportedly less effective compared to BHT and BHA when B100 Jatropha methyl ester (JME) was blended to B50 [24]. While the authors discussed the possibility of hydrocarbons hindering the polar phenol groups of BHT and BHA, the reasoning behind TBHQ being less effective in these blends was not reported. From Fig. 1 [25], both B7 and B20 at t = 0 showed similar ranking of antioxidant capabilities as those of [24] though it remains to be elucidated why TBHQ is less effective when blended down in the latter while there are no changes to the former. This makes the study of antioxidants under different biodiesel blends worth to be explored. The possibility of reducing antioxidant cost is enabled by increasing the blend ratio. Nevertheless, unless the norm of adding antioxidants first prior to blending is changed, it would not be considered a major influencing factor.

Table 7. IP values of biodiesel blends from rapeseed oil (RME) and mixed oil (MME) (used cooking oil and rapeseed oil, 20:80 ratio) with varying BHT concentrations. Adapted from [23].

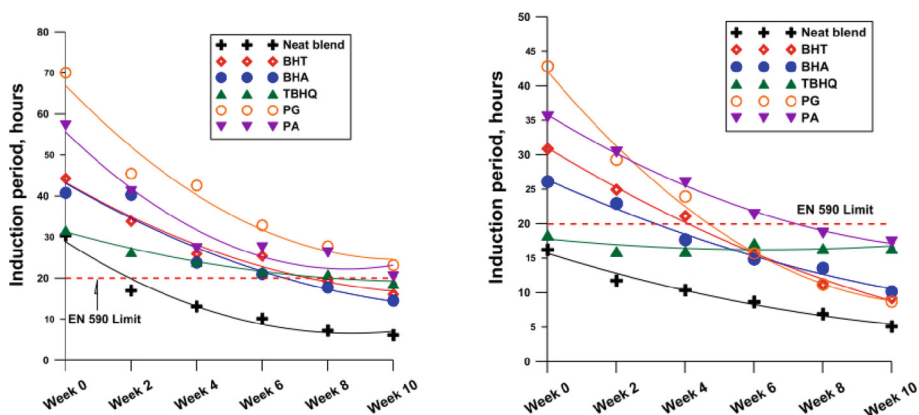| Biodiesel	IP value (h) at varying concentrations			
	0 ppm	100 ppm	200 ppm	300 ppm
B5 (RME)	19	31	39	47
B7 (RME)	19	28	36	41
B10 (RME)	15	22	28	33
B100 (RME)	1	2	3	3
B5 (MME)	17	40	44	43
B7 (MME)	20	34	42	45
B10 (MME)	18	31	36	36
B100 (MME)	1	1	2	2

Fig. 1. IP value of B7 (left) and B20 (right) commercial biodiesel dosed with 1000 ppm antioxidants over 10 weeks [25].

5 Storage Time

This is arguably the best parameter if the concern behind the experimental programme is the fuel stability over a longer period such as reservoir tanks for backup generators. Investigating the protection offered by antioxidants over a period allows researchers to understand the rate of depletion of these antioxidants and enable the estimation of how long it takes before the biodiesel becomes fully oxidised. During oxidation, the
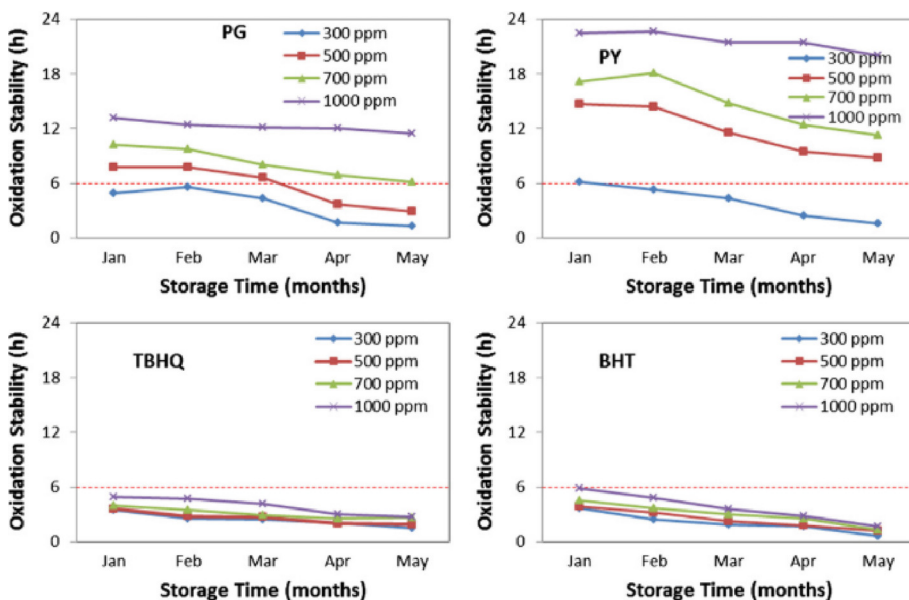
Fig. 2. IP trends for KOME dosed with PG, PY, TBHQ and BHT over 4 months of storage time. Adapted from [11].

antioxidants work as a layer of protection for the fuel by acting as a chain inhibitor, an oxygen quencher, or a reducing agent. As such, these antioxidants burn out themselves before the initiation of oxidation occurs on the biodiesel.

The tested storage times of biodiesel are usually more than 4 months [10, 11, 13, 20, 25, 26]. Even so, it is uncertain that the change in IP is significant enough to conclude that IP decreases over storage time. From Fig. 1 [25], BHA in B7 for the first two weeks barely has any change in the IP value though there is an overall decreasing trend over 10 weeks. Similarly, in Fig. 2 [11], 500 ppm of PG and PY show little to no change to the IP value after 1 month whereas 300 ppm of PG and 700 ppm of PY show increased IP values.

Figure 3 [26] also show a decreasing trend with a few notable outliers. The stability of B20 prepared from B100 D with 6 h initial IP increased over time for the hydrocracked diesel blended in the fuel. Meanwhile, fluctuating trends are seen between weeks 17 to 27 for the hydrotreated diesel version. Fluctuating trends are also observed for C-6 h and D-3 h for hydrocracked fuels, which might be due to uncontrollable conditions at those times though there were no plausible reasonings reported.
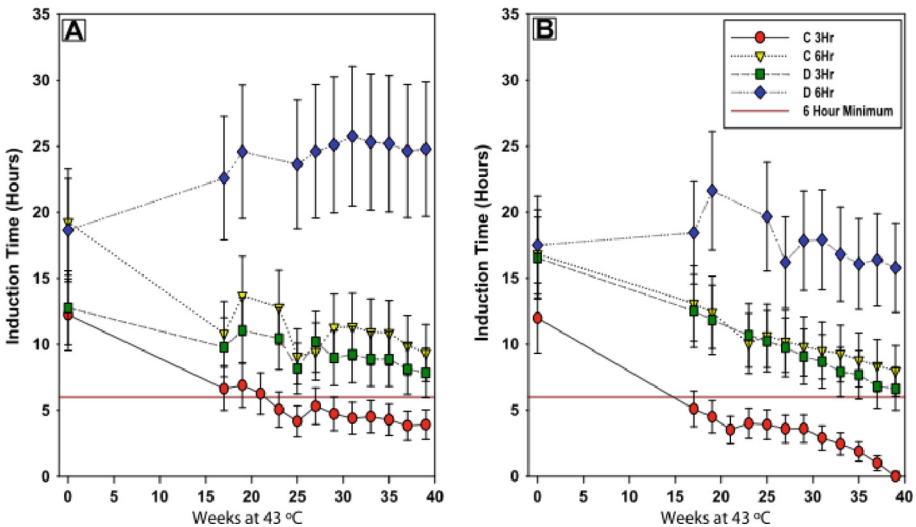
Fig. 3. IP trends of B20 blended from B100 with 3 and 6 h initial IP over 40 weeks of storage. (A: hydrocracked diesel, B: hydrotreated diesel) [26].

Overall, the study of antioxidants over an extended period allows researchers to understand the progression of antioxidants consumption to protect the biodiesel from oxidation. The ability to know how long a known concentration of a particular antioxidant can protect a fuel is a step needed to maximise the usage of antioxidants while reducing cost of adding antioxidant. A timeframe below 4 months would appear to be less than ideal as it might not fully project the processes occurring within the fuel. Whilst it is better if a fuel is stored longer for testing, there is also a risk of the fuel completely oxidising before that timeframe, leading to stagnant IP results. Thus, at least 6 months

to 1 year of storage is recommended when doing such tests. Additionally, it will be useful to include periodic measurements of the antioxidant concentration to ascertain the temporal consumption. Similarly, testing the fatty acid methyl ester compositions at the initial and final points for more in-depth analysis is recommended. Nevertheless, a point of consideration here is that results might vary due to changing ambient storage conditions, e.g., temperature and weather. Hence, it is important to keep these constant, or near constant as much as possible. In summary, storage time is a key influencing factor when it comes to evaluating the effects of antioxidants in stored biodiesel used as a backup energy source.

6 Temperature

The influencing factor of temperature is typically studied in conjunction with thermodynamics and kinetics studies. Temperature dependent oxidation tests are carried out to obtain the necessary data for calculation of fundamental thermodynamics and kinetics parameters. For thermodynamics parameters, the enthalpy ($\Delta H^{\ddagger}$) value indicates the heat change during the reaction while the entropy ($\Delta S^{\ddagger}$) value determines the spontaneity of the reaction. A positive $\Delta H^{\ddagger}$ value means that the reaction is endothermic while a positive $\Delta S^{\ddagger}$ indicates that the reaction is spontaneous. Meanwhile, the Gibbs free energy ($\Delta G^{\ddagger}$) corresponds to the total amount of work done in the system when temperature and pressure is kept constant. In terms of kinetics, parameters such as the reaction constant (k) and activation energy (E_a) are determined.

The IP of B100 samples was affected by temperature whereby an IP decrease corresponded to an increase in temperature of the Rancimat oxidation test [27]. This implies that the k value increases as the temperature increases, which can be viewed as the antioxidant consumption rate increasing as the temperature increases [28, 29].

The evaluation of thermodynamics and kinetics of antioxidants enables detailed fundamental understanding of how the antioxidants work in biodiesel. It also allows the mechanism of antioxidation in biodiesel to be elucidated though these would be unnecessary if the objective is merely to obtain an antioxidant sufficiently effective to produce biodiesel meeting the oxidation stability standards. Currently, there is a lack of overall studies on this topic and studies which focus on comparing and interpreting the varying results obtained for different antioxidants and biodiesel fuels. Hence, this could be a potential future research direction.

7 Conclusion and Future Research Direction

To date, is a lack of studies on comprehensive palm biodiesel oxidation stability evaluation with various antioxidants. A notable study on antioxidants in palm biodiesel was carried out by [6]. Significantly, for palm biodiesel, the antioxidant research would be focussing on DPOME, which has been stripped of its natural carotenes and vitamin E (tocopherol variants) since its IP has been reported as below the minimum requirement of the EN14214 standard at 3.52 h, unlike crude palm oil methyl ester at 25.70 h [6]. Such high stability of palm biodiesel is attributed to the fatty acid composition of palm oil since palm oil methyl ester has high C16 and C18:1 content as compared to other oils

such as camelina, Karanja and safflower [7, 11, 14]. Likewise, high stability is accorded to RME [18], where C18 and C18:1 are the dominant fatty acids. The presence of such high concentration of saturated fatty acids, namely C16 and C18, contributes significant fuel stability. The amount of different C18 unsaturated fatty acids also impacts the oxidation stability. Fuels with a higher content of C18:1 will have a higher stability compared to fuels with higher content of C18:2 and C18:3.

Considering the saturation of FAME in DPOME and the compiled data in Table 1 till Table 5, it is suggested that the order of effectiveness of the five commonly used synthetic antioxidants would be TBHQ > PY > PG > BHT ≥ BHA for DPOME. For natural antioxidants, it is hypothesised that the effectiveness would be in the order of quercetin ≥ curcumin > α-tocopherol. To the best knowledge of the authors, there are no studies to date on the use of curcumin and quercetin in palm biodiesel.

Generally, a higher applied antioxidant concentration results in higher IP extension though the relationship does not appear to be directly proportional. An area yet to be explored is the threshold of antioxidation activity with increasing concentration. For ensuring long-term palm biodiesel stability for use in backup generators, it would be preferable to screen the type of antioxidants first at a fixed concentration.

The stability of biodiesel blends dosed with antioxidants increases not only with increased concentration of antioxidants but also with higher percentage of blended diesel. Nonetheless, unless the norm of adding antioxidants prior to blending is changed, it would not be considered a major influencing factor.

The storage time is a major influencing factor for stored biodiesel used as a backup energy source. At least 6 months to 1 year of storage is recommended when doing such tests for palm biodiesel. Additionally, it will be useful to include periodic measurements of the antioxidant concentration to ascertain the temporal consumption and to test the FAME compositions at the initial and final points for more in-depth analysis. Bearing in mind ambient storage conditions vary, it is important to keep these constant, or near constant as much as possible.

Finally, temperature affects the thermodynamics and kinetics of antioxidants in biodiesel. Future work can focus on this aspect for palm biodiesel for comparison with other fuels considering the limited reported studies. From this, fundamental understanding of mechanism and how the antioxidants work in biodiesel can be gained.

References

1. Knothe, G., Razon, L.F.: Biodiesel fuels. Prog. Energy Combust. Sci. **58**, 36–59 (2017)
2. Xue, J., Grift, T.E., Hansen, A.C.: Effect of biodiesel on engine performances and emissions. Renew. Sustain. Energy Rev. **15**, 1098–1116 (2011)
3. Lapuerta, M., Rodríguez-Fernández, J., Ramos, A., Álvarez, B.: Effect of the test temperature and anti-oxidant addition on the oxidation stability of commercial biodiesel fuels. Fuel **93**, 391–396 (2012)

4. Mantovani, A.C.G., Chendynski, L.T., Santana, V.T., Borsato, D., Di Mauro, E.: Influence of antioxidants in biodiesel degradation: electronic paramagnetic resonance tracking of free radicals. Fuel **287**, 119531 (2021)

5. Goh, B.H.H., Chong, C.T., Ong, H.C., Milano, J., Shamsuddin, A.H., Lee, X.J., et al.: Strategies for fuel property enhancement for second-generation multi-feedstock biodiesel. Fuel **315**, 123178 (2022)

6. Yung, C.L., Choo, Y.M., Cheng, S.F., Ma, A.N., Chuah, C.H., Basiron, Y.: The effect of natural and synthetic antioxidants on the oxidative stability of palm diesel. Fuel **85**, 867–870 (2006)

7. Nogales-Delgado, S., Encinar, J.M., González, J.F.: Safflower biodiesel: improvement of its oxidative stability by using BHA and TBHQ. Energies **12**(10), 1940 (2019)

8. Zhou, J., Xiong, Y., Xu, S.: Evaluation of the oxidation stability of biodiesel stabilized with antioxidants using the PetroOXY method. Fuel **184**, 808–814 (2016)

9. Tavares, M.L.A., Queiroz, N., Santos, I.M.G., Souza, A.L., Cavalcanti, E.H.S., Barros, A.K.D., et al.: Sunflower biodiesel: Use of P-DSC in the evaluation of antioxidant efficiency. J. Therm. Anal. Calorim. **106**, 575–579 (2011)

10. Tang, H., De Guzman, R.C., Ng, K.Y.S., O Salley, S.: Effect of antioxidants on the storage stability of soybean-oil-based biodiesel. Energy Fuels. **24**(3), 2028–2033 (2010)

11. Agarwal, A.K., Khurana, D.: Long-term storage oxidation stability of Karanja biodiesel with the use of antioxidants. Fuel Process. Technol. **106**, 447–452 (2013)

12. Serqueira, D.S., Pereira, J.F.S., Squissato, A.L., Rodrigues, M.A., Lima, R.C., Faria, A.M., et al.: Oxidative stability and corrosivity of biodiesel produced from residual cooking oil exposed to copper and carbon steel under simulated storage conditions: dual effect of antioxidants. Renew. Energy **164**, 1485–1495 (2021)

13. Obadiah, A., Kannan, R., Ramasubbu, A., Kumar, S.V.: Studies on the effect of antioxidants on the long-term storage and oxidation stability of *Pongamia pinnata* (L.) Pierre biodiesel. Fuel Process. Technol. **99**, 56–63 (2012)

14. Yang, J., He, Q.S., Corscadden, K., Caldwell, C.: Improvement on oxidation and storage stability of biodiesel derived from an emerging feedstock camelina. Fuel Process. Technol. **157**, 90–98 (2017)

15. Kleinberg, M.N., Rios, M.A.S., Buarque, H.L.B., Parente, M.M.V., Cavalcante, C.L., Luna, F.M.T.: Influence of synthetic and natural antioxidants on the oxidation stability of beef tallow before biodiesel production. Waste Biomass Valori. **10**, 797–803 (2019)

16. Luo, M., Zhang, R.-Y., Zheng, Z., Wang, J.-l, Ji, J.-B.: Impact of some natural derivatives on the oxidative stability of soybean oil based biodiesel. J. Brazil. Chem. Soc. **23**(2), 241–246 (2012). https://doi.org/10.1590/S0103-50532012000200008

17. MohamedShameer, P., Ramesh, K.: FTIR assessment and investigation of synthetic antioxidant on the fuel stability of *Calophyllum inophyllum* biodiesel. Fuel **209**, 411–416 (2017)

18. Canha, N., Felizardo, P., Correia, M.J.N.: Controlling the oxidative stability of biodiesel using oils or biodiesel blending or antioxidants addition. Environ. Prog. Sustain. Energy **37**, 1031–1040 (2018)

19. Santos, M.N., de Souza, E.F., Moreira Ramos, T.C.P., Cavalheiro, A.A., Fiorucci, A.R., da Silva, M.S.: Effect of curcumin natural antioxidant on oxidative stability of commercial biodiesels from different raw materials. Orbital. **11**, 239–245 (2019)

20. de Sousa, L.S., de Moura, C.V.R., de Oliveira, J.E., de Moura, E.M.: Use of natural antioxidants in soybean biodiesel. Fuel **134**, 420–428 (2014)

21. Freitas, J.P.A., França, F.R.M., Silva, M.S., Toms, R.J., Silva, G.: Cottonseed biodiesel oxidative stability in mixture with natural antioxidants. Korean J. Chem. Eng. **36**(8), 1298–1304 (2019). https://doi.org/10.1007/s11814-019-0287-x

22. de Sousa, L.S., de Moura, C.V.R., de Moura, E.M.: Action of natural antioxidants on the oxidative stability of soy biodiesel during storage. Fuel **288**, 119632 (2021)
23. Beck, A., Pölczmann, G., Eller, Z., Hancsók, J.: Investigation of the effect of detergent-dispersant additives on the oxidation stability of biodiesel, diesel fuel and their blends. Biomass Bioenergy **66**, 328–336 (2014)
24. Jain, S., Sharma, M.P.: Oxidation stability of blends of Jatropha biodiesel with diesel. Fuel **90**(10), 3014–3020 (2011)
25. Karavalakis, G., Hilari, D., Givalou, L., Karonis, K., Stournas, S.: Storage stability and ageing effect of biodiesel blends treated with different antioxidants. Energy **36**, 369–374 (2011)
26. Christensen, E., McCormick, R.L.: Long-term storage stability of biodiesel and biodiesel blends. Fuel Process. Technol. **128**, 339–348 (2014)
27. Spacino, K.R., Borsato, D., Buosi, G.M., Chendynski, L.T.: Determination of kinetic and thermodynamic parameters of the B100 biodiesel oxidation process in mixtures with natural antioxidants. Fuel Process. Technol. **137**, 366–370 (2015)
28. Xin, J., Imahara, H., Saka, S.: Kinetics on the oxidation of biodiesel stabilized with antioxidant. Fuel **88**, 282–286 (2009)
29. Zhou, J., Xiong, Y., Shi, Y.: Antioxidant consumption kinetics and shelf-life prediction for biodiesel stabilized with antioxidants using the Rancimat method. Energy Fuels **30**, 10534–10542 (2016)

Techno-Economic and Environmental Analysis of a Hybrid Renewable Energy System: Al Qurayyat City, KSA

Hazem Abdulrahim Atlam[(✉)] and Aziza I. Hussein

Effat University, Jeddah, Saudi Arabia
{haatlam,azibrahim}@effatuniversity.edu.sa

Abstract. Hybrid renewable energy systems (HRESs) are becoming more prevalent as they are viewed as economic off-grid sources of clean energy that could help reduce rural electrification and global warming problems. This paper aims to provide a techno-economic feasibility and environmental analysis of a HRES to be designed for meeting a daily load requirement of 389.4 kWh/day with a peak load of 82.71 kW, represented by the energy demand of thirty houses located in Al-Qurayyat city, Al Jouf Province, KSA. Thus, the aim of this paper coincides with the KSA's "Vision 2030" and also with the "Net Zero Plan", which promote sustainable energy solutions and net zero CO_2 emissions, respectively. Moreover, the objective is achieved by designing a HRES consisting of PV, WT, a DG, converter and lead-acid BSS after taking into account the weather and operating conditions of Al Qurayyat city, which represents the novelty of this paper. Simulation of the system is achieved by HOMER to obtain the optimum configuration. After considering six arrangements, the results reveal that the ideal arrangement is indeed the PV/WT/DG//BSS with an optimized NPC and COE of $358,616, and $0.166/kWh while attaining a RF percentage of 92.8%. An alternative configuration, consisting of PV/WT//BSS would yield a 100% RF but with a NPC of $475,374 and COE of $0.22/kWh. The technical results show that the proposed HRES produces a total annual energy of 285,750 kWh/year with the PV, WT, and DG contributing 91.2%, 5.21%, and 3.58%, correspondingly. Regarding the environmental assessment, the optimized HRES annually saves a total of 206,678 kg of greenhouse gases.

Keywords: Hybrid renewable energy system (HRES) · HOMER · KSA

1 Introduction

In 2019, the global energy demand was the highest at 581.51 exajoules and it declined to 556.63 exajoules in 2020 [1]. Hence, a 4% reduction in the global energy consumption was exhibited, marking the biggest decline since World War II [2]. Generally, there has been a gradual increase in energy consumption except for the years 2009 and 2020, due to the global financial crisis and the Covid-19 pandemic, respectively. Therefore, the shift to renewable energy sources has become increasingly desired.

1.1 Energy Components

Solar energy is to be incorporated in the HRES. Solar cells operate on the concept of the photovoltaic effect, in which the light energy absorbed from the Sun excites and raises its energy level from the lower energy valance band to the higher energy conduction band. When the solar cell is connected to an electrical circuit, the energized electrons dissipate their energy, prompting the production of voltage and current [3].

Another energy component is wind turbines, which are systems designed to convert the kinetic energy of the air particles into electrical energy [4]. The turbines are typically comprised of rotating rotor blades, that are coupled to a generator by means of a shaft and a series of gears, with the system being mounted on a tower exhibiting an elevation of at least 30 m or more in order to capture higher wind speeds [5].

Finally, a diesel generator is also considered. Simply, it is machinery that incorporates a diesel engine with an electrical generator, thereby transforming the chemical energy stored in the diesel fuel into electrical energy [6, 7].

1.2 Study Location

The selected area is in Al-Qurayyat city (near the Technical College for Boys), Al-Jouf Province, which is located at the northern region of KSA as shown in Fig. 1. Furthermore, being in the northern region and having clear skies, the city is suitable for renewable energy as it has an abundance of solar radiation and high wind speeds.

Fig. 1. Map of the desired site in Al-Qurrayat city, Al Jouf Province, KSA.

1.3 Aims and Objectives

The paper aims to provide a practical solution for sustainable energy at economic prices that goes in accordance with the Saudi 2030 Vision as well as clean energy that ties in with the Kingdom's aim to "reach net zero" by 2060. Thus, the objective is to design a HRES composed of PV, wind turbines, a diesel generator, and lead-acid battery storage system to accommodate a daily load size of 389.4 kWh/day with a peak load of 82.72 kW. The HRES is designed after considering the operating and weather conditions in Al Qurayyat city and this reflects the originality of this paper.

2   Overview of Previous Works

Studies focused on implementing new HRES designs by incorporating several combinations of energy components, while employing numerous techniques for optimization and feasibility assessment in various regions that have diverse climate conditions.

In 2016, Hegazy Rezk et al. [8] designed a HRES consisting of PV/FC/BSS with a NPC and COE of $50,000 and $0.058, respectively, to be implemented in Menya Governate, Egypt. In the same year, Mehdi Baneshi et al. [9] proposed a PV/WT/DG/BSS hybrid system to meet a load of 9,911 kWh/day in Shiraz, Iran, and provided a dual economic analysis of the system when being on-grid and off-grid. The following year, a study achieved by Rumi Rajbongshi et al. [10] analyzed a PV/BM/DG/BSS hybrid system as both an on-grid and off-grid system for a rural village in India, and then reevaluated the resulting COE of both cases after considering various peak loads, thus, concluding that high loads with low peak demands would result in lower COE. In 2019, a study done by K. Murugaperumal et al. [11], attempted to accurately compute the load of 179.32 KWh/day, for Korkadu, India, by implementing an artificial neural network feedback propagation (ANN-BP) software along with a data optimization tool known as Levenberg-Marguardt (LM) to size and design the PV/WT/BM/BSS hybrid system. Another study in 2019 conducted by Om Krishan et al. [12], for ten houses in Yamunanagar, Haryana, India, endeavored to provide a precise technical analysis of a HRES, consisting of PV/WT/BSS, using HOMER and reattempting the simulation with MATLAB, then comparing the results. Another study in 2019, done by Hai Tra Nguyen et al. [13], tried to estimate the load of a wastewater treatment plant by utilizing creative, holistic methods, and accordingly, the hybrid system subunits were accurately sized using a fuzzy-decision-making algorithm after considering a multi-objective case. In 2020, a paper accomplished by Fabio Renaldi et al. [14] aimed to design a HRES to conserve the environment and provide electricity to three remote, rural villages named Campo serio, El potrero, and Silicucho, situated in the country of Peru, each having different climate zones, with the results revealing that the PV/WT/DG/BSS is the optimized configuration for all the villages. PV/WT/DG. In 2021, a study done by Reza Esfilar et al. [15], suggested a PV/WT/BM/BSS hybrid system, in which organic and inorganic wastes from nearby neighborhoods would be used for the biomass component, to supply clean electricity and heat for the University of Victoria, Canada, reducing CO_2 emissions by 1100 tons per year at an estimated NPC of $1.8 million and a COE of $0.074/kWh. Rasikh Tariq et al. [16], optimized the HRES, composed of PV/WT/DG/BSS, for Yucatan,

Mexico, using HOMER and then compared the results with those obtained by spreadsheet algorithms, followed by a Non-Dominating Sorting Genetic Algorithm II, and a multi-criteria decision-making tool known as The Order of Preference by Similarity to Ideal Solution, to provide multi-objective optimization.

In short, solar energy is one of the most common energy subunits incorporated in HRESs because it is abundant, relatively cheap, and has mature technology. As of this writing, no hybrid system was designed for Al Qurayyat city. Hence, the originality of this works lies in designing a HRES based on the weather conditions of Al Qurayyat.

3   Proposed HRES

To design the HRES, the Hybrid Optimization of Multiple Energy Resources software (HOMER) is used. The software considers the energy economic aspects, summarized by main parameters, including the net present cost (NPC) and cost of energy (COE). The NPC is the main objective to be minimized by HOMER, executed by utilizing two optimization algorithms. The first is the Grid Search algorithm, which simulates all the feasible HRES configurations, followed by the HOMER Optimizer, which allows the selection of the configuration with the least costs.

3.1   Resource Data

The global horizontal irradiance (GHI), temperature and wind speed data for Al Qurayyat is acquired to determine if the selected site is appropriate for implementing solar and wind technologies. The results are shown in Figs. 2, 3, and 4. Overall, the data, obtained from the National Aeronautics and Space Administration (NASA), shows incredible promise in terms of both solar and wind potential.
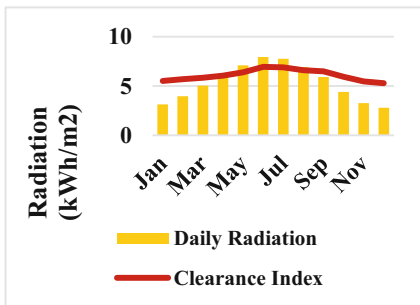
Fig. 2. Monthly average GHI.
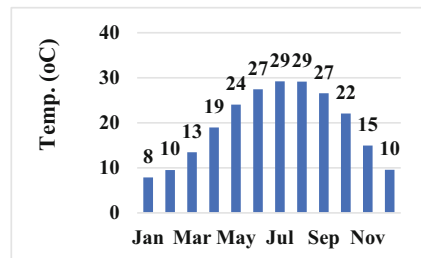
Fig. 3. Monthly average temperature.

3.2   Load Profile

The HRES is designed to supply electricity to a residential load comprised of 30 houses, estimated based on a two-bedroom household [17]. The results are displayed in Table 1
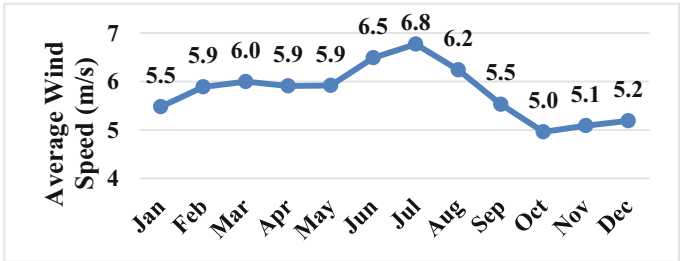
Fig. 4. Monthly average wind speed.

with the daily and monthly load distributions being illustrated in Figs. 5 and 6. A random variability of 10% was used to reflect the casual day to day variations. The load size for the system is evaluated to be 389.4 kWh/day, with a peak of 82.71 kW (considering a load factor of 0.2) [18, 19].
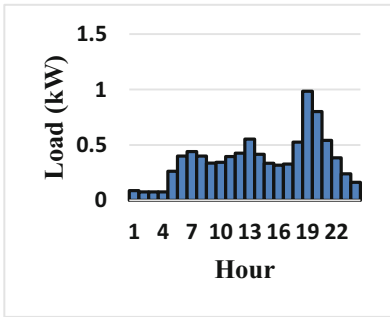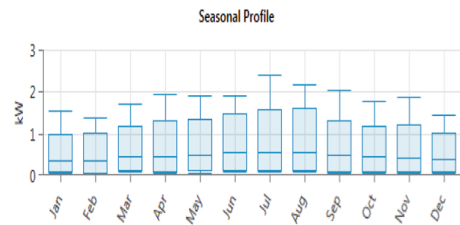

Fig. 5. Daily load distribution

Fig. 6. Monthly load profile

Table 1. Load distribution for a house

Electric Appliance	Power (W)	Quantity	Hours (h/d)	Load (Wh/day)
Refrigerator	250	1	24	6000
CFL Bulbs	15	5	8	600
Washing Machine (7kg)	500	1	1	500
Small (Window) AC	500	2	3	3000
LED TV (32")	50	1	3	150
Water Cooler	80	1	24	1920
Water Pump	250	1	3	750
Electric Kettle	600	1	0.1	60
Load 1 house (kWh/day)				12.98
Load 30 houses (kWh/day)				389.4
Peak load (kW)				82.71

3.3 Proposed HRES Components and Parameters

The proposed HRES has five main components comprised of a diesel generator, PV arrays, wind turbines, a converter (inverter), and a battery storage system.

The PV panels cover an area of 1.627 m^2. They yield a DC output and thereby require an inverter for AC conversion. Details are available in Table 2.

A Generic 3kW is the model chosen for the wind turbines, which have an AC output. More detailed parameters could be found in Table 3.

Table 2. PV parameters.

PV Parameter Description	Specification
PV Panel Specification:	
Panel Type	Flat Plate (monocrystalline)
Model	Peimar SG300MBF
Rated Capacity	1 kW
PV Lifetime	30 years
Cost:	
Capital Cost	$650/kW
Replacement Cost	$650/kW
Operation & Maintenance Cost	$10
Temperature:	
Efficiency at STC	19.1%
Temperature Coefficient	-0.4%/ºC
Nominal Operating Cell Temperature	25ºC

Table 3. Wind turbine parameters.

Wind Turbine Parameter	Specification
Wind Turbine Specification:	
Turbine Type	Horizontal Axis
Model	Generic
Rated Capacity	3 kW
Turbine Lifetime	20 years
Cost:	
Capital Cost	$4,000
Replacement Cost	$4,000
Operation & Maintenance Cost	$180
Hub Height	30 m

The diesel generator is connected directly to the AC load. The fuel price is listed at $0.168/liter [20]. More specifications are shown in Table 4.

A generic large converter is used that functions as both an inverter and a rectifier to convert from DC to AC and vice versa. More specifications are displayed in Table 5. Any excess energy generated by the PV panels during the day, would be stored in the batteries in order to satisfy the load demand at night. The lead-acid batteries, whose details are listed in Table 6, were selected over the Li-ion batteries due to being less costly [21].

Table 4. Diesel generator parameters.

Diesel Generator Parameter	Specification
Diesel Generator Specification:	
Model	Generic
Rated Capacity	15 kW
Fuel Type	Diesel
Diesel Generator Lifetime	15,000 hours
Cost:	
Capital Cost	$220/kW
Replacement Cost	$220/kW
Operation & Maintenance Cost	$0.3/operating hour
Fuel Price	$0.168/liter

Table 5. Inverter Parameters

Converter Parameter	Specification
Converter Specification:	
Converter Type	Inverter / Rectifier
Model	Generic
Converter Lifetime	15 years
Cost:	
Capital Cost	$550/kW
Replacement Cost	$450/kW
Operation & Maintenance Cost	$10/kW/year
Efficiency	85% for Inverter/90% for Rectifier

Table 6. Energy storage system parameters.

Energy Storage Parameter	Specification
Energy Storage Specification:	
Battery Chemistry	Lead-Acid
Model	BAE PVS70
Nominal Capacity	0.804 kWh
Maximum Capacity	67 Ah
Nominal Voltage	12V
Battery Lifetime	5 years
Cost:	
Capital Cost	$62
Replacement Cost	$50
Operation & Maintenance Cost	$6/year

3.4 PV Modelling

The HOMER software can compute the PV output power by utilizing the following equation [22]:

$$P_{out} = P_{out,STC} * f_{derating} (\frac{I_T}{I_{T,STC}})[1 + \propto_P (T_C - T_{C,STC})] \tag{1}$$

where $P_{out,STC}$ is the output power at STC [kW], $f_{derating}$ is the derating factor [%], I_T is the incident solar radiation [kW/m^2], $I_{T,STC}$ is the incident solar radiation at STC [1 kW/m^2], α_p is the temperature coefficient of power [%/^{o}C], T_C is the temperature of the solar cell [^{o}C], and $T_{C,STC}$ is the temperature of the solar cell at STC [^{o}C].

3.5 Wind Turbine Modeling

In general, to calculate the electrical power generated by the wind turbines (P_{wind}) the following mathematical expression is used [23]:

$$P_{wind} = 0.5C_p * \rho_{air} * A_{rotor} * v^3 * 10^{-3} * \eta_{wind} * \eta_{gen} \tag{2}$$

where C_p denotes the power coefficient of the wind turbine, ρ_{air} is the air density [1.225 kg/m^3], A_{rot} represents the rotor swept area [m^2], v is the wind speed [m/s], η_{wind} denotes the turbine efficiency [%], and η_{gen} is the generator efficiency [%].

3.6 Diesel Generator Modeling

To compute the generator output power ($P_{DG,\,out}$), the below formula is used [24]:

$$P_{DG,out} = \frac{F_{cons} - (a * P_{DG,rated})}{b} \tag{3}$$

where F_{cons} symbolizes the rate of fuel consumed [L/h], $P_{DG,\,rated}$ denotes the diesel generator rated capacity [kW], a represents the fuel curve intercept coefficient [L/h/kW$_{rated}$], and b indicates the fuel curve slope of the diesel generator [L/h/kW$_{out}$].

3.7 Economic Modeling

HOMER utilizes a series of economic parameters for optimization. First, the NPC, represented by the capital, replacement, and any operational costs, to be subtracted from the salvage value, is calculated through the following expression [25]:

$$NPC = CC + RC + OC - SV \tag{4}$$

where CC refers to the capital cost [$], RC represents the replacement cost [$], OC is used to denote the operation cost of the installed system [$], and SV stands for the salvage cost [$]. The NPC is the main objective function to be minimized.

Then, the CRF ratio is computed by utilizing the following formula [26]:

$$CRF = \frac{RDR(1 + RDR)^{LT}}{(1 + RDR)^{LT} - 1} \tag{5}$$

where RDR is the real discount rate [%], and LT is the system lifetime [years].

Subsequently, the NPC is corrected by multiplying it with the CRF ratio to yield the annualized total costs (ATC) [$/year] and is given by the expression [27]:

$$ATC = NPC * CRF \tag{6}$$

Finally, the COE [$/kWh], is evaluated by employing the subsequent equation [27]:

$$COE = \frac{ATC}{AEP} \tag{7}$$

where AEP is the annual energy production [kWh] of the HRES.
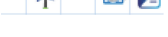
4   Results and Discussion

4.1   HOMER Optimization Results

After running thousands of simulations, HOMER software has yielded six possible configurations that would meet the daily load requirements of 389.4 kWh/day and a peak of 82.71 kW. The results are displayed in ascending order, as evident in Table 7, with the systems having the lowest NPC and COE being prioritized. Ultimately, the optimized design is observed to consist of all the five elements, revealing a combination of the succeeding components: 153 kW PV, two 3 kW wind turbines, a 15 kW diesel generator, a 65 kW converter, and 503 strings of 12 V lead-acid batteries for storage, against a NPC and COE of $358,617 and $0.166/kWh respectively. A schematic of the proposed HRES is shown in Fig. 8. Furthermore, the proposed HRES has RF of 92.8%, indicating that only 7.2% of the total energy demands would be satisfied through non-renewable means.

It can also be observed that attaining a 100% RF would require an arrangement of 172 kW PV, fifteen 3 kW wind turbines, a 75 kW converter, and 585 strings of 12V batteries, which can be achieved at a reasonably higher NPC of $475,374 and COE of $0.22/kWh, in case the environmental impacts are prioritized. From another perspective, the significance of including a diesel generator to reduce the overall costs of the project is demonstrated through this case.

Table 7. Optimization results of the various HRES configurations.

Configuration	PV (kW)	No. of 3kW WT	DG (kW)	Conv (kW)	No. of batteries	NPC ($)	COE ($/kWh)	RF (%)
	153	2	15	65	503	358,617	0.166	92.8
	207	--	15	65	506	382,298	0.177	93.7
	172	15	--	75	585	475,374	0.220	100
	314	--	--	70	856	537,838	0.249	100
	--	32	15	65	2,019	891,528	0.413	92.6
	--	65	--	80	2,621	1.29M	0.599	100

4.2   Economic Analysis

Figure 7 showcases a comparison of the total costs incurred by the various components of the hybrid system. It is clear that the BSS contributes the largest portion of the costs, followed by the solar PV system, with a NPC of $138,493 and $116,854.

Finally, the summation of the diesel generator and wind turbine costs, constituting around one third of the BSS costs, denote the lowest cost in the project overall, projecting a NPC of $29,970 and $15,444 correspondingly.
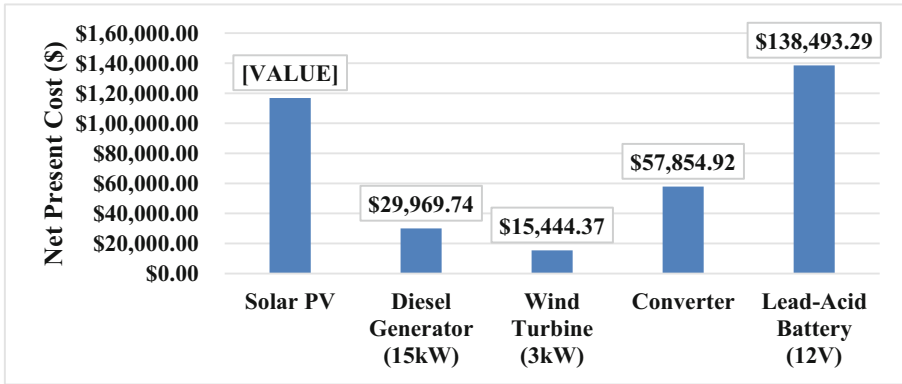
Fig.7. Net present cost (NPC) for each system component.

4.3 Technical Analysis

The optimized HRES yields an annual excess electrical energy output of 109,231 kWh/year at the lowest cost. The electrical output distribution is shown in Fig. 8.
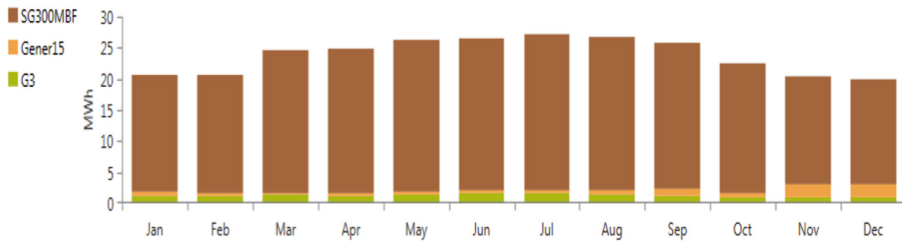

Fig. 8. Monthly electricity production by PV, wind, and a diesel generator.

The electricity production takes a nominal distribution shape. This is because the energy demand spikes from May till August, representing the summer season where the residential load is at its peak due to the overuse of air conditioners. Much of the electricity demand, approximately 91.2%, is satisfied by the PV, which is equivalent to almost 260,620 kWh/year, while the wind turbines and diesel generator only supply about 5.21% and 3.58% respectively of the total demand.

4.4 Environmental Analysis

The environmental impacts of the proposed HRES configuration would be studied by comparing it with a diesel generator system (used as the base case) to provide a sensible representation of the electricity generated by traditional power plants. Consequently, this would aid in reflecting the positive effects of the HRES on the environment. The optimization results of the base case system demonstrate a NPC of $745,259 and a COE of $0.345/kWh.

First, the base case has a zero RF which means that the amount of fuel and in turn the amount of toxic emissions generated could be used as a reference for comparison. Next, a summary of the amount of annual fuel consumed by the proposed HRES and the base case is provided below in Figs. 9 and 10, respectively.

Quantity	Value	Units
Total fuel consumed	3,809	L
Avg fuel per day	10.4	L/day
Avg fuel per hour	0.435	L/hour
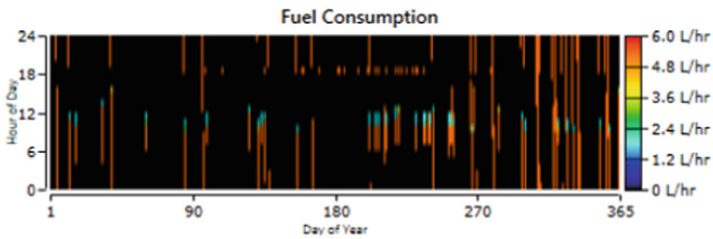
Fig. 9. Annual fuel consumption details for proposed HRES.

For the HRES, the volume of fuel consumed yearly by the diesel generator equates to 3,809 L/year, with a daily average of 10.4 L/day as indicated in Fig. 9.

Quantity	Value	Units
Total fuel consumed	81,607	L
Avg fuel per day	224	L/day
Avg fuel per hour	9.32	L/hour
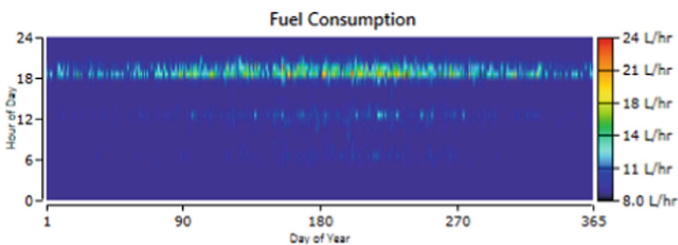
Fig. 10. Annual fuel consumption details for base case.

Figure 10 shows that the quantity of fuel used annually in the base case is 81,607 L/year, whilst attaining an average daily fuel consumption of 224 L/day.

Finally, the quantity of each pollutant generated by the base case and the proposed HRES is then compared and the results are indicated in Fig. 11. In addition, the base case is always responsible for the higher production of pollutants, approximately 20 times greater than the HRES for all gas types. More details are listed in Table 8.
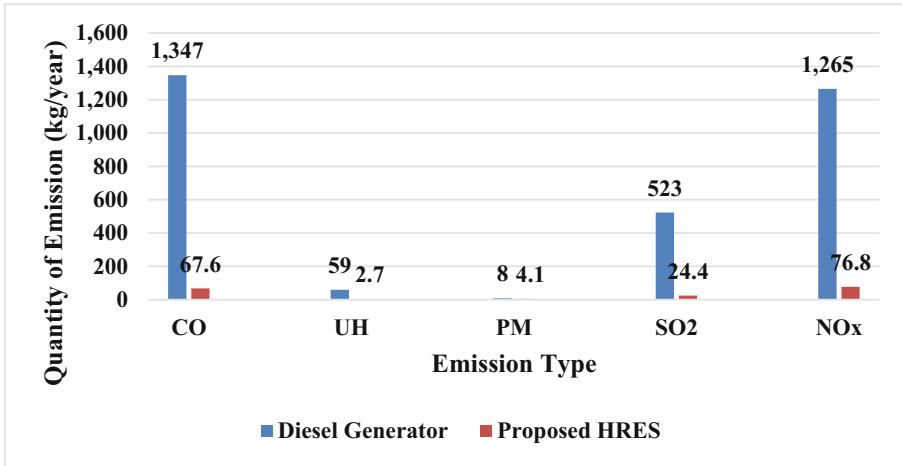
Fig. 11. Analysis of the environmental impacts between DG and HRES.

Consequently, the use of solar and wind technologies helps to drastically reduce the harmful emissions, traditionally generated by the combustion of the diesel fuel. This is achieved by reducing the operational hours of the diesel generator. At the same time, the addition of the diesel generator aids in offsetting the total capital costs.

Table 8. Emissions produced by the diesel generator and the proposed HRES.

Emission Gas	Quantity DG (kg/year)	Quantity HRES (kg/year)	Amount Saved (kg/year)
Carbon Dioxide	213,616	9,964	203,652
Carbon Monoxide	1,347	67.6	1,279.4
Unburned Hydrocarbon	58.8	2.74	56.06
Particulate Matter	8.16	4.10	4.06
Sulfur Dioxide	523	24.4	498.6
Nitrogen Oxides	1,265	76.8	1,188.2

5   Conclusion

In conclusion, the gradual increase of population, and the proposition of energy and environmental focused policies like "Vision 2030" and "Net Zero Plan" in KSA, has driven the desert country to actively pursue sustainable and clean energy forms.

The novelty of this paper lies in its focus on evaluating the compatibility of applying a HRES specifically in Al Qurayyat city. By obtaining the GHI, temperature and wind speed resource data of the designated site, it was established that there is great potential for solar and wind energy applications. Consequently, system optimization was done and analyzed from an economic perspective to determine the most feasible configuration and a technical analysis was also conducted to identify the annual quantity of energy yielded by the system. The design and optimization results of the HRES show the following:

- Six configurations are revealed that would meet the load requirements, where the daily energy demand is 389.4 kWh/day with a peak load of 82.71 kW.
- The selected PV/WT/DG/BSS arrangement is identified to yield the lowest NPC and COE with the values being $358,616 and $0.166/kWh respectively. Also, this configuration has a 92.8% RF.
- Alternatively, the PV/WT/BSS has a 100% RF, but at a moderately higher NPC and COE of $475,374 and $0.22/kWh, correspondingly.
- The annual energy generated by the PV, wind turbines, and diesel generator is 260,618, 14,891, and 10,241 kWh/year, respectively.

Finally, an environmental assessment was made revealing that the HRES saves 203,652 kg of CO_2, 1,279.4 kg of CO, 56.06 kg of unburned hydrocarbons, 4.06 kg of particulate matter, 498.6 kg of SO_2, and 1,188 kg of NOx.

References

1. Sönnichsen, N.: World Primary Energy Consumption 2020. Statista, 12 August 2021. https://www.statista.com/statistics/265598/consumption-of-primary-energy-worldwide/. 12 Dec 2021
2. Total energy consumption. Enerdata. (n.d.). Retrieved December 12, 2021, from https://yearbook.enerdata.net/total-energy/world-consumption-statistics.html
3. Nelson, J.: The Physics of Solar Cells. Imperial College Press And Distributed By World Scientific Publishing Co., Singapore (2003). https://doi.org/10.1142/p276
4. Hau, E.: Wind Turbines: Fundamentals, Technologies, Application, Economics. Springer, Heidelberg (2013). https://doi.org/10.1007/978-3-642-27151-9
5. Spera, D.A.: Introduction to modern wind turbines. In: Wind Turbine Technology: Fundamental Concepts of Wind Turbine Engineering, pp. 47–72 (1994)
6. Benton, K., Yang, X., Wang, Z.: Life cycle energy assessment of a standby diesel generator set. J. Clean. Prod. **149**, 265–274 (2017)
7. Deb, S., Ghosh, D., Mohanta, D.K.: Reliability analysis of PV cell, wind turbine and diesel generator by using Bayesian network. In: 2016 international conference on electrical, electronics, and optimization techniques (ICEEOT), pp. 2714–2719. IEEE, March 2016
8. Rezk, H., Dousoky, G.M.: Technical and economic analysis of different configurations of stand-alone hybrid renewable power systems–a case study. Renew. Sustain. Energy Rev. **62**, 941–953 (2016)
9. Baneshi, M., Hadianfard, F.: Techno-economic feasibility of hybrid diesel/PV/wind/battery generation systems for non-residential large electricity consumers under southern Iran climate conditions. Energy Convers. Manage. **127**, 233–244 (2016)
10. Rajbongshi, R., Borgohain, D., Mahapatra, S.: Optimization of PV-biomass-diesel and grid base hybrid energy systems for rural electrification. Energy **126**, 461–474 (2017)
11. Murugaperumal, K., Raj, P.A.D.V.: Feasibility design and techno-economic analysis of hybrid energy system for rural electrification. Sol. Energy **188**, 1068–1083 (2019)
12. Krishan, O., Suhag, S.: Techno-economic analysis of a hybrid renewable energy system for an energy poor rural community. J. Energy Storage **23**, 305–319 (2019)
13. Nguyen, H.T., Safder, U., Nguyen, X.N., Yoo, C.: Multi-objective decision-making and optimal sizing of a hybrid renewable energy system to meet the dynamic energy demands of a wastewater treatment plant. Energy **191**, 116570 (2020)

14. Rinaldi, F., Moghaddampoor, F., Najafi, B., Marchesi, R.: Economic feasibility analysis and optimization of hybrid renewable energy systems for rural electrification in Peru. Clean Technol. Environ. Policy **23**(3), 731–748 (2020). https://doi.org/10.1007/s10098-020-01906-y

15. Esfilar, R., Bagheri, M., Golestani, B.: Technoeconomic feasibility review of hybrid waste to energy system in the campus: a case study for the University of Victoria. Renew. Sustain. Energy Rev. **146**, 111190 (2021)

16. Tariq, R., et al.: Artificial intelligence assisted technoeconomic optimization scenarios of hybrid energy systems for water management of an isolated community. Sustain. Energy Technol. Assess. **48**, 101561 (2021)

17. Mas'ud, A.A., AlGarni, H.Z.: Optimum configuration of a renewable energy system using multi-year parameters and advanced battery storage modules: a case study in Northern Saudi Arabia. Sustainability **13**(9), 5123 (2021). https://doi.org/10.3390/su13095123

18. Google. (n.d.). Average+Electric+Kettle+Wattage. Google Shopping. https://www.google.com/shopping/product/. 9 Apr 2022

19. Robert, F.C., Sisodia, G.S., Gopalan, S.: The critical role of anchor customers in rural microgrids. In: 2017 International Conference on Computation of Power, Energy Information and Commuincation (ICCPEIC), pp. 398–403. IEEE, March 2017

20. Ahmed, J., Harijan, K., Shaikh, P.H., Lashari, A.A.: Techno-economic feasibility analysis of an off-grid hybrid renewable energy system for rural electrification. J. Elect. Electron. Eng. **9**(1), 7–15 (2021)

21. Çetinbaş, İ., Tamyürek, B., Demirtaş, M.: Design, analysis and optimization of a hybrid microgrid system using HOMER software: Eskisehir osmangazi university example Int. J. Renew. Energy Dev. IJRED. **8**(1), 1–15 (2019)

22. Mahesh, A., Sandhu, K.S.: Hybrid wind/photovoltaic energy system developments: critical review and findings. Renew. Energy Rev. **52**, 1135–1147 (2015)

23. Ramli, M.A., Bouchekara, H.R.E.H., Alghamdi, A.S.: Optimal sizing of PV/wind/diesel hybrid microgrid system using multi-objective self-adaptive differential evolution algorithm. Renew. Energy **121**, 400–411 (2018)

24. Kumar, P., Pukale, R., Kumabhar, N., Patil, U.: Optimal design configuration using HOMER. Proc. Technol. **24**, 499–504 (2016)

25. OulisRousis, A., Tzelepis, D., Konstantelos, I., Booth, C., Strbac, G.: Design of a hybrid AC/DC microgrid: case study on a residential application. Inventions **3**(3), 55 (2018)

26. Kumar, Y.P., Bhimasingu, R.: Optimal sizing of microgrid for an urban community building in south India using HOMER. In: 2014 IEEE International Conference on Power Electronics, Drives and Energy Systems (PEDES), pp. 1–6. IEEE, December 2014

27. Demiroren, A., Yilmaz, U.: Analysis of change in electric energy cost with using renewable energy sources in Gökceada, Turkey: an island example. Renew. Sustain. Energy Rev. **14**(1), 323–333 (2010). https://doi.org/10.1016/j.rser.2009.06.030

On-Site Stacking Efficiency Performance of a Novel Full-3D-Printed Plant Microbial Fuel Cell Electrode Assembly

Miguel Angelo M. Chua[1], Abby Joy T. De Los Santos[1], and Kristopher Ray S. Pamintuan[1,2(✉)] ⓘ

[1] School of Chemical, Biological, and Materials Engineering and Sciences, Mapua University, Manila, Philippines
krspamintuan@mapua.edu.ph
[2] Center for Renewable Bioenergy Research, Mapua University, Manila, Philippines

Abstract. Plant microbial fuel cells (PMFCs), a derivative of microbial fuel cells, are a clean and renewable energy source that utilizes plants and bacteria to generate bioelectricity. The electrodes utilize the electrons generated by the bacteria for a redox reaction to occur. In this study, the 3D-printed PMFC stake was designed and tested, which paved the way an accessible, convenient, and inexpensive electrodes while maintaining the ability to compete with other electrodes in terms of electricity generation. Series and parallel connections were significant due to the increase of the power output, from the average individual power of 1.06×10^{-9} W, the average power increased up to an output of 5.47×10^{-7} W provided by three-stack cells connected in series, and the highest obtained value was at 1.62×10^{-4} W from a nine-stack parallel connection. The highest power density obtained was 9.18 mW/m^2 for the output setting, and it is obtained from the nine cells connected in parallel. These results proved that PMFC could be utilized for simultaneous electricity generation and food production. Additionally, the output power and power densities showed the potential of large-scale applications of PMFCs.

Keywords: Bioelectricity · Plant-microbial fuel cell · 3D-printed electrodes

1 Introduction

Plant microbial fuel cells (PMFCs) are defined as the derivative of microbial fuel cells that utilize plants to provide organic compounds for the electrochemically active bacteria (EAB) in the soil [1]. Through photosynthesis, plants release rhizodeposits consumed by the bacteria in the roots, allowing bacteria's metabolism to generate electrons. This plant–microbe relationship that occurs in the rhizosphere region resulted in bioelectricity generation from the bacteria. Similar to the microbial fuel cells, oxidation occurs in the anode, while reduction occurs in the cathode. The electrons released by the EAB are received and oxidized in the anode. Then, the electrons pass through an external load to reach the cathode while the protons are transferred towards the cathode through a

potential gradient. Finally, the protons and the electrons underwent a reduction process at the cathode, which resulted in bioelectricity generation [2]. Thus, the PMFCs fulfill their purpose of simultaneous electricity generation and food production. Even though PMFC is a promising source of renewable energy, the availability and costs for the materials utilized for the PMFCs, especially the electrodes, are still a challenge. In this study, the researchers replaced the existing electrode materials with 3D-printed PMFC electrodes incorporated into a garden stake. 3D printing is utilized to easily manufacture the electrodes at a lower cost while maintaining their ability to compete with other electrodes in terms of electricity generation. The garden stake design paved the way for a wider range of people who can utilize PMFC since its shape may be applied to different plants.

The PMFCs utilize plant roots to activate the electrochemically active bacteria (EAB) from the anode through rhizodeposition, resulting in electricity generation [1]. PMFCs usually utilize soil as their substrate such that many microorganisms can be found within the soil, thus the dependence of the energy generation. Different materials for the electrodes of the PMFCs can be used, but each electrode has its own set of advantages and disadvantages. The anode is in contact with the root, while the cathode is implanted in the soil a bit higher than the anode. The electrochemically active bacteria that receive organic compounds from the rhizodeposits generate electrons utilized in the anode. Meanwhile, the soil acts as a substrate in the system. Soils like agricultural soils and forest soils may be used as a substrate. However, as a substrate, it is proven that agricultural soils can produce 17 times more power than forest soils [3]. Furthermore, 3D Printed Electrodes have already been used in different fields, but most studies suggest that these electrodes are used for sensors. Thus the aim of the study is that the 3D printed electrodes may be applied in the PMFC mechanism to produce cheaper electrodes conveniently. The filament utilized for the electrodes is the Protopasta (ProtoPlant, USA) conductive poly-lactic acid filament, and its design is similar to a garden stake. The PMFC is inserted into the soil, attaching the anode to the root while the cathode is on the upper surface.

Indeed, PMFCs have excellent potential in bioelectricity generation since they are renewable and clean energy sources. However, the power generation of PMFCs is still a challenge since their power is not yet high enough to be an economically viable source of renewable energy. These low power densities are the effect of the internal resistances present in the system, and the examples of these are ohmic, activation, bacterial metabolic, and concentration losses [4]. Consequently, the values of the power produced are erratic, and the resulting power densities indicate unstable power generation. Fortunately, series and parallel stacking can be applied to maximize the cells' power output. Proper stacking combinations showed significant effects on the performance of PMFCs as it results in power amplification [5]. This study focused on the stacking efficiency wherein the 3D-printed electrodes are connected in series and parallel. In that way, the potential of the PMFCs to be applied on a larger scale through stacking is investigated.

2   Methodology

2.1   Plant-Microbial Fuel Cell Assembly

Turmeric (Curcuma longa) plants in continuous soil (non-potted) are utilized in an outdoor system. The plants are utilized as the source of organic compounds that are helpful for the bacteria in power generation. However, the rate of the release of the organic compounds from plants is different from each other. Thus, the power generation of the plant microbial fuel cell system is affected. The setup of the plant microbial fuel cell is shown in Fig. 1.

Fig. 1.   PMFC set-up

The PMFC stake, as shown in Fig. 2, consists of three parts, namely, the cathode, anode, and the separator. The cathode is where the reduction reaction takes place. On the other hand, the site for oxidation, anode, also acts as the water compartment for the release of water to be controlled. Finally, the separator is also used wherein it has to be permeable with water. The conductive ProtoPasta (ProtoPlant, USA) conductive polylactic acid (PLA) filament is used for the electrodes (anode and cathode), labeled as black in Fig. 2. Meanwhile, an ordinary PLA + filament was used for the separator, labeled as color blue in Fig. 2. The 3D-printed electrode also served as a watering stake for the plants with a measured water retention time of 59 h.

The dimensions of the PMFC stake are provided in Table 1. As mentioned earlier, the electrodes are also designed as a watering stake for the plants. Watering stakes hold the water for a short period and slowly release the water through the small holes. The 3D printed electrodes are appropriate to be a watering stake as they can also slowly release the water since the prints were not water-tight, meaning water can also flow outside. Additionally, watering stakes are very helpful to plants as it allows water and oxygen to be transported directly to the plant's roots. As a result, the watering stakes promote strong root development. Healthier roots would produce a good supply of rhizodeposits beneficial for the microbes as they consume the nutrients from the roots and metabolize them to generate electrons. Also, soil saturation is maintained as the water is held inside
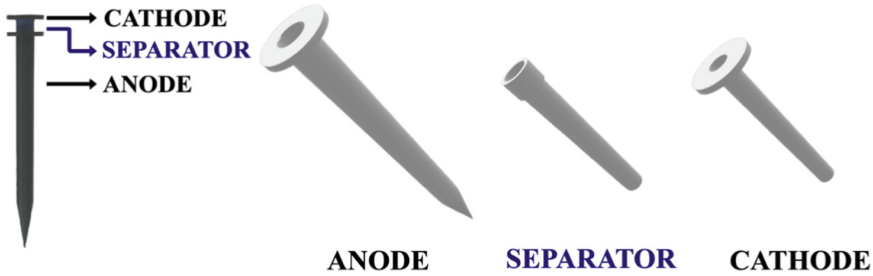
Fig. 2. PMFC stake parts

the watering stake, preventing the run-off and evaporation of the water. Thus, the design of the PMFC stake is advantageous as it provides a more efficient electron generation and, at the same time, produces healthier plants.

Table 1. Size of PMFC stake

	Anode	Separator	Cathode
Overall length	200 mm	100 mm	100 mm
Surface area	18,970.51 mm^2	7,801.75 mm^2	8,006.96 mm^2
Lip			
Length	3 mm	10 mm	3 mm
Outside diameter	30 mm	15 mm	30 mm
Inside diameter	13 mm	11.5 mm	9.9 mm
Body			
Length	197 mm	90 mm	97 mm
Outside diameter	15 mm	12.5 mm	10.9 mm
Inside diameter	13 mm	11.5 mm	9.9 mm
Wall thickness	1 mm	0.5 mm	0.5 mm

2.2   Measurement and Monitoring

The voltage and current readings are measured against a 1000-Ω resistor using a digital multimeter, and it is manually recorded five times daily (9 AM, 12 PM, 3 PM, 6 PM, and 9 PM) for the preliminary testing. In that way, the effect of plants' sunlight exposure to power generation can be observed. This measurement is done by connecting the 3D-printed electrodes with the copper wires and the alligator clips. After the preliminary tests for ten (10) days, individual cell monitoring took place wherein the voltage and current reading for all the nine plants were measured. Also, stacking efficiency studies are performed wherein various combinations for the three cells, and nine cells are connected

in series and parallel are obtained, and its setup is shown in Fig. 3. The individual cell monitoring and the series and parallel stacking combinations are measured daily for twenty (20) days. Furthermore, cumulative stacking is observed wherein measurements took place on an increasing number of sequentially stacked cells in series and parallel. Additionally, the voltage reading for different resistors ranging from ten to fifty-one thousand ohms (10Ω–$51,000\Omega$) is measured for the polarization studies to identify the effect of increasing the external resistance in the PMFC system. Unlike the individual cell monitoring and series and parallel stacking combinations, the cumulative stacking is measured weekly, while the polarization studies are only measured once every five days. Throughout the experimentation process, the soil from the plants is not allowed to dry out since its moisture may affect the power generation of the soil. Also, the temperature is considered since its sudden fluctuations may affect electricity generation.

Furthermore, power and power density are calculated through the recorded values of voltage and currents. The power followed the formula, $P = V^2/R$, wherein V and R are the obtained voltage and utilized resistor, respectively. Meanwhile, the formula used for the power density and current density are $P_D = P/A$ and $I_D = I/A$, respectively, where A is the nominal anode area.
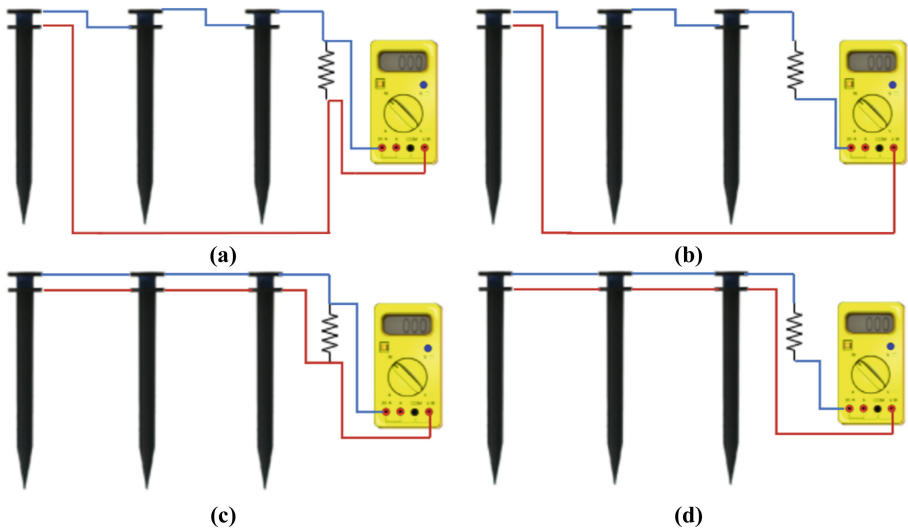
Fig. 3. Stacking setup for measuring (a) voltage and (b) current in series and (c) voltage and (d) current in parallel

3   Results and Discussion

3.1   Preliminary Voltage and Current Readings

Shown in Fig. 4 is the electrodes' daily monitoring of the voltage and current from 9:00 AM to 9:00 PM with three (3) hours interval per measurement. From the obtained data,

there are times that at 12:00 PM, the peak of the voltage and current measurement is defined. However, there are also possibilities that the peak is at another time slot. These differences in the peak per day are due to uncontrolled variables such as the soil saturation through the presence of rain. The voltage and current reading are observed to be higher when there is the presence of water that serves as a medium for the microorganisms. This behavior is reasonable as the presence of water enabled the internal resistance present in the system to be reduced, resulting in good ionic mobility between the electrodes [6]. Additionally, it is evident that the data from the measured voltage and currents have increased as the days passed since the trend increased over time. This observation is an excellent indication that an increased amount of rhizodeposits from plants occurred, resulting in an increased amount of microorganisms present in the rhizosphere [7].
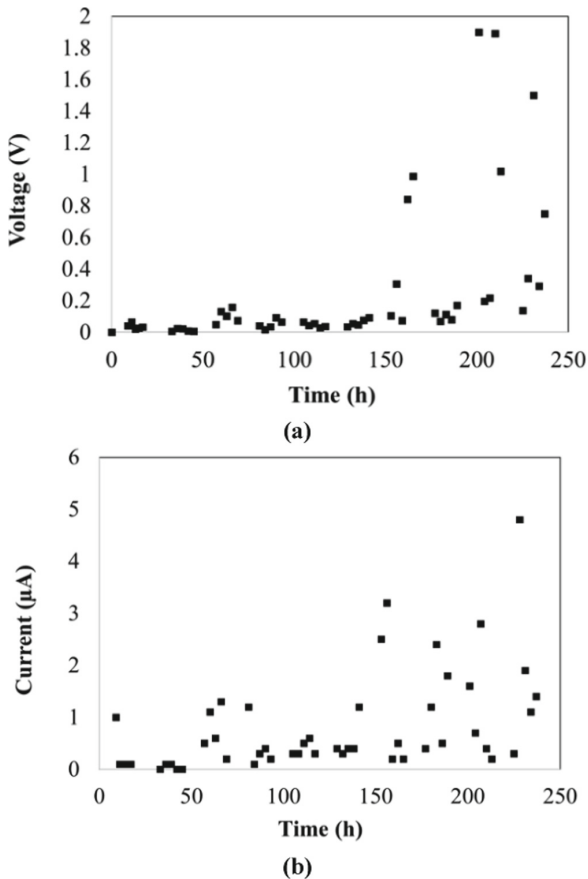
Fig. 4. Preliminary data for (a) voltage and (b) current

3.2 Individual and Stacked Cells Comparison

The plot between the obtained average voltage (volts) versus the time (days) for comparing the individual cells, three cells, and nine cells is shown in Fig. 5. From these two figures, it is evident that the individual cells and the cells connected in series have comparable similarities, such that the graph showed an overlap in the figures. On the other hand, the measured voltage from parallel stacking is higher than that of the series connection and individual cells. An increased voltage in the parallel stacking showed PMFC's potential for large-scale applications. Meanwhile, the relative similarities between the voltage from the individual cells and series stacking indicated that voltage reversal may have occurred, caused by the electron drive between the cells with high potential and cells with low potential, which led to the voltage losses [8].
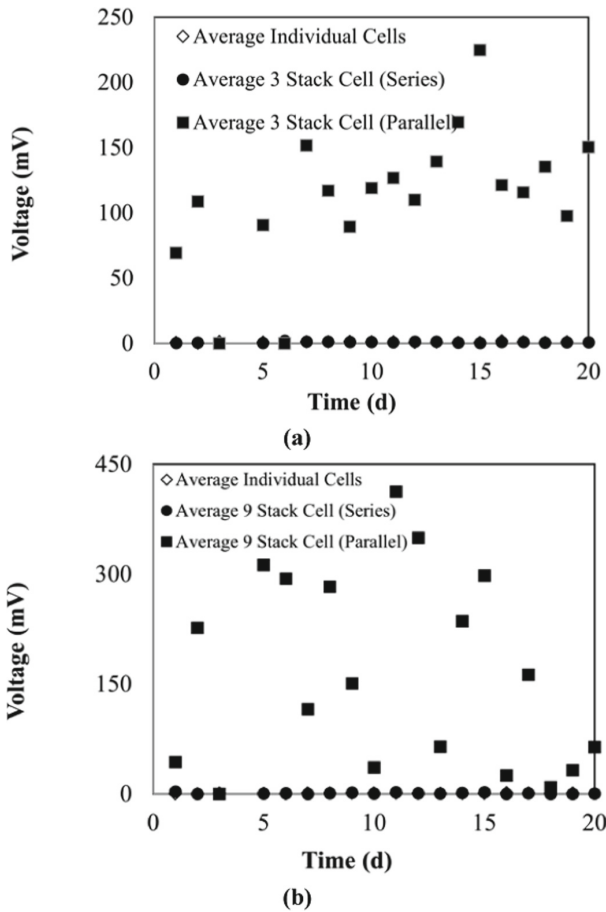
Fig. 5. Daily average voltage comparison between the (a) individual cells and three stacked cells connected in series and parallel and (b) individual cells and nine stacked cells connected in series and parallel

Furthermore, the obtained average current (microamperes) versus the time (days) between the individual cells, three cells, and nine stacked cells are plotted in Fig. 6. The current is expected to be similar to the individual cells in series stacking, while the current for cells stacked in parallel is projected to be greater than the individual cell readings [5]. The principles of ohm's law supported this analysis wherein the total current is constant for the series circuit due to the continuity on the charge flowing, while the total current is equal to the sum of all the individual currents in parallel current.
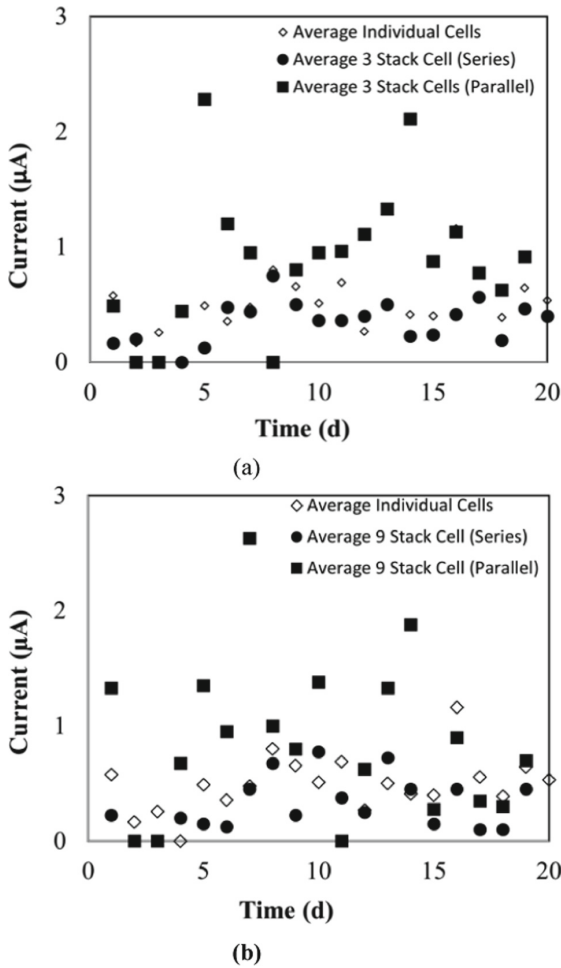
Fig. 6. Daily average current comparison between the (a) individual cells and three stacked cells connected in series and parallel and (b) individual cells and nine stacked cells connected in series and parallel

Moreover, it is important to note that differences in light intensity cause differences in voltage output. Photosynthetic active radiation (PAR) estimates at 150 W/m^2 in western Europe. Compared to the PAR in the equatorial region, it would amount to a higher amount of 10 times higher than the PAR of western Europe [9]. It could be used as a basis where the more the sun is highly concentrated, the higher the voltage or output.

3.3   Series and Parallel Stacking

In Fig. 7, it is evident that the stacking of the cells can be concluded as successful in terms of its voltage and current reading because almost all of the actual values exceeded the expected voltages in series and parallel stacking. It is expected that for higher numbers of cells stacked, the voltage would increase together with its current. This theory could be understandable if the three-stacked is compared to the nine-stacked. Based on the measurements, the values of the voltages and currents of the nine-stacked are a lot greater than the three stacked. In some instances, a three stacked cell could reach at least the range of nine stacked due to the soil saturation, which leads to some spike in the readings. Uncontrollable parameters, like rain, improved the PMFC performance due to the increased mobility of the bacteria.
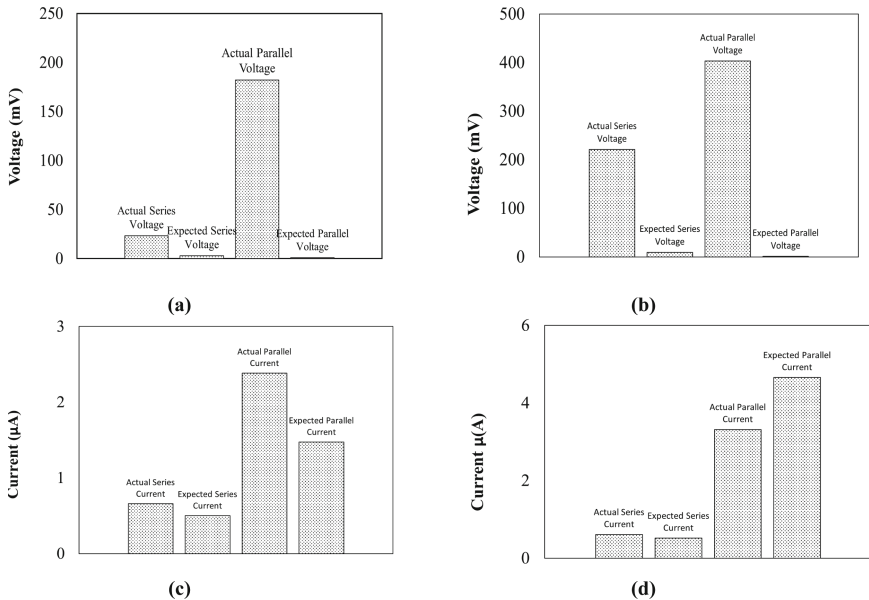
Fig. 7. Voltage comparison between the actual and expected values of (a) three stacked cells connected in series and parallel and (b) nine stacked cells connected in series and parallel; and Current comparison between the actual and expected values of (c) three stacked cells connected in series and parallel and (d) nine stacked cells connected in series and parallel

It can also be observed that the current and voltage reading gathered for series are lower than the parallel connection due to the theory that the presence of one damaged

cell in series stacking leads to the defect in the whole connection while damage in a single cell does not affect the whole connection for parallel stacking as the defective cell can be isolated. The results showed that the voltage and current of parallel connections are significantly higher than the series connections.

3.4   Cumulative Stacking

Cumulative stacking can conclude different aspects, first is how cells in a series connection depend on every cell to provide power. Meanwhile, in a parallel connection, cells are independent of one another. Another conclusion is how adding cells in connection can generate a greater amount of voltage. From Fig. 8(a) and (b), the trend would show that it increases while more cells are added, and comparing the actual from the theoretical, the trend shows that it is expected to increase. Few situations can be noted, such as random drops in the voltage that are evident in the graphs. One faulty cell found within the connection would affect the overall performance of the circuit [10]. Due to this effect, the output voltages in the exceeding connections will only increase limitedly.
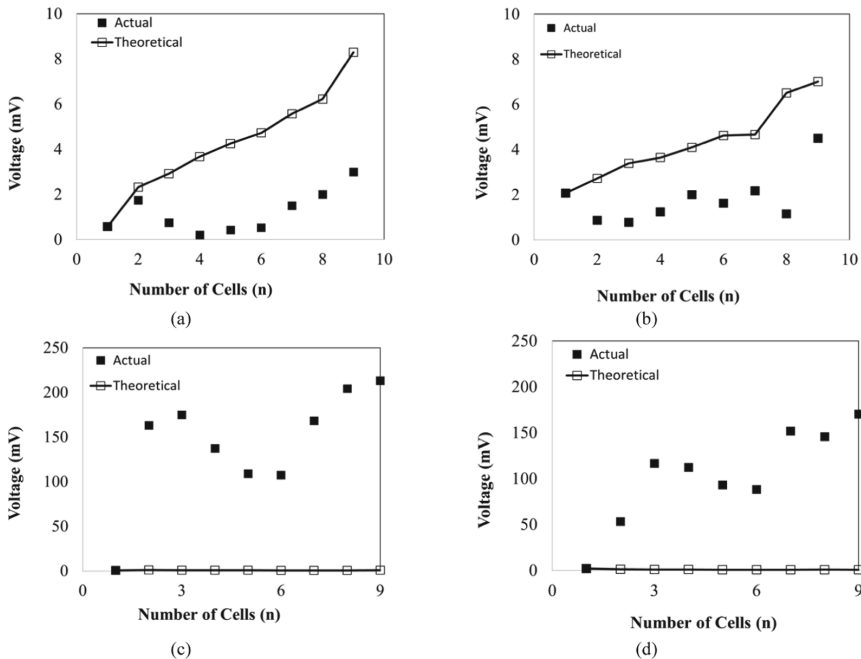
Fig. 8. Voltage response to (a) series, (b) series reverse, (c) parallel, and (d) parallel reverse cumulative stacking

In a parallel sense, the actual voltage measured was greater than the theoretical or the expected value. Some of the data from Fig. 8(c) and (d) gave a lower output than the prior values. These results can be related to some faulty cells. However, due to a parallel connection, it is possible to increase the voltage such that the cells are not dependent on

one another. Despite having voltage drops in some connections, theoretically, the voltage would increase only if cells were fully functioning. Until then, it is expected that there will be voltage loss due to different factors, and some of them could be due to weather, faulty cell, lack of microorganisms, and voltage reversal.

3.5 Polarization Studies

Increasing resistance shows that the voltage would also increase. These results could be defined by the formula $V = IR$, wherein the voltage is proportional to its resistance. The formula supported the reason why at a lower resistance, the reading would be low voltage to none. The sense of measuring the voltage at different resistance would be because of its application on the ground. Remember, the electrons may have difficulties moving towards the cells within the soil due to resistances [11].

Outliers were found in Fig. 9 (b) and (c). For Fig. 9 (b), the outlier was found in 3.3 kΩ, which read a voltage of 0.4128 V, and for Fig. 9(c), a resistance of 1,000 Ω with a reading of 0.1825 V in the voltage. The voltage reaches a peak and slowly decreases as the resistance increases.
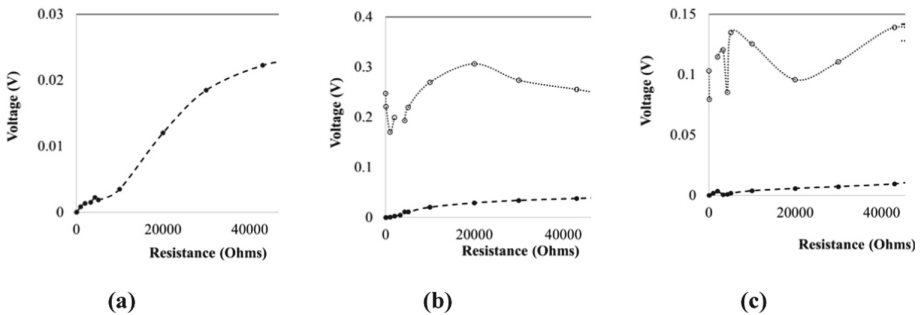
Fig. 9. Different resistors response of (a) individual cell voltage, (b) three stacked cells, (c) nine stacked cells

3.6 Power and Power Densities

Power and power densities have been calculated to compare the series and parallel stacking to the individual cells. The power and power densities comparison is presented in Fig. 10. The individual cells are denoted as "IND," while the three stacked cells were denoted as "3S" for series connection and "3P" for parallel connection. Meanwhile, the nine cells connected in series and parallel are denoted as "9S" and "9P. These parameters are compared side by side with each other to identify if stacking resulted in a better performance compared to the individual cells. The power and power densities showed exemplary results as all the studied systems have exceeded the performance of the individual cells, especially the nine cells connected in parallel. An increase in the anodic area is expected to provide higher power. This theory can be executed by stacking the cells to increase the total electrode surface area. Hence, it explained why the nine

cells connected in parallel provided greater power than the individual cells. The results showed a favorable outcome since it is desired for PMFCs to reach high power and density values. Thus, these results claim that power amplification and the possibility for large-scale applications can be achieved through the stacking of the PMFC system.
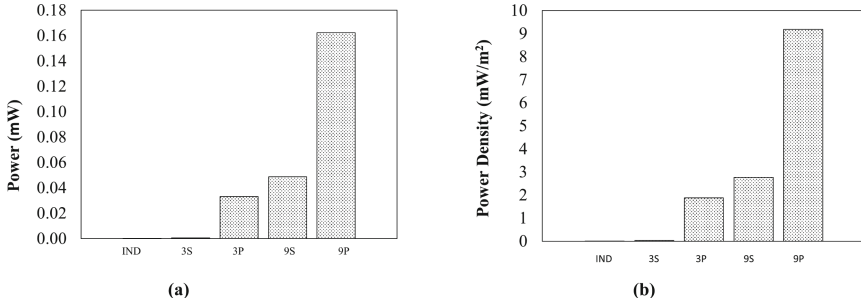

Fig. 10.   (a) Power and (b) power density of all studied systems: individual (IND), 3 cells in series (3S), 3 cells in parallel (3P), 9 cells in series (9S), and 9 cells in parallel (9P)

In comparison, the highest power output that the study obtained amounted to 9.18 mW/m^2 in terms of its power density and a voltage of 4.54 V, provided that its growth condition is moist soil. Some growth conditions may vary, such as different soil can be plain moist soil or be contaminated with chromium, or even soils with fertilizers and activated carbon [12]. This study obtained a higher power density than soils with activated carbon values at 1.04 mW/m^2, and lower than a growth condition which consists of soil containing an industrial fertilizer with a value of 350 mW/m^2. In terms of voltage, moist soil obtained higher than the soil contaminated with hexavalent chromium, which has a value of 0.162 V compared to the 4.54 V provided by 9 cells stacked in parallel.

4   Conclusion

Through this study, a 3D-printed PMFC was successfully designed and tested, which paved the way to accessible, convenient, and inexpensive electrodes while the ability to compete with other electrodes in terms of electricity generation is still maintained. The study proved the potential of the PMFC for simultaneous electricity generation and food production. If amplification of power is desired, parallel stacking has shown an outstanding result as actual values of the voltages exceeded the theoretical values, which allowed the power and power density to be greater. Furthermore, polarization studies have proven that higher external resistance leads to higher voltage responses. Even though the power outputs of PMFCs are known to be low compared to the energy demands, stacking efficiency studies have proven the potential for large-scale applications of PMFC.

References

1. Kabutey, F.T., et al.: An overview of plant microbial fuel cells (PMFCs): Configurations and applications. Renew. Sustain. Energy Rev. **110**, 402–414 (2019)

2. Shaikh, R., Rizvi, A., Quraishi, M., Pandit, S., Mathuriya, A.S., Gupta, P.K., Singh, J., Prasad, R.: Bioelectricity production using plant-microbial fuel cell: present state of art. South African J. Botany **140**, 393–408 (2021)
3. Roesch, L.F.W., et al.: Pyrosequencing enumerates and contrasts soil microbial diversity. ISME J. **1**, 283–290 (2007)
4. Pamintuan, K.R.S., Reyes, C.S.A., Lat, D.K.O.: Compartmentalization and polarization studies of a plant-microbial fuel cell assembly with cynodon dactylon. E3S Web Conf. **181**, 01007 (2020)
5. Pamintuan, K.R.S., Katipunan, A.M.C., Palaganas, P.A.O., Caparanga, A.R.: An analysis of the stacking potential and efficiency of plant-microbial fuel cells growing green beans (Vigna ungiculata ssp. sesquipedalis). Int. J. Renew. Energy Dev. **9**, 439–447 (2020)
6. Tapia, N., Rojas, C., Bonilla, C., Vargas, I.: A new method for sensing soil water content in green roofs using plant microbial fuel cells. Sensors **18**, 71 (2017)
7. Pamintuan, K.R.S., Ancheta, A.J.G., Robles, S.M.T.: Stacking efficiency of terrestrial plant-microbial fuel cells growing ocimum basilicum and origanum vulgare. E3S Web Conf. **181**, 01004 (2020)
8. Kuchi, S., Sarkar, O., Butti, S.K., Velvizhi, G., Mohan, S.V.: Stacking of microbial fuel cells with continuous mode operation for higher bioelectrogenic activity. Biores. Technol. **257**, 210–216 (2018)
9. Martínez, B., et al.: Evaluation of the LSA-SAF gross primary production product derived from SEVIRI/MSG data (MGPP). ISPRS J. Photogram. Remote Sens. **159**, 220–236 (2020)
10. Estrada-Arriaga, E.B., et al.: Performance of air-cathode stacked microbial fuel cells systems for wastewater treatment and electricity production. Water Sci. Technol. **76**, 683–693 (2017)
11. Nitisoravut, R., Regmi, R.: Plant microbial fuel cells: a promising biosystems engineering. Renew. Sustain. Energy Rev. **76**, 81–89 (2017)
12. Maddalwar, S., Kumar Nayak, K., Kumar, M., Singh, L.: Plant microbial fuel cell: opportunities, challenges, and prospects. Biores. Technol. **341**, 125772 (2021)

Investigation into the Temperature Effect on the Performance of CZTS(Se) Thin Film Solar Cells

Mohamed Moustafa[1](✉) and Tariq AlZoubi[2]

[1] Department of Physics, School of Sciences and Engineering, The American University in Cairo, AUC Avenue, P.O. Box 74, New Cairo 11835, Egypt
mohamed.orabi@aucegypt.edu

[2] College of Engineering and Technology, American University of the Middle East, Kuwait City, Kuwait
tariq.alzoubi@aum.edu.kw

Abstract. The objective of this study is to examine the effect of temperature on the performance parameters of the kieserite quaternary semiconductor compounds CZTS, CZTSe, and CZTSSe. For the purpose of this study, a SCAPS-1D model has been used. P-MoS(Se)$_2$ is positioned between the Mo back contact and the absorber layer, acting as an interfacial layer. From the results of this study, it is clear that the p-MoS(Se)$_2$ interfacial layer facilitates the quasi-ohmic contact between the CZTS(Se) heterojunctions and the Mo heterojunctions. Consequently, the J-V characteristic is steeper as a result of this finding. We examined all structures from 250 K to 450 K in terms of the temperature dependence of open-circuit voltage (V_{oc}), short-circuit current (J_{sc}), fill factor (FF), and power conversion efficiency (PCE). CZTSe-based solar cells have been found to perform best at high operating temperatures, according to a comparative study. Based on the voltage variation to temperature $\Delta V_{oc}/\Delta T$ coefficients of the CZTS and CZTSe-based solar cells, it was found that the voltage variation to temperature coefficients were respectively -2.15 and -1.4 mV/K as a result of temperature changes.

Keywords: Thin film · Solar cells · CZTS(Se) · SCAPS simulation

1   Introduction

Since thin-film solar cells (TFSC) have demonstrated remarkable properties and performances in recent years, they have gained significant attention for their potential use in solar cells. Recent research has explored copper zinc tin sulfide/selenide CZTS(Se) Kesterite quaternary compound semiconductors as promising TFSC materials. These materials exhibit excellent photovoltaic and electronic properties, including bandgap values (Eg) between 1.1 eV and 1.9 eV and absorption coefficients of ~105 cm-1 [1–4]. Further, they are environmentally friendly, cost-effective, and earth-abundant [5]. It has been reported that CZTS(Se) solar cells have improved in performance and efficiency through several theoretical and experimental studies [6–8]. CZTS-TFCS were reported

to have a power conversion efficiency of 9.66% [9], 10.1% [10], and 11.1% [11]. It was demonstrated that a champion CZTSe solar cell could achieve a high power conversion efficiency of 12.6% of those fabricated by utilizing a spin-coating process in conjunction with CdS as a buffer layer [12]. It is common for CZTS(Se) TFSCs to use Molybdenum (Mo) as the material for the back contact. As a result of unintentional interaction between CZTS(Se) absorber and Mo back contact, MoS(Se)2 interface layers have been discovered. The performance of solar cells is influenced by the interfacial layer. In contrast to Schottky-type contacts, MoS(Se)2 mediates ohmic contacts with Mo back contacts [13]. 2D metal dichalcogenides such as MoS(Se)2 belong to group VI of layered transition metal dichalcogenides (TMDCs). Due to their 2D nature, these materials have remarkable physical and structural properties. An atomic layer consisting of X, Mo, and X (X here is Se or S) is held together by a weak van der Waals bond, and the sheets are strongly in-plane covalently bonded. Furthermore, MoS(Se)2 has a broad bandgap ranging from 1.1 eV to 1.8 eV, which contributes to its high hole mobility [14, 15].

TFSCs perform poorly under high-temperature conditions due to the effects of high ambient temperatures. A goal of the study is to investigate the effect of temperature on kieserite quaternary CZTS, CZTSe, and CZTSSe based solar cells using a one-dimensional SCAPS simulation (SCAPS-1D). Our first discussion is focused on the interfacial layer of p-MoS(Se)$_2$ TMDC. Afterward, we discuss and analyze the J-V characteristics and photovoltaic parameters for all structures operating between 250 °C and 450 °C.

2   Device Modeling and Simulation

It is important to note that in this study, SCAPS-1D is used in order to investigate the effects of temperature on the performance of the CZT(S,Se) TFSCs. At the University of Gent, the SACPS codes have been developed [16]. As a result of its effectiveness, it has been used to simulate and study several thin solar cells, including those based on Perovskite, CIGS, and CdTe [17–19]. A steady-state band diagram, recombination profile, and carrier transport are calculated by SCAPS using the Poisson equation and hole and electron continuity equations. As part of this model, an AM 1.5 is used with a power density of 1000 watts per square meter of illumination. Basically, a solar cell has layers with different properties, including energy band gaps, layer thicknesses, and doping density [20, 21]. In Fig. 1, we can see a schematic representation of the structure of a CZTS(Se) solar cell. During the construction of this structure, n-type CdS is used as a buffer layer with an 80 nm thickness, followed by a layer of n-ZnO as the window layer. This scheme was implemented by inserting MoS(Se) interfacial layers between the device's active layer and back contact. The interfacial layers exhibit Hall mobilities between 150 and 250 cm^2/Vs at 295 K. In terms of the band gap, one layer of MoS(Se) will have a band gap between 1.2 eV and 1.4 eV, while monolayers can reach 1.9 eV. Furthermore, the p-MoS(Se)$_2$ carrier concentration is set to be 10^{18} cm^{-3}, which is a high concentration. As a standard, the thickness of the absorber layer has been selected as 2000 nm in all simulation structures. All modeling structures were based on this thickness, and it was used in all simulations.
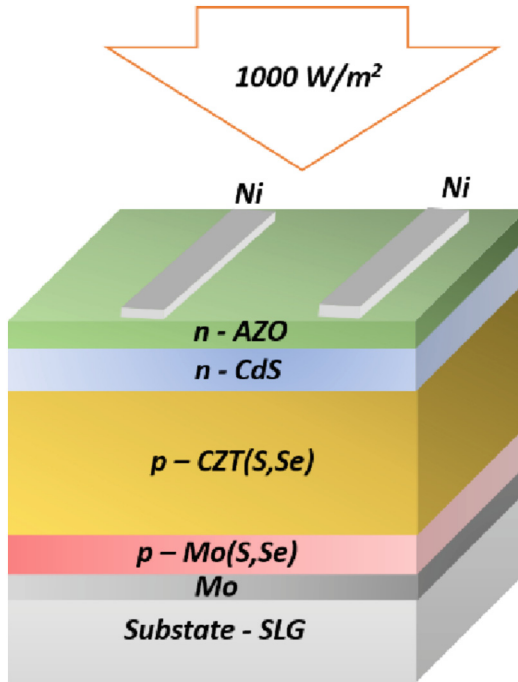
Fig. 1. The schematic configuration of the layer scheme of the investigated solar cell using the MoS(Se)$_2$ as an interface layer.

3   Results and Discussion

The primary objective of this study is to investigate the effect of the p-MoS(Se)$_2$ as an interfacial layer between the CZTS(Se) absorber layer and the Mo back contact in a CZTS(Se) based solar cell. Figure 2 shows the simulated J–V characteristics (a) and (b) the quantum efficiency (QE) of the CZTS solar cell structure. Considering the results obtained, it seems that the presence of p-MoS$_2$ directly affects the slope of the J–V curve, as shown in Fig. 2 (a) and (b). As a result of this study, it is possible to observe the ohmic properties of the contact more clearly. There is a significant difference between the slope of the slope ($\Delta I/\Delta V$) with the MoS(Se)$_2$ and that without the MoS(Se)2. By modifying the Schottky-type contact to a more favorable ohmic-type contact, the p-MoS(Se)$_2$ layer at the interface between CZTS(Se) and Mo improves the CZTS(Se)/Mo heterojunction interface. Studies have shown that Schottky contacts form at the buffer-Mo contact, which leads to resistive losses, unlike ohmic back contacts in CZTS(Se). Comparing the solar cell with and without the MoS$_2$ layer, the solar cell with the MoS2 layer performed 16.82% better than the solar cell without the MoS$_2$. These values were obtained using a high doping level of 10^{18} cm^{-3} at the interface layer. Furthermore, the Mo-CZTS standard structure with the MoS$_2$ layer increased J$_{sc}$ up to 27 mA/cm^2. Figure 2 shows that the insertion of the interfacial layer MoS(Se)$_2$ significantly improved the optical response of the device. Several factors could lead to this improvement, including greater absorption of solar radiation above 500 nm for CZTS/MoS$_2$. Figure 2 (b) shows an

increase in QE enhancement from 77.4% to 89.8% at longer wavelengths from 500 nm to 835 nm. The improvement is caused by the fact that the Molybdenum (Mo) and CZTS junction barrier heights decrease in the MoS_2 structure because the bandgap value is lower. Previous studies have examined how TMDC semiconductors influence solar cell device performance as interfacial layer materials in solar cell devices. Recombination speeds near 10^7 cm/s have been observed experimentally when the $MoS(Se)_2$ interfacial layer is used [22, 23].
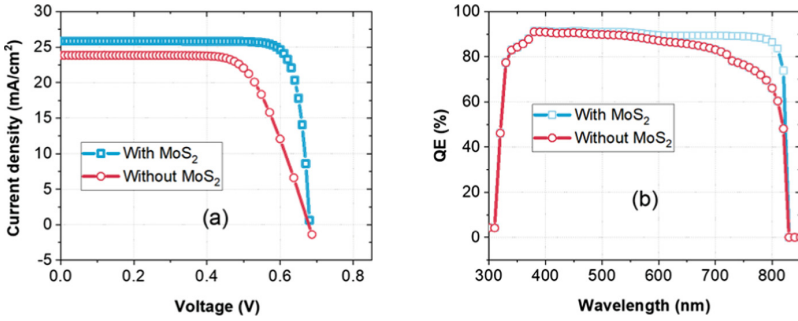
Fig. 2. (a) Current-voltage characteristic of CZTS solar cells with and without an interfacial layer MoS_2 (solid line and dashed line). (b) The spectral response and quantum efficiency (QE) with and without the MoS_2 layer (solid line and dashed line).

Due to the high hole recombination velocity at the $MoS(Se)_2$/Mo interface, solar cells have improved photovoltaic performance. V_{oc} values can be evaluated as follows:

$$V_{oc} = \frac{nkT}{q} \ln\left(\frac{J_{ph}}{J_o} + 1\right) \tag{1}$$

J_{ph} and J_o are photogenerated, and the reverse saturation current densities, respectively. n is the ideality factor. Boltzmann's constant and absolute temperature are represented by k and T, respectively. Due to the high hole recombination rate at the $Mo(S)Se_2$/Mo interface, an electron-driven Jo decreases. In CZTS(Se) solar cells, $MoS(Se)_2$/Mo interfaces can enhance their photovoltaic properties. Compared with CZTS(Se) solar cells without the interface layer, $MoS(Se)_2$ solar cells exhibit improved properties. Ordered defect compounds (ODCs) are formed when holes recombine between the absorber and buffer layers. In ODC layers, electrical conductivity is characterized by n-type characteristics [24]. By shifting the valence band maximum to Fermi, and by reducing interface recombination, the buffer/absorber interface absorber bandgap tends to increase, improving the solar cell's performance. The overall performance of the solar cell is enhanced by adding a suitable interfacial layer to the CZTS(Se) film. In order to investigate how operating temperature affects solar cell performance. In Fig. 3, we illustrate the J-V characteristics of solar cells consisting of CZTS, CZTSe, and CZTSSe. Open-circuit voltage decreases as temperature rises, due to an increase in reverse saturation current density J_o. A major factor contributing to the increase in Jo is the increased intrinsic carrier concentration n_i and the decrease in the bandgap of the

semiconductor material [25]. In addition to affecting the conductivity of the material, a higher cell temperature also degrades the performance of solar cells. Temperature and reverse bias saturation current density are related as follows:

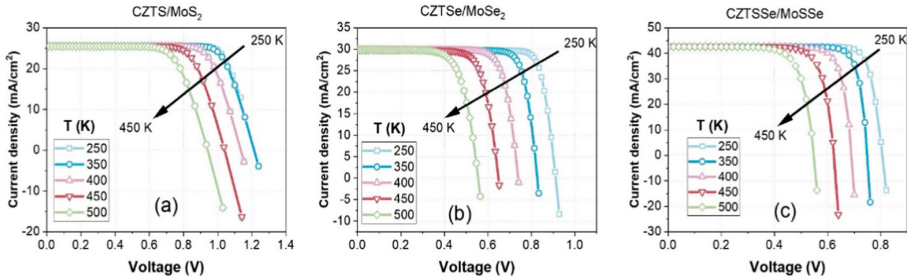$$J_o = AT^3 e^{-(E_{go}/K_B T)} \tag{2}$$

Fig. 3. Temperature dependence of the J-V characteristics for (a) CZTS, (b) CZTSe, and (c) CZTSSe [25].

where A is a constant for a given material and Ego is the bandgap at 0 °K. For semiconductors, the bandgap decreases as the temperature increases [24, 25]. Thus, the solar cell is able to recognize the longer wavelength regions of the solar spectrum. A final analysis examines how different operating temperatures affect the performance parameters such as V_{oc}, J_{sc}, FF, and efficiency at temperatures ranging from 250 °K to 450 °K for all structures. The obtained results are illustrated in Fig. 4.

It has been observed that J_{sc} currents in simulated cell structures have a nearly constant behavior at temperatures up to 450 K with values of 47 mA/cm^2, 30 mA/cm^2, and 25 mA/cm^2 for the CZTS, CZTSSe, and CZTSe absorbers, respectively. At 250 K, the CZTSSe/MoSSe structure had the highest PCE or optimum PCE (Fig. 4). The PCE is observed to decrease as the temperature increases. As a result, the PCE decreased by approximately 10% for the CZTSe and CZTSSe, increasing up to 450 K. By contrast, CZTS displayed more stable solar temperature-dependent cell performance at 350 K. Furthermore, all structures showed a decrease in FF and Voc with increasing temperature between 250°K and 450°K. As an example, the FF for both CZTSe and CZTSSe structures has dropped from 87% to 75 %, while the Voc has decreased by about 0.3V (from 1.1 V to 0.9 V for the CZTSSe). The decrease in FF and PCE with increasing temperature and degradation of efficiency is primarily due to the decrease in Voc. As the temperature rises, Voc and conversion efficiency decrease linearly with an increase in temperature, which can be interpreted as an increase in dark current. As the temperature increases, the bandgap narrows, accelerating the recombination process between electron-hole pairs in the conduction band and the valence band. CZTSSe-based solar cells' performance as a function of temperature is shown in Table 1. CZTSe-based solar cells perform most efficiently at high operating temperatures. Based on Table 1 calculations, The coefficient of the voltage variation to temperature ΔVoc/ΔT for CZTS, CZTSSe, and CZTSe PV devices, respectively, was −2.15 mV/K, −1.4 mV/K, and −1.35 mV/K, due to voltage variation to temperature.
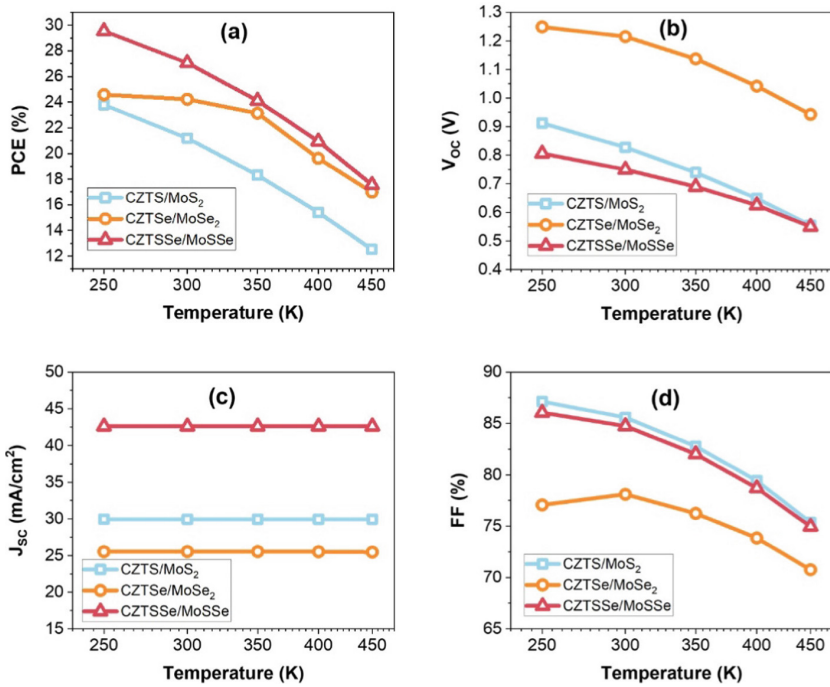
Fig. 4. The simulated photovoltaic performance parameters of CZTS, CZTSe, and CZTSSe based solar cells using MoS_2, $MoSe_2$, and MoSSe as an interfacial layer, respectively, as a function of operating temperature [25].

Table 1. The obtained performance behavior as a function of the temperature.

Parameters	CZTS	CZTSSe	CZTSe
$\Delta V_{oc}/\Delta T$ (mV/K)	−2.15	−1.4	−1.35
$\Delta PCE/\Delta T$ (%/°C)	−0.06	−0.05	−0.03
$\Delta FF/\Delta T$ (%/°C)	−0.055	−0.045	−0.03

4   Conclusion

CZT(S,Se) Solar cells were investigated for their performance as a function of temperature using SCAPS codes. All structures have been constructed with the $Mo(S,Se)_2$ TMDC materials integrated as an interfacial layer between the absorber layer and Mo back contact. CZTS(Se)/Mo heterojunctions show J-V characteristics that indicate that an ohmic contact is mediated by the interfacial layer. The results of this study have been analyzed using a variety of performance parameters, including V_{oc}, the FF, the J_{sc}, and PCE. According to the results, the CZTSe based solar cell demonstrated the most improved stable behavior when it was operated at high temperatures compared to the other solar cells. It has been concluded that the obtained results will increase the use

of CZTSe material in the manufacture of photovoltaic modules for high-temperature applications.

References

1. Harry, A.A., Albert, P.: Plasmonics for improved photovoltaic devices. Nat. Mater. **9**, 205–213 (2010)
2. Ramasamy, K., Malik, M.A., Brien, P.O.: Routes to copper zinc tin sulfide Cu_2ZnSnS_4 a potential material for solar cells. Chem. Commun. **48**, 5703–5714 (2012)
3. Boudaira, R., Meglali, O., Bouraiou, A., Attaf, N., Sedrati, C., Aida, M.S.: Optimization of sulphurization temperature for the production of single-phase CZTS kesterite layers synthesized by electrodeposition. Surf. Eng. **36**(9), 1000–1011 (2020)
4. Cozza, D., Ruiz, M., Duche, D., Simon, J.J., Escoubas, L.: Modeling the back contact of $Cu_2ZnSnSe_4$ solar cells. IEEE J. Photovolt. **6**, 1292–1297 (2016)
5. Tripathi, S., Maurya, S., Kumar, B., Dwivedi, D.K.: Comparative analysis of CZTS/CZTSe/CZTSSe absorber layer for solar cell applications. In: 2020 International Conference on Electrical and Electronics Engineering (ICE3) (2020)
6. Chen, S., et al.: Fabrication of low cost kesterite Cu2 ZnSnS4 (CZTS) thin films as counter-electrode for dye sensitised solar cells (DSSCs). Mater. Technol. **30**(5), 306–312 (2015). https://doi.org/10.1179/1753555715Y.0000000007
7. Shin, B., Bojarczuk, N.A., Guha, S.: On the kinetics of $MoSe_2$ interfacial layer formation in chalcogen-based thin film solar cells with a molybdenum back contact. Appl. Phys. Lett. **102**, 091907 (2013)
8. Zhang, J., Jung, Y.-G. (eds.): Advanced Ceramic and Metallic Coating and Thin Film Materials for Energy and Environmental Applications. Springer, Cham (2018). https://doi.org/10.1007/978-3-319-59906-9
9. Wang, W., et al.: The effects of SnS_2 secondary phases on Cu_2ZnSnS_4 solar cells: a promising mechanical exfoliation method for its removal. J. Mater. Chem. A. **6**, 2995–3004 (2018)
10. Todorov, T.K., Reuter, K.B., Mitzi, D.B.: High-efficiency solar cell with earth-abundant liquid-processed absorber. Adv. Mater. **22**, E156–E159 (2010)
11. Barkhouse, D.A.R., Gunawan, O., Gokmen, T., Todorov, T.K. Mitzi, D.B.: Device characteristics of a 10.1% hydrazine-processed $Cu_2ZnSn(Se,S)_4$ solar cell. Prog. Photovolt. Res. **20**, 6–11 (2012)
12. Todorov, T.K., et al.: Beyond 11% efficiency: characteristics of state-of-the-art Cu2 ZnSn(S,Se)4 solar cells. Adv. Energy Mater. **3**(1), 34–38 (2013). https://doi.org/10.1002/aenm.201200348
13. Wang, W., et al.: Device characteristics of CZTSSe thin-film solar cells with 12.6% efficiency. Adv. Energy Mater. **4**, 1301465 (2014)
14. Suryawanshi, M.P., et al.: CZTS based thin film solar cells: a status review. Mater. Technol. **28**(1–2), 98–109 (2013). https://doi.org/10.1179/1753555712Y.0000000038
15. Abou-Ras, D., et al.: Formation and characterisation of MoSe2 for Cu(In,Ga)Se2 based solar cells. Thin Solid Films **480**(11), 433–438 (2005). https://doi.org/10.1016/j.tsf.2004.11.098
16. Böker, T., et al.: Band structure of MoS_2, $MoSe_2$, and $\alpha-MoTe_2$: angle-resolved photoelectron spectroscopy and ab initio calculations. Phys. Rev. B. **64**, 235305 (2001)

17. Moustafa, M., Paulheim, A., Mohamed, M., Janowitz, C., Manzke, R.: Angle-resolved photoemission studies of the valence bands of ZrS_xSe_{2-x}. Appl. Surf. Sci. **366**, 397–403 (2016)
18. Singh, P., Singh, S.N., Lal, M., Husain, M.: Temperature dependence of I-V characteristics and performance parameters of silicon solar cell. Sol. Energy Mater. Sol. Cells **92**(12), 1611–1616 (2008)
19. Burgelman, M., Decock, K., Khelifi, S., Abass, A.: Advanced electrical simulation of thin film solar cells. Thin Solid Films **535**, 296–301 (2013)
20. Yasin, S., Abu Waar, Z., Al Zoubi, T.: Development of high efficiency CZTS solar cell through buffer layer parameters optimization using SCAPS-1D, Mater. Today Proc. **33**, 1825–1829 (2020)
21. Moustafa, M.O., Alzoubi, T.: Numerical simulation of single junction InGaN solar cell by SCAPS. Key Eng. Mater. **821**, 407–413 (2019)
22. Moustafa, M., Alzoubi, T.: Numerical study of CdTe solar cells with p-$MoTe_2$ TMDC as an interfacial layer using SCAPS. Mod. Phys. Lett. B. **32**, 1850269 (2018)
23. Yasin, S., AlZoubi, T., Moustafa, M.: Design and simulation of high efficiency lead-free heterostructure perovskite solar cell using SCAPS-1D. Optik **229**, 166258 (2021)
24. Alzoubi, T., Moustafa, M.: Simulation analysis of functional $MoSe_2$ layer for ultra-thin Cu(In, Ga)Se_2 solar cells architecture. Mod. Phys. Lett. B. **34**, 2050065 (2020)
25. Zoubi, T.A., AlGharram, M., Moustafa, M.: Insights into the impact of defect states and temperature on the performance of Kesterite-based thin-film solar cells. Optik **264**, 169442 (2022). https://doi.org/10.1016/j.ijleo.2022.169442

Research on Output Characteristics of Cooling, Heating and Electricity of Adiabatic Compressed Air Energy Storage System

Shuting Kong[1], Yanqiang Di[1,2(✉)], Yanyi Li[1,2], Xiaona Li[1,2], and Yu Weng[1,2]

[1] China Academy of Building Research, Beijing 100013, China
yanqiangdi@126.com
[2] China Building Technique Group Co., Ltd., Beijing 100013, China

Abstract. Advanced adiabatic compressed air energy storage (AA-CAES) technology has the advantages of zero emissions, which can meet the demand of combined storage and supply of various forms energy in integrated energy system. However, considering the coordination and unity of various energy outputs, there are still gaps in the research on the characteristics of cooling, heating and electricity energy output of AA-CAES. In view of the above problems, this paper used Gatecycle to establish an AA-CAES system model. By changing key operating parameters such as compression heat return ratio, turbine inlet air flow rate and turbine inlet air pressure, the output characteristics and round trip efficiency RTE of the system are analyzed. The results show that by adjusting the compression heat return ratio, the RTE varies from 52% to 75%, the output ratio of cooling, heating and electricity varies from 32% to 44%, 0 to 24% and 32% to 60%, respectively. By adjusting the air flow rate of turbine inlet, the RTE keep at about 70%, the output ratio of cooling, heating and electricity varies between 31%–42%, 23%–24% and 36%–45%, respectively. By adjusting the inlet air pressure of the turbine, the RTE varies from 67% to 83%, and the output ratio of cooling, heating and electricity varies from 37% to 42%, 20% to 24% and 38% to 39%, respectively. This study can provide theoretical basis for the design of AA-CAES multi-energy supply system structure, provide guidance for adjusting the output power of AA-CAES system and improve the coordination of multi-energy output.

Keywords: AA-CAES · Operating parameters · CHP · Output characteristics · Integrated energy efficiency

1 Introduction

Large-scale development and utilization of renewable energy is one of the main technical routes to solve the energy crisis and environmental pollution. However, the output power of renewable energy represented by wind and solar energy is intermittent and fluctuating due to the influence of seasonal alternation, day and night alternation, weather change and other factors. At the same time, the energy demand on the user side also shows a certain rule of change over time, resulting in different fluctuation states between the

user demand side and the energy supply side, leading to the mismatch between the energy demand and supply in time, space and form [1]. Energy storage technology can realize the space-time transfer of energy and is one of the effective ways to solve this problem. Currently, the commonly used energy storage technologies mainly include pumped storage, battery storage, flywheel storage, etc., but all of them have problems such as geographical constraints, cost, capacity and environmental protection, etc., and the energy interface form is single, which is difficult to meet the needs of users for the combined cooling, heating and electricity multi-energy supply [2].

Advanced adiabatic compressed air energy storage (AA-CAES) can use pressure vessel to store gas, get rid of the limitation of geographical conditions, and do not emit carbon dioxide during the working process. It can meet the demand of cold, heat and electricity multi-energy fed power supply in the comprehensive energy system, and is considered as one of the most promising energy storage technologies. At present, domestic and foreign scholars have carried out a series of studies on AA-CAES and its multi-energy combined supply system. Wen et al. [3] established an AA-CAES system model through Aspen Plus, and studied the influence of inlet air temperature and flow rate of turbine on the output electrical power and efficiency of the system. Facci et al. [4] established the thermodynamic model of the triple power supply system based on compressed air energy storage, determined the relevant parameters affecting the system efficiency, and proposed the correct selection principle of compressor, expander and heat exchanger. Jiang et al. [5] conducted thermal economic analysis and comparison of AA-CAES based cogeneration systems, revealing the influence of AA-CAES compression stages and expansion stages on the comprehensive efficiency, exergic efficiency and annual total cost saving rate of the systems. Szablowski et al. [6] established the dynamic model of adiabatic compressed air energy storage system with Aspen Plus, analyzed the changing rule of electrical efficiency and exergic efficiency with compression and expansion levels, and improved the energy conversion efficiency of the system to 50% by optimizing the parameters. Jabari et al. [7] designed and optimized the scheduling of the cogeneration system of cooling, heat and electricity based on AA-CAES and air source heat pump, and the results showed that the use of AA-CAES system could reduce the operating costs of the whole system in cooling and heating modes by 21.79% and 22.36%, respectively. Li et al. [8] proposed a cogeneration system of cold, heat and electricity based on adiabatic compressed air energy storage, which can meet users' demands for power supply, heating and cooling by adjusting air pressure and temperature at the inlet of turbine, and analyzed the round trip efficiency of the system under different working conditions. Yao et al. [9] proposed a distributed energy system of combined cold, heat and electricity supply coupled with compressed air energy storage technology and internal combustion engine technology, established the thermodynamic model of the system, and conducted sensitivity analysis of the system, including the performance and key parameters of compressor, heat exchanger, turbine, internal combustion engine and other key equipment. Zhang et al. [10] coupled compressed air energy storage device, gas internal combustion engine and wind turbine to form a combined cooling, heat and electricity supply system, and carried out capacity configuration for the system in order to improve the matching of system output and load.

To sum up, the research on AA-CAES and its multi-energy combined supply system mainly focuses on system performance analysis, capacity configuration and operation strategy optimization, and there are still two major problems:

(1) The research on AA-CAES system mainly aims at improving the charging and discharging efficiency of the system, while heat and cold energy are only by-products of the power generation process, without considering the possibility of coordination and unification of electricity, heat and cold energy.

(2) AA-CAES multi-energy combined power supply system is mainly studied based on specific structure of AA-CAES multi-energy combined power supply system. In the conceptual design stage of engineering application, it is necessary to design the structure of AA-CAES multi-energy combined power supply system with high efficiency according to different forms of energy output characteristics of AA-CAES, and then conduct further detailed optimization research. At present, there is a lack of research on the output characteristics of AA-CAES cold, heat and electricity.

In view of this, this paper use Gatecycle to establish an adiabatic compressed air energy storage system model. By changing key operating parameters such as compression heat return ratio, turbine inlet air flow rate and turbine inlet air pressure, the cool, heat and electricity output characteristics and the round trip efficiency of the system are analyzed. The results of this study can provide theoretical basis for the design of AA-CAES multi-energy supply system structure, and provide guidance for adjusting the output power of AA-CAES system and improving the coordination of multi-energy output.

2   Methodology

2.1   System Description

Figure 1 is the theoretical diagram of the advanced adiabatic compressed air energy storage system studied in this paper. The system includes compression subsystem, heat recovery subsystem and turbine subsystem. The heat recovery subsystem includes heat storage tank, heat exchanger, regenerative device and heat storage medium, the heat storage medium adopts pressurized water. The compression subsystem adopts the structure of five-stage compression (C1–C5) and inter-stage heat exchanger (HE1–HE5). The five-stage compressor is driven by surplus wind power and photoelectric power. The heat exchanger is located at the back end of each compressor to recover the compression heat generated during the compression process. The structure can not only reduce the inlet air temperature and consumption of each compressor, but also save the cost of heat exchanger. The turbine subsystem adopts a first-stage expansion structure, and uses the regenerator to preheat the inlet air of the turbine, so as to improve the output power and efficiency of the turbine. The system uses surplus wind power or photoelectric to drive the compression subsystem, and the compressed high-pressure air expands in the turbine subsystem to do work to output electric energy. The low-temperature air after work can be cooled externally, and the compressed waste heat generated in the compression process can be heated externally, thus realizing the output of cold, heat and electricity of the system.
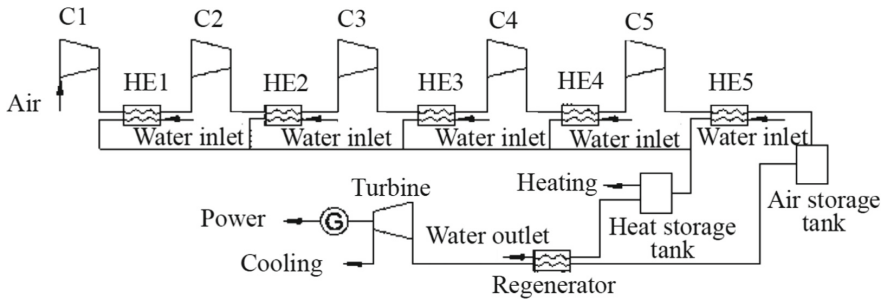
Fig. 1. Theoretical diagram of the advanced adiabatic compressed air energy storage system.

2.2 Gatecycle Mode of the AA-CAES System

Gatecycle model is established according to Fig. 1. Firstly, a compression model was established. Five compressors were dragged from Gatecycle's equipment toolbox to the modeling area, and a heat exchanger was placed behind each compressor as an inter-cooler. Then the heat storage tank model, air inlet model, air discharge model, cooling water inlet model, heat flow outlet model was established. After the critical equipment model is established, connect each device in turn according to the process shown in Fig. 1. Finally, input the initial design parameters of the system in each device model. Gatecycle model of compression link is shown in Fig. 2. Then establish the expansion link model, the modeling process is the same as the compression link, respectively establish turbine model, regenerator model, each fluid inlet and outlet model, according to the system schematic diagram of the equipment connected to the initial design parameters of the system. Gatecycle model of expansion link is shown in Fig. 3.
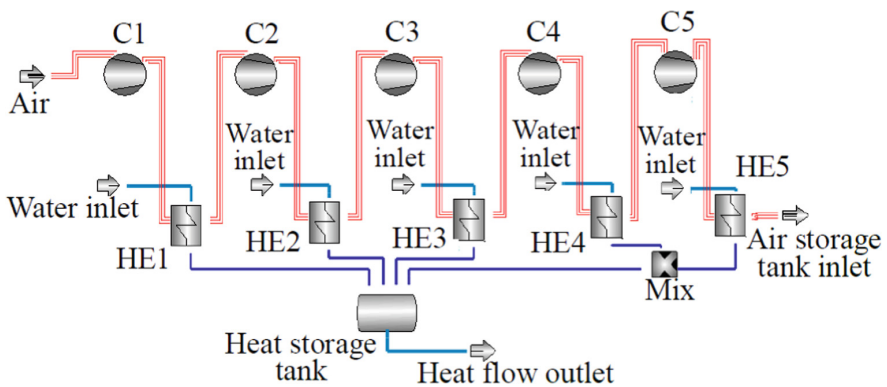
Fig. 2. Gatecycle model of compression link.

The user's cooling, heating and electricity load and economic benefit are the key factors to determine the capacity of each device in the system. As the research in this paper focuses on the system's cooling, heating and electricity dynamic output characteristics and system efficiency, the capacity optimization configuration of each component of the
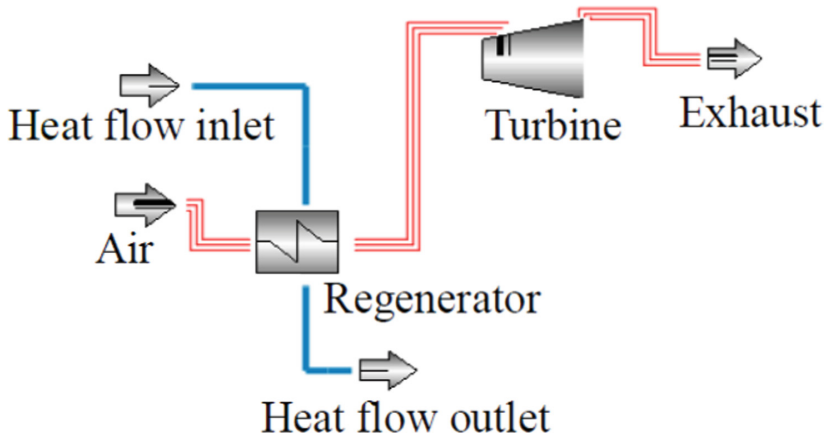
Fig. 3. Gatecycle model of expansion link.

system is not considered for the time being. The initial parameters of the entire system are shown in Table 1.

Table 1. Initial system parameters.

Parameters	Values	Unit
Compressor stages	5	/
Compression ratio	3.545/2.668/2.670/2.630/1.859	/
Isentropic efficiency of compressor	77.62/79.62/82.31/81.15/78.44	%
Compressor flow rate	0.43	kg/s
Inlet air temperature	25/45/45/45/45	°C
Initial air pressure	99	kPa
Storage air temperature	37	°C
Storage air pressure	10	MPa
Expansion stages	1	/
Isentropic efficiency of turbine	80	%
Turbine inlet air flow rate	2.28	kg/s
Heat exchanger efficiency	80	%
Turbine outlet air pressure	105	kPa
Turbine inlet air pressure	2500	kPa
Compression heat return ratio	10	%

2.3   Research on Cold, Heat and Electricity Output Characteristics of the System

Gatecycle is used in this paper to simulate the changes of key operating parameters of the system, such as cooling, heating and electricity output capacity, the RTE with compression heat return ratio, turbine inlet air flow rate, turbine inlet air pressure and so on. Control variable method was adopted in the research process, that is, except the studied variables, other parameters remained unchanged, the initial values of each variable are shown in Table 1.

2.4   Evaluation Criteria

Based on the analysis of the first law of thermodynamics, according to the conservation of energy quantity, the law of energy transfer and conversion in the system is revealed, so as to reflect the total energy utilization of compressed air energy storage system. The round trip efficiency RTE of the system is defined as the ratio of total electric energy, heat and cooling output of the system to the input energy within a complete energy storage and release cycle, as shown in the following Eq. (1):

$$\eta_Z = \left(E_{out} + Q_{h,out} + Q_{c,out}\right)/E_{in} \tag{1}$$

where E_{out} is the total electric energy output by the system, kW; $Q_{h,out}$ is the total heat output of the system, kW; $Q_{c,out}$ is the total cooling capacity of system output, kW; E_{in} is the electrical energy input from external system, kW.

The calculation formula of $Q_{h,out}$ is shown in the following Eq. (2):

$$Q_{h,out} = C_w m_w \left(t_{w,out} - t_{w,in}\right)(1 - a) \tag{2}$$

where C_w is the specific heat capacity of water, kJ/(kg·°C); m_w is the mass flow of cooling water, kg/s; $t_{w,out}$ is the temperature of cooling water at outlet side of inter-cooler, °C; $t_{w,in}$ is the cooling water temperature of inlet side of inter-cooler, take 20 °C; a is the compression heat return ratio, %.

The calculation formula of $Q_{c,out}$ is shown in the following Eq. (3):

$$Q_{c,out} = C_{air} m_{air} \left(t_{air,out} - t_{air,in}\right) \tag{3}$$

where C_{air} is the specific heat capacity of air, kJ/(kg·°C); m_{air} is the air mass flow rate at turbine outlet, kg/s; $t_{air,out}$ is the turbine exhaust temperature, °C; $t_{air,in}$ is the system inlet air temperature, °C.

3   Results and Discussion

3.1   Effect of the Compression Heat Return Ratio

The compression heat return ratio is the proportion of the heat used to preheat the inlet air of the turbine to the recovered compression heat. Adjusting the compression heat return ratio can change the ratio of cold, heat and electricity output of the compressed air energy storage system. The larger the compression heat return ratio is, the more heat

used to preheat turbine inlet air in the recovered compression heat, and the less heat supplied to customers by the system. The compression heat return ratio can be adjusted to match system output and customer load according to needs. Figure 4 and Fig. 5 show the variation of cooling, heating and electricity output capacity and the RTE of the system with compression heat return ratio.

According to Fig. 4, when the compression heat return ratio is less than 20%, the power generation increases and the cooling capacity decreases as the compression heat return ratio increases. When the compression heat return ratio increases from 0 to 20%, the power generation increases by 99.17 kW, and the cooling capacity decreases by 164.54 kW. This is mainly because increasing the compression heat return ratio can increase the air temperature at the turbine inlet. The higher the temperature is, the greater the internal energy of the air is, then the higher the turbine working capacity and the output electric energy is. But at the same time, the turbine exhaust temperature rises, leading to the decrease of the system output cooling capacity. When the compression heat return ratio is greater than 20%, restricted by the efficiency of the regenerator, increasing the compression heat return ratio cannot improve the inlet air temperature of the turbine. Therefore, the power generation and cooling capacity remain unchanged, the power generation is kept at 441.51 kW, and the cooling capacity is kept at 298.82 kW. In the process of the compression heat return ratio gradually increasing from 0 to 100%, the output heat of the system presents a downward trend, from the initial 260.97 kW to 0, and the whole process presents a linear change.

According to Fig. 5, with the increase of the compression heat return ratio, the RTE of the system gradually decreased from the initial 75% to 52%, a decrease of 23%. According to the above analysis, with the increase of the compression heat return ratio, the power generation of the system increases first and then stays constant, the cooling capacity decreases first and then stays constant, the heating capacity always presents a downward trend, and the total output energy of the system generally presents a downward trend. However, the change of the compression heat return ratio does not affect the power consumption in the compression process, so the RTE shows a downward trend.

In the whole process of the change of the compression heat return ratio, the system output power ratio changes between 32% and 60%, the output cooling ratio changes between 32% and 44%, and the output heat ratio varies from 0 to 24%.

3.2 Effect of the Turbine Inlet Air Flow Rate

The inlet air flow rate of turbine is one of the important factors affecting the cooling, heating and electricity output characteristics of the system. Under the condition that the parameters of the compression and storage link remain unchanged, changing the air flow rate of turbine inlet can change the energy release time of the system, adjust the relative value of the energy release and storage time, thus changing the ability of the system to output cold, heat and electricity in the dimension of time. Figure 6 and Fig. 7 reflect the variation of the cooling, heating and electricity output capacity and the RTE of the system with the air flow rate at the turbine inlet.

According to Fig. 6, the power generation, cooling capacity and heating capacity of the system all show a rising trend with the increase of air flow at turbine inlet. This is mainly because with the increase of air flow at the turbine inlet, the amount of air
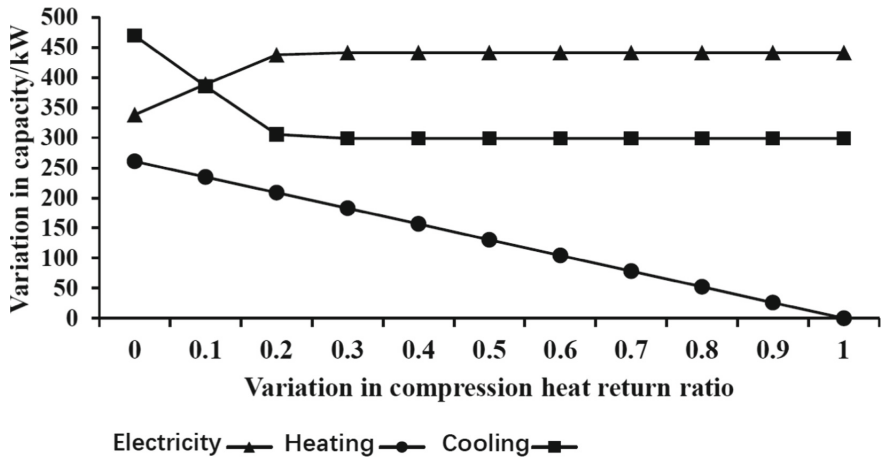
Fig. 4. The variation of cooling, heating and electricity output capacity with compression heat return ratio.
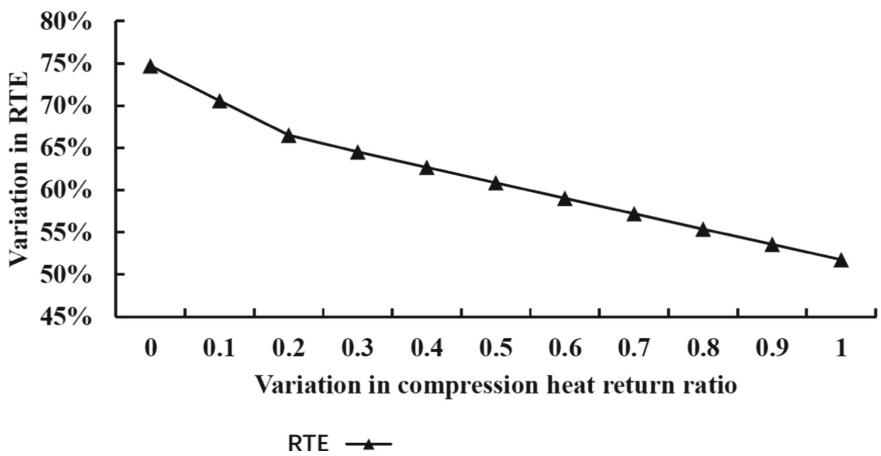

Fig. 5. The variation of RTE with compression heat return ratio.

entering the turbine for work increases, while the total internal energy of air basically remains unchanged, so the power generation of the system increases. At the same time, the turbine exhaust temperature decreases, so the system cooling capacity increases. Since changing the air flow rate of turbine inlet will change the relative time of energy storage release of the system, increasing the air flow rate of turbine inlet will reduce the energy release time of the system. After converting the system heating amount into energy storage and energy release time, the system heating amount shows a rising trend. When the air flow rate of turbine inlet is less than 2.43 kg/s, the power generation of the system is greater than the cooling capacity. When the air flow rate of turbine inlet is greater than 2.43 kg/s, the power generation of the system is less than the cooling capacity. Adjusting the air flow rate of turbine inlet can well change the relative value of

the power output and cooling capacity of the system. When the inlet air flow increases from 0.43 kg/s to 4.43 kg/s, the output power increases from 83.27 kW to 708.12 kW, the output cooling capacity increases from 56.36 kW to 829 kW, and the output heat increases from 44.32 kW to 456.55 kW.

According to Fig. 7, with the increase of air flow at the turbine inlet, the RTE of the system basically remains unchanged at about 70%. Therefore, it can be seen that the air flow rate at the turbine inlet has little influence on the RTE. Changing the air flow rate at the turbine inlet will only cause the change in the output of energy storage release time dimension, and affect the low-power long-time release mode and high-power short-time release mode, but will not have much influence on the total output capacity of the system.

In the whole process of the change of air flow at the turbine inlet, the proportion of output electric quantity varies between 36% and 45%, the proportion of output cooling quantity varies between 31% and 42%, and the proportion of output heat varies between 23% and 24%.
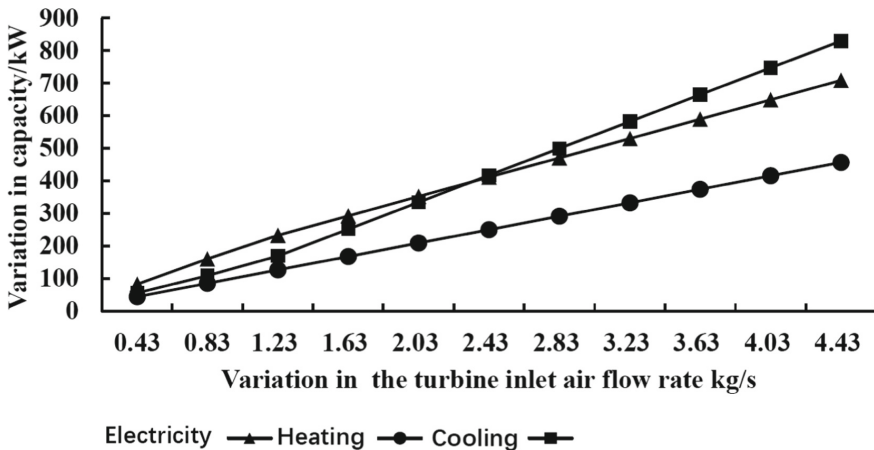
Fig. 6. The variation of cooling, heating and electricity output capacity with the air flow rate at the turbine inlet.

3.3   Effect of the Turbine Inlet Air Pressure

The inlet air pressure of turbine is also one of the important factors affecting the cooling, heating and electricity output characteristics of the system. The gas storage pressure in the system is a fixed value of 10 MPa, and a throttle valve is set between the gas storage tank and the turbine. The inlet pressure of the turbine air can be controlled between 0–10 MPa by adjusting the opening of the throttle valve. Figure 8 and Fig. 9 reflect the variation of the cooling, heating and electricity output capacity and the RTE of the system with the turbine inlet air pressure.

According to Fig. 8, with the increase of inlet air pressure, the power generation and cooling capacity of the system gradually increase, but the increase rate gradually slows
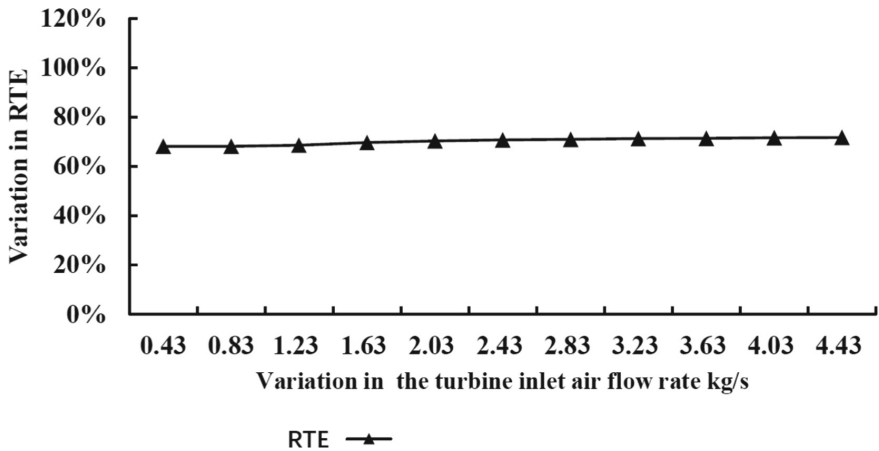
Fig. 7. The variation of RTE with the air flow rate at the turbine inlet.

down. If the air pressure at the turbine inlet increases from 2.5 MPa to 3 MPa, the power generation increases by 18.06 kW, and the cooling capacity increases by 20.24 kW. When the inlet air pressure of turbine increases from 7 MPa to 7.5 MPa, the power generation and cooling capacity of the system increase only 3.83 kW and 5.77 kW. The reason is that the turbine design mode is "fixed outlet pressure" in the simulation process. Therefore, when the turbine inlet pressure increases, the work of high-pressure air in the turbine increases and the exhaust temperature decreases. The increase of turbine inlet air pressure does not affect the compression process, and the system heat supply remains unchanged at 234.87 kW. When the air pressure at the turbine inlet is less than 2.73 MPa, the power generation is greater than the cooling capacity; when the air pressure at the turbine inlet is greater than 2.73 MPa, the power generation is less than the cooling capacity. When the air pressure at the turbine inlet increases from 2 MPa to 7.5 MPa, the power generation increases from 371.57 kW to 459.95 kW, the cooling capacity increases from 359.75 kW to 493.33 kW, and the heating capacity keeps at 234.87 kW.

According to Fig. 9, when the air pressure at the turbine inlet increases, the RTE of the system increases, because the power generation and cooling capacity of the system increase while the heating capacity remains unchanged. With the decrease of the increase rate of power generation and cooling capacity, the increase rate of RTE decreases. If the inlet air pressure of turbine increases from 2.5 MPa to 3 MPa, the RTE increases from 71% to 73%. When the inlet air pressure of the turbine increases from 7 MPa to 7.5 MPa, the RTE increases from 82% to 83%.

In the whole process of the change of air pressure at the turbine inlet, the proportion of output electricity varies between 38% and 39%, the proportion of output cooling varies between 37% and 42%, and the proportion of output heat varies between 20% and 24%.
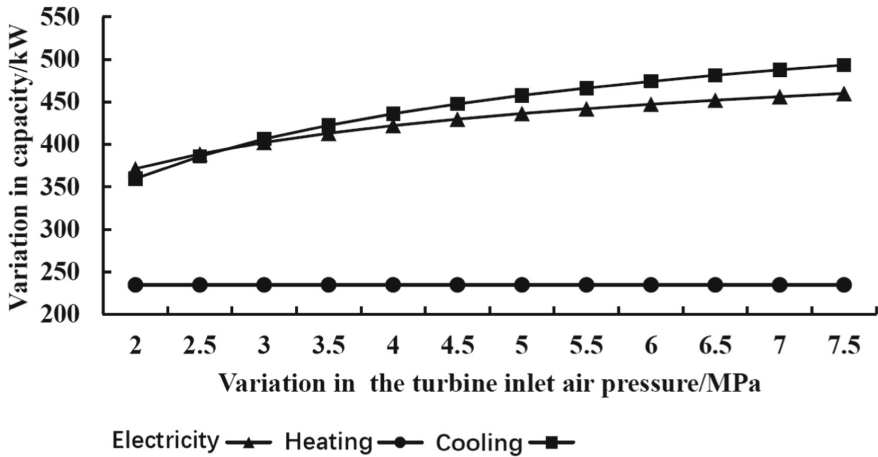
Fig. 8. The variation of cooling, heating and electricity output capacity with the turbine inlet air pressure.
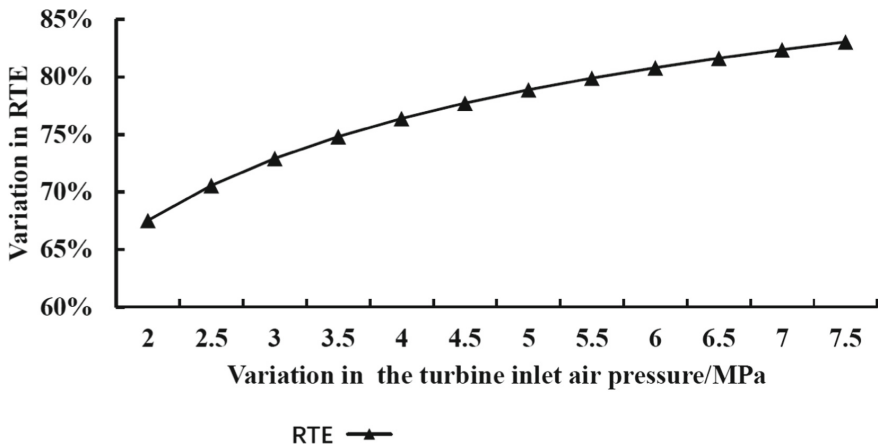

Fig. 9. The variation of RTE with the turbine inlet air pressure.

4 Conclusion

In this paper, Gatecycle was used to simulate and analyze the influence of key operating parameters such as compression heat return ratio, turbine inlet air flow rate and turbine inlet air pressure on system performance, including the cooling, heating and electricity output characteristics and the RTE of the system. This study fills in the blank of theoretical research on multi-energy flow output characteristics in the field of AA-CAES, makes up for the problem that existing studies have long focused on the electrical efficiency of AA-CAES and ignored the coordination of the output of cooling, heating and electricity multi-energy flow. This paper provides a theoretical basis for the optimal design of compressed air energy storage multi-energy combined power supply system, a method

guidance for adjusting various energy output power of the system and improving source-charge matching, which is expected to promote the large-scale application of AA-CAES in comprehensive energy system. The main conclusions are as follows:

(1) When the compression heat return ratio is less than 20%, the power generation increases and the cooling capacity decreases with the increase of the compression heat return ratio. When the compression heat return ratio increases from 0 to 20%, the power generation increases by 99.17 kW, and the cooling capacity decreases by 164.54 kW. When the compression heat return ratio is greater than 20%, restricted by the efficiency of the regenerator, increasing the compression heat return ratio cannot improve the inlet air temperature of the turbine. The power generation and cooling capacity remain unchanged, the energy generation is 441.51 kW, and the cooling capacity is 298.82 kW. In the whole process of the change of the compression heat return ratio, the system heating capacity and RTE show a linear downward trend, the system output power ratio changes between 32% and 60%, the output cooling capacity ratio changes between 32% and 44%, and the output heat ratio changes between 0 and 24%.

(2) With the increase of air flow at turbine inlet, the power generation, cooling capacity and heating capacity of the system all show a rising trend. The RTE remains at about 70% during the whole process. Changing the air flow at the turbine inlet will only cause the change of the energy storage and release in the time dimension, affecting the low-power long-time energy release mode and the high-power short-time energy release mode, without much influence on the total output capacity of the system. In the whole process of the change of air flow at the turbine inlet, the proportion of output electric quantity varies between 36% and 45%, the proportion of output cooling quantity varies between 31% and 42%, and the proportion of output heat varies between 23% and 24%.

(3) With the increase of air pressure at turbine inlet, the power generation, cooling capacity and RTE of the system gradually increase, and the increase rate gradually slows down, while the heating capacity of the system remains unchanged during the whole process. When the inlet air pressure of the turbine is less than 2.73 MPa, the system energy generation is greater than the cooling capacity; when the inlet air pressure of the turbine is greater than 2.73 MPa, the system energy generation is less than the cooling capacity. With the increase of air pressure at turbine inlet, the increase rate of the RTE decreases. In the whole process of the change of air pressure at the turbine inlet, the proportion of output electricity varies between 38% and 39%, the proportion of output cooling varies between 37% and 42%, and the proportion of output heat varies between 20% and 24%.

References

1. He, Y.L., Yan, J.J., Yang, W.W., Li, Y.S., Tao, Y.B.: High efficient energy storage in distributed energy system. Bull. Nat. Nat. Sci. Found. China **34**(03), 272–280 (2020). https://doi.org/10.16262/j.cnki.1000-8217.2020.03.004

2. Xue, X.D., Mei, S.W., Lin, Q.Y., Chen, L.J., Chen, Y.: Energy Internet oriented non-supplementary fired compressed air energy storage and prospective of application. Power Syst. Technol. **40**(01), 164–171 (2016). https://doi.org/10.13335/j.1000-3673.pst.2016.01.022

3. Wen, X.U., et al.: Simulation and efficiency analysis of advanced compressed air energy storage system. J. Chin. Soc. Power Eng. **41**(09), 802–808 (2021). https://doi.org/10.19805/j.cnki.jcspe.2021.09.013

4. Facci, A.L., Sánchez, D., Jannelli, E., Ubertini, S.: Trigenerative micro compressed air energy storage: concept and thermodynamic assessment. Appl. Energy **158**, 243–254 (2015). https://doi.org/10.1016/j.apenergy.2015.08.026

5. Jiang, R., Cai, Z., Peng, K., Yang, M.: Thermo-economic analysis and multi-objective optimization of polygeneration system based on advanced adiabatic compressed air energy storage system. Energy Convers. Manage. **229**, 113724 (2021). https://doi.org/10.1016/j.enconman.2020.113724

6. Szablowski, L., Krawczyk, P., Badyda, K., Karellas, S., Kakaras, E., Bujalski, W.: Energy and exergy analysis of adiabatic compressed air energy storage system. Energy **138**, 12–18 (2017). https://doi.org/10.1016/j.energy.2017.07.055

7. Jabari, F., Nojavan, S., Ivatloo, B.M.: Designing and optimizing a novel advanced adiabatic compressed air energy storage and air source heat pump based µ-Combined Cooling, heating and power system. Energy **116**, 64–77 (2016). https://doi.org/10.1016/j.energy.2016.09.106

8. Li, Y., Wang, X., Li, D., Ding, Y.: A trigeneration system based on compressed air and thermal energy storage. Appl. Energy **99**, 316–323 (2012). https://doi.org/10.1016/j.apenergy.2012.04.048

9. Yao, E.R., Wang, H.R., Xi, G.: A novel combined cooling heating and power system with coupled compressed air energy storage and combustion engine. J. Xi'an Jiaotong Univ. **50**(01), 22–27 (2016). https://doi.org/10.7652/xjtuxb201601004

10. Zhang, H.Y., Chen, S., Zhu, T., Gan, Z.X.: Performance analysis of distributed energy system with adiabatic compressed air energy storage. Proc. CSEE **38**(S1), 142–150 (2018). https://doi.org/10.13334/j.0258-8013.pcsee.180314

Modelling the Permeate Flux in Ultrafiltration of Xanthan Gum

Michelle C. Almendrala[1]([✉]), David Joshua G. Barangan[1], Jomari C. Gutierrez[1], Zhane Ann M. Tizon[1], Ralph Carlo T. Evidente[2], and Bonifacio T. Doma[1]

[1] School of Chemical, Biological, and Materials Engineering and Sciences, Mapua University Intramuros, 658 Muralla Street, Intramuros, 1002 Manila, Metro Manila, Philippines
`mcalmendrala@mapua.edu.ph`

[2] Division of Advanced Nuclear Engineering, POSTECH, Pohang, Gyeongbuk 37673, South Korea

Abstract. Using MATLAB, this study develops an empirical and semi-empirical model for determining the initial flux in the ultrafiltration of xanthan solution as an alternative separating process in concentrating xanthan gum. The literature of reference uses hollow fiber membrane of A/G Technology Corporation, which the authors in this current study utilized to gather data for developing the permeate flux equation. In this research, the empirical model incorporates viscosity by replacing the concentration term from the original model based in the referenced literature. The pH parameter was tested if it had any significant effect to the permeate flux. Consequently, multiple empirical and semi-empirical models were developed in such a way that the authors selected the one with the lowest absolute relative error and high R-squared for optimization purposes. The modified model was found to have higher accuracy with an absolute relative error of 5.91% as compared to 11.42% with the old model, whereas the semi-empirical model had an average percent error of 7.69% . The optimal parameters found were 73 kPa for transmembrane pressure (TMP), 30.2 $cm^{-1}s^{-1}$ for γ_w/L, 50 °C for temperature, and 159.3 cP for viscosity.

Keywords: Xanthan gum · Multiple linear regression · MATLAB · Optimization

1 Introduction

The rheological property of xanthan gum which known to be pseudoplastic is commonly used as food thickener and even found in petroleum production [1]. Production of this polysaccharide commonly uses alcohol precipitation in separating xanthan gum from the solution [2]. The process requires around two to three volumes of isopropanol to precipitate one volume of xanthan gum broth and requires distillation to recover the alcohol used which is energy-intensive [3]. Furthermore, isopropanol is a volatile organic compound and highly flammable that poses a safety work and environmental hazard. This requires the need for investing in expensive flame-proof equipment [4]. Which leads to the interest in investing in membrane technology as it is efficient, clean, and safe to work with [5].

Resources in literature regarding modelling ultrafiltration of xanthan gum are limited. An empirical model is known in determining the permeate flux in the ultrafiltration of xanthan gum solution that accounts transmembrane pressure, shear rate, and xanthan concentration as well as optimization but only for finding the optimal transmembrane pressure [3]. However, the parameters of viscosity, pH, and wall shear rate per unit length have not yet been investigated. Where viscosity is expected to have a more significant effect on predicting the initial flux in the ultrafiltration of xanthan gum solution [4].

This study developed a linear equation for determining viscosity. Develop empirical models that incorporates viscosity, pH, and wall shear rate per unit length. Develop a semi-empirical model based on the gel-polarization model. And optimize the operating parameters used in the experiment is based on the response surface methodology (RMS).

The significance of this study is to develop different models for permeate flux of ultrafiltration of xanthan gum solution. Finding the best parameters that optimize the permeate flux. Modelling can be used to predict the initial permeate flux of xanthan gum solution based on a specified concentration and other operating parameters. The optimization of operating conditions will be possible to design the process of concentrating xanthan gum.

The scope and limitation of this study are that fouling does not take any effect on the permeate flux. Only the initial stage of the ultrafiltration was studied as the effect of fouling and accumulation overtime of the membrane was not accounted in the data. Whereas the two effects cause the permeate flux to decrease as functions of time due to the clogging of pores of the membrane [5]. Therefore, experimental data used in this study were based on the steady state assumption and no fouling effect. Furthermore, the optimization was only performed within a local maximum and local minimum as a measure of the initial operating conditions in ultrafiltration operation.

2 Methodology

2.1 Experimental Data

The setup experiment is shown in Fig. 1, the xanthan solution was recirculated allowing the observation of the initial flux at steady state. The temperature, pressures (feed & retentate), pH, and viscosity were measured from the pH probe, thermometer, pressure gauges, and viscometer. A total of 146 flux data were obtained that ranges from 73.39–172.39 kPa for transmembrane pressure, 30–50 °C for temperature, 4–7 pH, 2–5% w/v for concentration, and 6.63–30.20 for γ_w/L. The ultrafiltration of xanthan solution had the assumption of steady-state condition and negligible fouling effect. The data for developing a viscosity equation varies in shear rate (10–200 rpm) and xanthan concentrations (2.5–8%w/v).
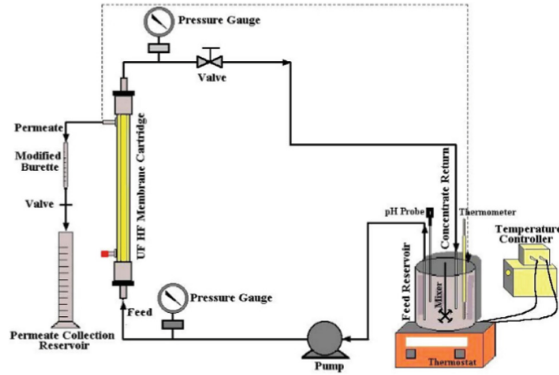
Fig. 1. Ultrafiltration of xanthan broth setup

Note, the shear rate (γ) parameter in was measured from a Brookfield viscometer. And for γ_w/L was calculated using the equation below under laminar flow conditions.

$$\gamma_w = \left[\frac{3n + 1}{4n}\right] \frac{4Q_B}{m\pi r^3} \tag{1}$$

where,

γ_W - shear rate on the membrane wall
n - flow behavior index
Q_B - volumetric feed flow rate
r - radius of a hollow fiber tube
m - number of hollow fiber tube.

2.2 Multiple Linear Regression of Viscosity

The processed viscosity data was first visualized by graphing the linear and exponential plots of viscosity and shear rate using MATLAB's plot functions. Fitting a linear equation with two or more independent variables and a dependent variable requires the use of multiple linear regression. The multiple linear regression of viscosity was done using the regress function of MATLAB with the xanthan concentration and the shear rate (γ) as parameters for viscosity (μ). The linear equation of viscosity takes on the form of Eq. 2 where the regress function gives the coefficients (a, b, & c) as one of its outputs and R-square being the other output. Equation 3 is the exponential form for the viscosity equation.

$$\ln\mu = a + bC - c\ln\gamma \tag{2}$$

$$\mu = e^{a + bC - c\ln\gamma} \tag{3}$$

where,

μ - viscosity (cP)
C - xanthan gum concentration (% w/v)
γ - shear rate (rpm).

2.3   Empirical Model

Multiple linear regression was performed through MATLAB in developing the empirical model. The independent variables incorporated into the empirical model were transmembrane pressure, wall shear rate per unit length, temperature, viscosity, and pH. About 70% of the experimental data was used for developing new models and 30% was used for validation. Rather than adding viscosity (μ) into the new model, it instead substitutes xanthan concentration. This is to avoid the multicollinearity between xanthan concentration and viscosity as they are correlated with each other [6]. The effect of pH was also investigated if having the parameter would affect the filtration flux. Therefore, the empirical models take on the form as below:

$$J = e^A (\text{TMP})^B \left(\frac{\gamma_w}{L}\right)^C (T)^D (\mu)^E (\text{pH})^F \tag{4}$$

$$J = e^A (\text{TMP})^B \left(\frac{\gamma_w}{L}\right)^C (T)^D (\mu)^E \tag{5}$$

2.4   Semi-empirical Model

The development of the semi-empirical model is based on the gel-polarization model, where it describes the phenomenon of concentration polarization. Where due to the accumulation of solute molecules at the solution-membrane interphase resulting from the balance between the convective mass transport and back diffusion. Due to concentration polarization, there is the formation of a gel layer of macrosolutes on the membrane surface that offers an additional hydraulic resistance to flow, as seen if Fig. 2 [5].
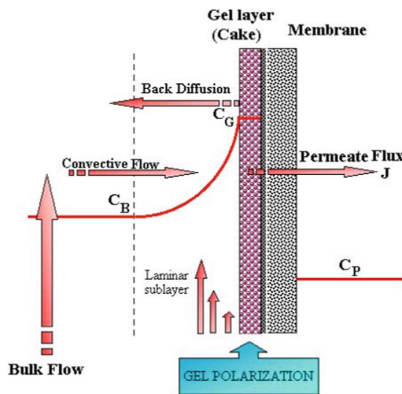
Fig. 2. Diagram of gel polarization

This model is presented as,

$$J = k \ln\left(\frac{C_g}{C_b}\right) \tag{6}$$

$$k = e^A \left[\gamma_W \frac{D^2}{L}\right]^{0.33} \tag{7}$$

In the model development, diffusion has been shown to be unimportant in determining the concentration of large molecules. The osmotic pressure was assumed to be zero with a steady state process because it increased solute concentration causes a rise in the osmotic pressure which partially cancels the applied pressure difference. The computed Reynold's number for the polysaccharide solution is below 1 which means the flow inside each hollow fiber tubule is creeping flow.

$$J = e^A \left(\frac{\gamma_W}{L}\right)^B \ln\left(\frac{C_g}{C_b}\right) \tag{8}$$

Equation 7 was then modified with the idea that an increase of the solution viscosity with the solute concentration can play the main role in the existence of a limiting permeate flux at a finite pressure difference [7].

$$J = e^A (\mu)^B \ln\left(\frac{C_g}{C_b}\right) \tag{9}$$

The process for obtaining the coefficients is similar to how the empirical model's coefficients were obtained. The accuracy of the models was determined by obtaining the R-squared value and average percent errors. Where, the plot of permeate flux versus the logarithm of the bulk concentration C_b gives a straight line with a negative slope equal to the mass transfer coefficient k. According to Eq. 7, the intercept with the abscissa should occur when $C_b = C_g$. This provides a way for experimentally determining the gel concentration. Thus, the value of Cg is determined when the value of permeate flux is extrapolated to its extinction value on the x-axis. The value of the gel concentration was approximated based on the assumption that the gel layer concentration is affected by the shear rate and other parameters.

2.5 Optimization

The optimization is based on response surface methodology or RSM (Eq. 10) which generally is to obtain the desired maximum or minimum response variable (z) at specific independent variables (x & y), and ε is the experimental error which will not be included.

$$z = f(x, y) + \varepsilon \tag{10}$$

The parameters investigated are the TMP, temperature, γ_w/L, and viscosity. MATLAB contains the essential functions for optimizing the models to determine the best operating parameters for maximizing the filtration flux. For the "max" and "min" functions the optimum and least favorable conditions will be obtained. The "surf" function is used for the 3D visualization of the plot with the "plot3" function used for plotting the maximum and minimum points.

3   Results and Discussion

3.1   Viscosity Equation

Equation 11 was the result of the coefficient determined by regression of MATLAB and this equation was converted into the form of Eq. 12 for computing viscosity. A high degree of linearity was obtained with an R^2 equivalent to 0.999 from the equation. The exponential plot (Fig. 3) shows the pseudoplastic behavior of the xanthan gum solution at different concentrations.

$$\ln\mu = 10.4837 + 0.1992C - 0.7855\ln\gamma \tag{11}$$

$$\mu = e^{10.4837 + 0.1992C - 0.7855\ln\gamma} \tag{12}$$
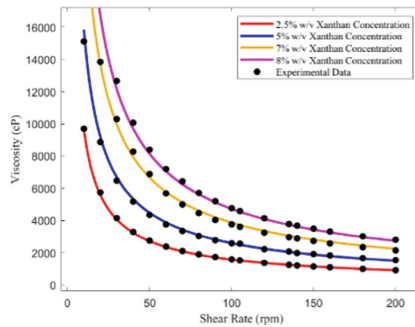
Fig. 3. Flow curves of xanthan solution

The effect of concentration causes the flow curve to shift higher. And as expected for a pseudoplastic behavior, increasing the shear rate results in the lowering of viscosity. The highest viscosity is 28,800 cP which is 8% w/v xanthan concentration and a shear rate of 10 rpm. While the lowest viscosity is 920 cP which is 2.5% w/v xanthan concentration and a shear rate of 200 rpm.

3.2   Empirical Model

The 146 data was divided into 70% data (102 data) was used for developing the empirical model with the 30% data (44 data) used for validation. Below are the developed empirical models, where Eq. 13 retains pH and Eq. 14 pH is removed.

$$J = e^{-0.0809}(\text{TMP})^{-0.4656}\left(\frac{\gamma}{L}\right)^{-0.291}(T)^{-0.3155}(\mu)^{-1.1130}(\text{pH})^{0.0812} \tag{13}$$

$$J = e^{0.1018}(\text{TMP})^{-0.45}\left(\frac{\gamma_w}{L}\right)^{-0.2975}(T)^{0.3003}(\mu)^{-1.1175} \tag{14}$$

Table 1 list the performance of the empirical models inaccurately determining the flux in the ultrafiltration of xanthan solution.

Table 1. Performance of empirical models

Empirical equations	70% data		30% data	
	APE	R^2	APE	R^2
Eq. 13	6.20%	0.9253	6.53%	0.9045
Eq. 14	6.37%	0.9198	5.91%	0.9034

The model flux and experimental flux were plotted as seen in Fig. 4 and Fig. 5. However, between Eq. 13 and Eq. 14, it was found that removing the pH has better APE and R^2. Equation 14 has a APE of 5.91% and an R^2 of 0.9034. Therefore, having pH as a parameter for the empirical model has no significant effect in determining the ultrafiltration flux. It should be noted that xanthan gum is an anionic polysaccharide and xanthan solution is sensitive to changes to pH [2]. However, xanthan solution is only sensitive below pH 4 and is highly stable above it [2].
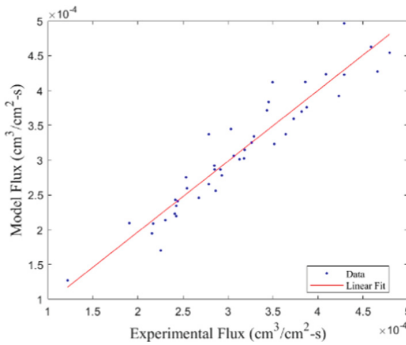
Fig. 4. Graphs of experimental flux vs model flux of Eq. 13
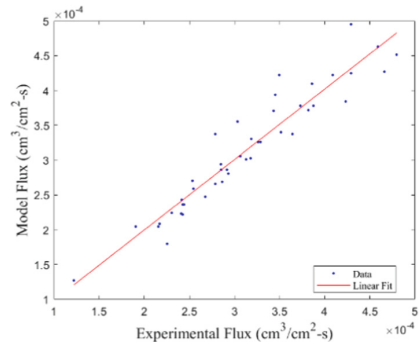
Fig. 5. Graphs of experimental flux vs model flux of Eq. 14

3.3 Semi-empirical Models

Below are the developed semi-empirical models, where Eqs. 15 and 16 varies C_g while Eq. 17 and Eq. 18 C_g is constant. The models were validated and plotted as seen in Figs. 6, 7, 8 and 9.

$$J = e^{-9.6005} \left(\frac{\gamma_w}{L} \right)^{0.5416} \ln \left(\frac{C_g}{C_b} \right) \tag{15}$$

$$J = e^{-5.3616} (\mu)^{0.6054} \ln \left(\frac{C_g}{C_b} \right) \tag{16}$$

$$J = e^{-10.136} \left(\frac{\gamma_w}{L} \right)^{0.4965} \ln \left(\frac{C_g}{C_b} \right) \tag{17}$$

$$J = e^{-5.6519}(\mu)^{0.5539}\ln\left(\frac{C_g}{C_b}\right) \qquad (18)$$

Validation for Eq. 15 resulted in an APE of 7.69% and R^2 of 0.8314 as shown in Fig. 6. While validation for Eq. 16 is depicted in Fig. 7, which resulted in an APE of 9.30% and R^2 of 0.794. The lowest value of C_g calculated is 18.21%w/v where TMP is 168.92 kPa, γ_w/L is 29.19 cm^{-1} s^{-1}, and T is 30 °C. While the highest value of C_g calculated is 21.61% w/v where TMP is 127.55 kPa, γ_w/L is 7.12 cm^{-1} s^{-1}, and T is 45 °C. Table 2 list the performance of the semi-empirical models inaccurately determining the flux in the ultrafiltration of xanthan solution.

Table 2. Performance of semi-empirical models

Empirical equations	70% data		30% data	
	APE	R^2	APE	R^2
Eq. 15	10.04%	0.8131	7.69%	0.8314
Eq. 16	10.78%	0.8031	9.30%	0.7940
Eq. 17	10.27%	0.8005	7.83%	0.8215
Eq. 18	11.08%	0.7901	9.52%	0.7831
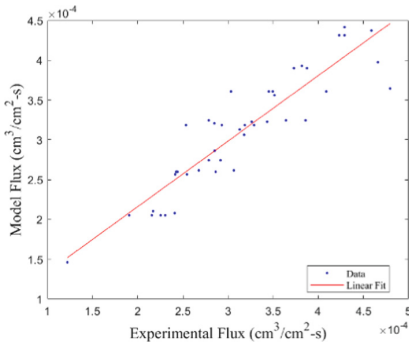
Fig. 6. Experimental flux vs model flux of Eq. 15
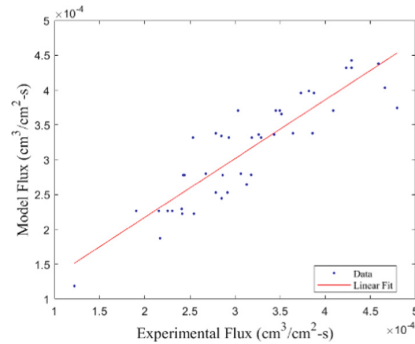
Fig. 7. Experimental flux vs model flux of Eq. 16

For constant C_g, the value is calculated by averaging the values of C_g is 19.54% w/v. The resulting model flux and experimental flux were plotted as seen in Fig. 8 and Fig. 9. The statistical value of R^2 of the two models is 0.8215 for Eq. 17 and 0.7831 for Eq. 18. As for the average percentage error, Eq. 17 has 7.83% and Eq. 18 has 9.52%.

For the semi-empirical model, Eq. 15 was found to perform better than the latter equations. Replacing γ_w/L with viscosity significantly increased the APE and decreased the R^2. Using a constant C_g or the mean C_g had no effect in improving the APE and the R^2.
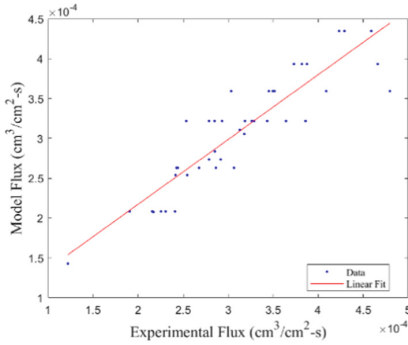
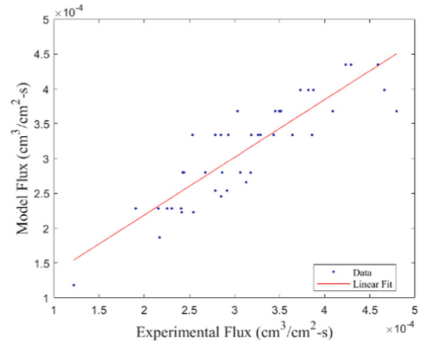**Fig. 8.** Experimental flux vs model flux of Eq. 17

Fig. 9. Experimental flux vs model flux of Eq. 18

3.4 Optimization

For optimization, Eq. 14 and Eq. 15 were chosen for being the best empirical and semi-empirical models. To maximize the filtration flux, it is desirable to minimize TMP and xanthan concentration and maximize γ_w/L and temperature. The response variables assigned for Eq. 14 are the transmembrane pressure, γ_w/L, temperature, and viscosity. While for Eq. 15, its response variable is wall shear rate per length and the natural log of C_g over C_b.
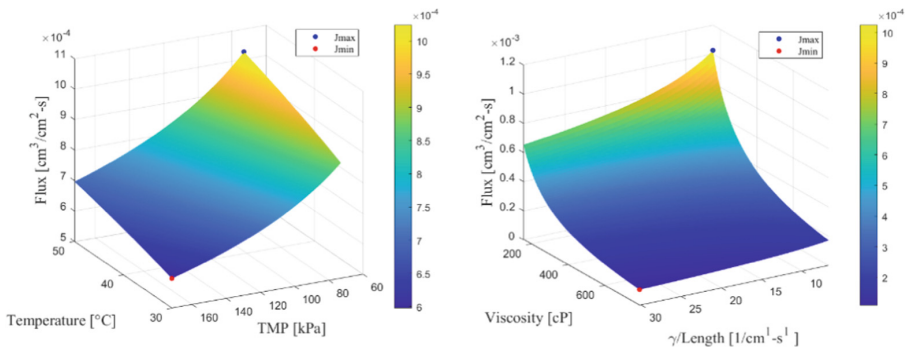
Fig. 10. (Left) Eq. 14, graph of temperature and transmembrane pressure vs flux and (Right) graph of viscosity and γ_w/L vs flux.

Figure 10 shows that increasing the transmembrane pressure decreases the filtration flux which is due to the thickening and rapid formation of the gel layer. Filtration of macromolecules such as whey protein is known to have specific resistance be strongly dependent on transmembrane pressure [8]. For context, γ_w/L was obtained from one of Leveque's solutions [9], where it was used to determine the mass transfer coefficient. However, the effects of wall shear rate per unit length in Eq. 14 and Eq. 15 are contrasting. It is expected that increasing γ_w/L should also increase the filtration flux like in Eq. 15,

but Eq. 14 shows the opposite effect. Figure 10 also shows that increasing the temperature causes an increase in filtration flux, while viscosity causes the opposite effect. Increasing the temperature of the xanthan solution has the effect of decreasing the viscosity allowing for less resistance to filtration [4, 10]. In Fig. 11 it is seen that the increase of natural log of C_g over C_b causes an increase in filtration flux which is due to the low C_b. The surface plots in Fig. 11 show the points of maximum and minimum fluxes (J_{max} and J_{min}). The empirical model Eq. 13 had a maximum flux obtained is 1.025×10^{-3} cm^3/cm^2-s where its responses are 73 kPa for TMP, 6.63 cm^{-1} s^{-1} for γ_w/L, 50 °C for T, and 159.3 cP for μ. As for the minimum flux it is 5.975×10^{-4} cm^3/cm^2-s where its responses are 172 kPa for TMP, 30.2 cm^{-1} s^{-1} for γ_w/L, 30 °C for T, and 794.2 cP for μ.
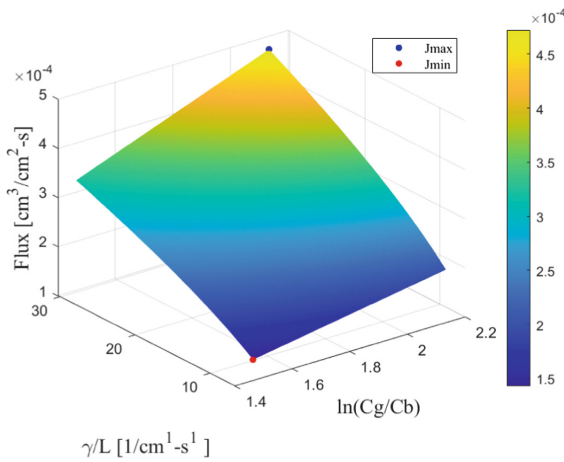
Fig. 11. Eq. of Wall shear rate per length and ln(Cg/Cb)

For the optimization of the semi-empirical model. The Eq. 15 was chosen had a maximum flux obtained in Eq. 15 is 4.723×10^{-4} cm^3/cm^2-s, 30.2 cm^{-1} s^{-1} for γ_w/L, 21.087% w/v for C_g, 2.5% w/v for C_b. And for the minimum flux of Eq. 15 it is 1.428 $\times$ 10^{-4} cm^3/cm^2-s, 6.63 cm^{-1} s^{-1} for γ_w/L, 21.594% w/v for C_g, 5% w/v for C_b. Because the optimized maximum flux was higher and the model was more accurate, we can conclude that the empirical model performs better than the semi-empirical model.

4 Conclusion

This study developed an empirical and a semi-empirical model for determining the filtration flux in the ultrafiltration of xanthan solution. A mathematical model for viscosity was developed based on the effect of shear rate and concentration of xanthan gum exhibited a high degree of linearity with an R^2 of 0.999 to the experimental data and was proven useful in the development of permeate flux models. It was found that pH had no significant effect on the filtration flux but is suspected to change when pH drops below 4 as Eq. 14 had an APE of 5.91% and an R^2 of 0.9034 while Eq. 13 had an APE

of 6.53% and an R^2 of 0.9045. The semi-empirical models did not perform well compared to the empirical models. The empirical model was found to have less APE with the experimental flux and was slightly more linear than using the semi-empirical model. However, the empirical model contrasted with the effects of the wall shear rate per unit length as it shows to have a decreasing effect with the flux. Optimization found that decreasing the transmembrane pressure and viscosity while increasing the temperature and wall shear rate per unit length results in a high initial flux in the ultrafiltration of xanthan solution. Overall, the empirical model Eq. 14 proved to be the best out of all equations in accurately determining the flux.

References

1. Katzbauer, B.: Properties and applications of xanthan gum. Polym. Degrad. Stab. **59**, 81–84 (1998). https://doi.org/10.1016/s0141-3910(97)00180-8
2. Sworn, G.: Xanthan gum. In: Handbook of Hydrocolloids, pp. 833–853 (2021). https://doi.org/10.1016/B978-0-12-820104-6.00004-8
3. Lo, Y.M., Yang, S.T., Min, D.B.: Kinetic and feasibility studies of ultrafiltration of viscous xanthan gum fermentation broth. J. Membr. Sci. **117**, 237–249 (1996). https://doi.org/10.1016/0376-7388(96)00067-1
4. Xuewu, Z., Xin, L., Dexiang, G., et al.: Rheological models for xanthan gum. J. Food Eng. **27**, 203–209 (1996). https://doi.org/10.1016/0260-8774(94)00092-1
5. Cheryan, M.: Ultrafiltration and Microfiltration Handbook, 2nd edn. CRC Press, Boca Raton (1998)
6. Daoud, J.I.: Multicollinearity and regression analysis. J. Phys. Conf. Ser. **949**, 012009 (2018)
7. ladisavljevic, G.T., Radjkovic, M.B.: The effect of concentration dependent viscosity on permeate flux limitation in ultrafiltration. Food Technol. **2**, 9–19 (1999)
8. Steinhauer, T., Kühnl, W., Kulozik, U.: Impact of protein interactions and transmembrane pressure on physical properties of filter cakes formed during filtrations of skim milk. Procedia Food Sci. **1**, 886–892 (2011)
9. Ranjan, R., Dasgupta, S., De, S.: Mass transfer coefficient with suction for laminar non-Newtonian flow in application to membrane separations. J. Food Eng. **64**, 53–61 (2004). https://doi.org/10.1016/j.jfoodeng.2003.09.012
10. Reinoso, D., Martín-Alfonso, M.J., Luckham, P.F., Martínez-Boza, F.J.: Rheological characterisation of xanthan gum in brine solutions at high temperature. Carbohydr. Polym. **203**, 103–109 (2019). https://doi.org/10.1016/J.CARBPOL.2018.09.034

Author Index